Title
VOID BEHAVIOR DURING CREEP AND SINTERING AT HIGH TEMPERATURES

Author
Hsueh, C-H.

Publication Date
1981-09-01

UC-25

LBL-13397

Lawrence Berkeley Laboratory
UNIVERSITY OF CALIFORNIA

Materials & Molecular Research Division

VOID BEHAVIOR DURING CREEP AND SINTERING AT HIGH TEMPERATURES

Chun-Hway Hsueh
(Ph.D. thesis)

September 1981

Prepared for the U.S. Department of Energy under Contract W-7405-ENG-48

DISCLAIMER

VOID BEHAVIOR DURING CREEP AND SINTERING AT HIGH TEMPERATURES

Chun-Hway Hsueh

Ph.D. Thesis

Materials and Molecular Research Division
Lawrence Berkeley Laboratory
and
Department of Materials Science and Mineral Engineering
University of California
Berkeley, California 94720

September 1981

This work was supported by the Director, Office of Energy Research, Office of Basic Energy Sciences, Materials Science Division of the U.S. Department of Energy under Contract No. W-7405-ENG-48.

PART I

EFFECT OF INHOMOGENEITY ON CREEP RUPTURE

Table of Contents

ABSTRACT v

ACKNOWLEDGMENTS vii

1. INTRODUCTION 1

2. LOCAL STRESSES 4

3. CAVITY GROWTH 11

3.1 General Consideration 11

3.2 Derivation of Governing Equations 12

3.3 Equilibrium Cavities 14

3.4 Crack-like Cavities 16

3.5 Velocity Trends 19

4. PROPAGATION TIME 22

5. ZONE SPREADING 24

6. DISCUSSION AND CONCLUSIONS 28

APPENDIX 31

REFERENCES 34

FIGURE CAPTIONS 37

FIGURES 39

PART II

PORE/GRAIN BOUNDARY SEPARATION

Table of Contents

1. INTRODUCTION 53

2. PORE VELOCITIES 58

3. GRAIN BOUNDARY SHAPES 65

4. PORE BREAKAWAY 68

5. IMPLICATIONS AND CONCLUSIONS 72

APPENDIX I 74

APPENDIX II 79

APPENDIX III 87

REFERENCES 89

FIGURE CAPTIONS 91

FIGURES 93

VOID BEHAVIOR DURING CREEP AND SINTERING AT HIGH TEMPERATURES

Chun-Hway Hsueh

Materials and Molecular Research Division
Lawrence Berkeley Laboratory
and
Department of Materials Science and Mineral Engineering
University of California
Berkeley, California 94720

ABSTRACT

Pores in ceramics are often found both in the process of fabrication and in service. The porosity is a serious problem because of its effects both on electrical conductivity, thermal conductivity and most importantly upon strength. The present work is hence devoted to a study of void formation and propagation under an applied tensile stress and to pore elimination in the final stage of sintering.

The first part of the thesis is a study of creep rupture in ceramics. This occurs by the nucleation, growth and coalescence of cavities in localized, inhomogeneous arrays. The cavities grow by diffusive mechanisms; a process which has previously been analyzed for uniform cavity distributions. Experimental results indicate that the inhomogeneity exerts substantial perturbations upon the failure sequence and hence, on the failure time. The failure sequence in the presence of inhomogeneity effects is examined in this paper. A model is developed that accounts for the experimentally observed damage accumulation features and predicts the influence of inhomogeneity upon the failure time.

The second part of the thesis is devoted to the motion of pores attached to two grain interfaces. It is shown that pores exhibit a maximum steady state velocity that varies with the dihedral angle and

that the onset of non-steady state pore motion results in grain boundary convergence and the separation of the pore from the grain boundary. The peak steady state pore velocity has been compared with grain boundary velocities for several grain configurations, in order to identify a critical condition for the onset of separation. This comparison indicates that the pore size must be maintained below a critical value to ensure grain boundary attachment.

ACKNOWLEDGMENTS

I would like to express my deep appreciation to Professor Anthony G. Evans for his excellent guidance and support in this work. I would also like to thank Professors Iain Finnie and David P. Whittle for critical reading and comment on the thesis.

Interaction with colleagues and friends greatly assisted the completion of this work. Special thanks are extended to the helpful secretaries Mary Besser and Virginia Farr.

Finally, I thank my parents for their love, understanding and encouragement through these years.

This work was supported by the Director, Office of Energy Research, Office of Basic Energy Sciences, Materials Science Division of the U.S. Department of Energy under Contract No. W-7405-ENG-48.

PART I

EFFECT OF INHOMOGENEITY ON CREEP RUPTURE

1. INTRODUCTION

Creep behavior in polycrystalline ceramic materials has been investigated extensively in recent years because of the increasing use of these materials at high temperatures. It is usually found that cavities form at grain boundaries during creep and subsequently grow and coalesce to produce failure.[1-4] Experimental results indicate that cavities generally form on grain boundaries oriented in a direction perpendicular to the applied tensile load.[5-6]

A variety of cavity growth mechanisms has been proposed depending on the temperature, the stress and the grain size.[7] Most commonly, the growth of cavities has been explained by a diffusional transport mechanism. This process was first analyzed by Hull and Rimmer,[8] who considered a square array of spherical voids on a grain boundary slab subject to a tensile load. They found that the void growth rate increases linearly with increasing applied stress, provided that the voids grow with a spherical morphology (by the absorption of vacancies from the grain boundary) and that the grains on both side are rigid. The model has been modified by subsequent workers by imposing different boundary conditions.[9-11] However, the conclusions were essentially the same. The assumption concerning cavity shape implies that surface diffusion is rapid enough that cavity growth is controlled by grain boundary diffusion. However, these conditions do not always pertain. The cavities sometimes exhibit an elongated, crack-like shape. Hence, Chuang and Rice[12] and others[13-15] considered the other limiting case of a thin crack-like cavity with a cavity growth rate controlled by

surface diffusion. Different relations between applied stress and growth rate were established for this growth process.

Mechanisms such as grain boundary sliding[16,17], power law creep[18,19] and the combined effects of diffusion and power law creep[20-25] may also be in operation during the cavitation process. However, the present study is restricted to long failure times and high temperatures so that diffusive growth mechanisms prevail.

Prior studies of diffusive cavity growth assumed a homogeneous distribution of cavities. However, the cavitation process is inhomogeneous, involving preferential cavitation in certain regions of the polycrystalline array[2,26] (Fig. 1). The intent of this work is thus to examine the role of cavitation inhomogeneity upon the cavity evolution process and hence, upon the time to failure.

The principal sources of inhomogeneity are assumed to derive from local variations in the grain boundary or surface diffusivity (attributed to grain orientation effects[27], augmented by impurity distributions[2,28]) or in the dihedral angle (i.e., the ratio of the boundary to the surface energy). The inhomogeneity effect resulting from a grain size distribution has been discussed by other investigators.[29-31]

The inhomogeneity is needed to obtain preferred sites for initial cavitation, but appears to be of secondary importance for the zone spreading and coalescence aspects of failure, as will become clear later.

The concept of constraint on diffusive cavity growth was first introduced by Dyson[32], who considered inhomogeneous cavitation at

the grain boundaries of a polycrystalline aggregate. He suggested that compatibility between the cavitated grain boundaries and the creep deformation of the surrounding material attenuates the local stress transmitted to the cavitated region. A subsequent analysis of this phenomenon by Rice[33], considered diffusional void growth on an isolated grain boundary and evaluated the local stress by simulating the system as a circular crack in a viscous medium.

In the present study, differences in matter transport rates associated with local variations in grain boundary diffusion, and/or inhomogeneous cavitation, result in local stresses. These stresses are induced by the constraint of the surrounding material, and tend to suppress the original differences in matter transport.[32,33] The constraint thus provides some stability to the inhomogeneous cavity arrays and thereby contributes importantly to the rupture time.[33] An approach for estimating the level of constraint is described in the second section of the thesis. Then, the formation of cavities, subject to the appropriate constraints, is examined in the third section. Initially, the cavities exhibit an equilibrium morphology. Thereafter, a transition to crack-like morphology ensues; a prediction of the transition is drawn in Fig. 2.[34] This transition is of particular significance to creep rupture in polycrystalline ceramics, because it signals the onset of more rapid cavity growth[34], subject to reduced constraint. In the fourth section the time taken for the cavities to extend across grain facets is discussed. Ultimately, the cavitation zone begins to spread laterally and creates the failure initiating macrocrack. This process is considered in the fifth section.

2. LOCAL STRESSES

Inhomogeneous diffusion or localized cavitation creates local stresses that may substantially differ from the applied stress. Determination of these local stresses is central to the analysis of creep rupture. The stress distributions in a polycrystalline aggregate is complex, and a rigorous stress analysis requires extensive numerical computation. An approximate analytic solution is thus suggested, which permits both the identification of the important creep rupture parameters and elucidates the essential trends. First the creeping material is viewed as a viscous solid with the corresponding viscosity related to the diffusivity and the grain size.[16] Thus the analysis can be based upon a continuum solution for the transformation of an inclusion in an elastic medium[35] and then the analogy between linear elastic and viscous materials is invoked[36] (Appendix). The solution requires cavitation to occur within a zone of diameter d (Fig. 3a) such that matter deposition on the intervening boundaries procedes at a rate which differs from the average mass transport rate in the surrounding material. The enhanced matter deposition, $\Delta\delta$, that occurs in time, Δt, induces rigid body displacements of the juxtaposed grains which, if unconstrained, would produce a shape change in the zone comprising these grains (Fig. 3b). The unconstrained shape change is analagous to a transformation strain, e^T_{ij}, of a corresponding elastic problem, as depicted in Fig. 3b. Maintaining compatibility between the 'transformation' zone with the surroundings (the 'matrix'), the matrix grains induce a constraint P^I_{ij} on the transformation zone, and corresponding stresses in the matrix (Fig. 3c, d). Hence the constraint can be calculated by

adopting the Eshelby procedures.[35] This comprises the imposition of surface tractions to the transformation zone that causes it to conform with the matrix, followed by the application of equal, but opposite, body forces along the interface to remove the applied surface tractions.

The constraint P^I_{ij} is dictated by the unconstrained transformation strain, e^T_{ij}, and by the elastic constants for the elastic medium.[35] Transforming the solutions to the viscous material, the constraint P^I_{ij} is then dictated by the unconstrained transformation strain rate, $\dot{e}^T_{ij}$, and by the effective viscosity, η[16], of the transformation zone and matrix (Appendix). While the whole material is subject to diffusive creep, the cavitation region is subject to an extra flux from the cavity surface, which deposits within the transformation region. Hence, the unconstrained strain rate is the net cavity volume change rate. Cavitation procedes in response to stresses normal to the cavitating boundary; the appropriate $\dot{e}^T_{ij}$ thus derives from the cavity volume change in the presence of the resultant normal stress acting during the interval, Δt.

The viscous deformation involves grain boundary sliding and diffusive flow[16,37] (Fig. 3c). The viscosity assigned to this mode of deformation depends upon the number of grains participating in the relaxation process (especially those grains at the periphery of the cavitation zone, Fig. 3c, where the shear stresses are most intense). The viscosity approaches the continuum value for the polycrystalline aggregate, $\eta_{cont.}$,[16] when a sufficiently large number of grains are involved;

$$\eta_{cont.} \equiv \sigma_\infty/\dot{\varepsilon}_\infty = 3\sqrt{3}\ell^3 kT/14\Omega(\sqrt{3}\ell D_\ell + \pi D_b\delta_b) \quad (1)$$

where $D_b\delta_b$ is the grain boundary diffusion parameter, D_ℓ is the lattice diffusivity, Ω is the atomic volume, ℓ is the grain facet length, kT has the usual meaning, σ_∞ is the applied stress and $\dot{\varepsilon}_\infty$ is the steady-state creep rate. It is assumed, for present purposes, that cavitation zones consisting of at least three grain facets (Fig. 3) embrace an adequately large number of peripheral grains (i.e. $\sim$8 peripheral grains in the two dimensional section shown in Fig. 3, but $\sim$30 peripheral grains for the three-dimensional zone subject to analysis).

The transformation strain-rate $\dot{e}^T_{ij}$ is determined by the distribution of matter deposition within the cavitation zone; it is a function of both the total cavitation rate, the distribution of grain boundary orientations within the cavitation zone, and the zone shape. In general, $\dot{e}^T_{ij}$, will contain both deviatoric and dilational components. The general stress analysis is unwieldly. Hence, the cavitation zone is first approximated by an ellipsoid (Fig. 3c) and the constraint derived from the Eshelby solution.[35] Specific results are presented for the two limits of most significance. One extreme case obtains when the aspect ratio is unity and the ellipsoid becomes a sphere; the other is when the aspect ratio is large and the ellipsoid can be considered to exhibit a disc shape.

When the transformation zone is a sphere, the dilational component, e^T, results in a constraint, P^I, independent of the zone size.[38] As the cavitation zone diameter is relatively small (such as the three cavitating facets depicted in Fig. 3), the constraint is approximately the same as that expected for a purely dilational transformation

(Appendix). The zone can therefore be considered subject to a dilation dictated exclusively by the cavitation volume, ΔV. Consequently, by equating the cavitation zone volume to that of an ellipsoidal region of equivalent size (Fig. 3c);

$$V \approx \pi d^2 \ell/3 \tag{2}$$

the transformation strain rate becomes;

$$\dot{e}^T \approx 3\Delta\dot{V}/\pi d^2 \ell \tag{3}$$

This dilational strain, pertinent to the lower zone size limit, results in a size independent, upper bound constraint. For viscosities characterized by Eq. (1), the constraint is given by (Appendix, Eq. (A7));

$$p^I = -\left(\frac{18\sqrt{3}}{7\pi}\right) \frac{\ell^2 kT\ \Delta\dot{V}}{\Omega d^2(\sqrt{3}\ell D_\ell + \pi D_b \delta_b)} \tag{4}$$

Conservation of matter within the zone requires that;

$$\Delta\dot{V} \approx \pi d^2 \Delta\dot{\delta}/3 \tag{5}$$

The constraint thus becomes;

$$p^I \approx -\left(\frac{6\sqrt{3}}{7}\right) \frac{\ell^2 \Delta\dot{\delta} kT}{\Omega(\sqrt{3}\ell D_\ell + \pi D_b \delta_b)} \tag{6}$$

The local tensile stress σ_ℓ^i normal to the cavitating boundaries depicted in Fig. 3 is thus

$$\sigma_{\ell}^{i} = \left(\frac{3}{4}\right)\sigma_{\infty} - \left(\frac{2\sqrt{3}}{7}\right)\frac{\ell^2 \Delta\dot{\delta} kT}{\Omega(\sqrt{3}\ell D_{\ell} + \pi D_b \delta_b)} \tag{7}$$

where the first term is the applied stress resolved on the grain boundary facet and the second term is the component P_{11}^{I}, normal to the grain boundary ($P_{11}^{I} \approx P^{I}/3$). For fine grained materials, $\ell D_{\ell} << D_b \delta_b$, and Eq. (7) reduces to

$$\sigma_{\ell}^{i} = \left(\frac{3}{4}\right)\sigma_{\infty} - \left(\frac{2\sqrt{3}}{7\pi}\right)\frac{\ell^2 \Delta\dot{\delta} kT}{\Omega D_b \delta_b} \tag{8}$$

The constraint reduces to a lower level than given by Eq. (8) when the zone approaches a free surface or, when an array of such zones, separated by $\lesssim$ d, interact.

When the cavitation zone enlarges, such that $d \lesssim 6\ell$, an appreciable deviatoric stress develops, and the problem resembles that of a crack with diameter d, subject to opening displacements that accommodate the enhanced matter deposition along the intervening grain facets (Appendix).[33] The crack solution, pertinent to the large zone size limit, provides a constraint, given by (Appendix, Eq. (A8));

$$P_{11}^{I} = -\frac{9\sqrt{3}}{28}\,\frac{\Delta\dot{\delta}\ell^2 kT}{\Omega D_b \delta_b}\left(\frac{\ell}{d}\right) \tag{9}$$

The subsequent analysis is conducted in detail using the upper bound constraint, as pertinent to situations in which most of the rupture time is consumed while the cavitation zone is small. It is relatively straightforward to extend the analysis to include alternate constraints.

The shape change in the cavitation zone enhances the stress in the matrix (Fig. 3d). The stresses on those boundaries contiguous with the cavitating boundaries are of principal interest. These stresses derive from the continuum stresses, as redistributed by grain boundary sliding and local grain boundary diffusion. It is assumed that the stress redistribution is confined primarily to those boundaries immediately adjacent to the cavitation zone; such that the average stress on the peripheral boundaries is similar to the average continuum stress. Cavity growth in the peripheral zone is then considered to proceed at a rate dictated by this average stress. The upper bound continuum stress on the grain boundaried of the surrounding grains, subject to dilation, is;

$$\sigma_{\ell}^{o} = \left(\frac{3}{4}\right)\sigma_{\infty} + \left(\frac{P^{I}}{3}\right)\left(\frac{\ell}{x}\right)^{3} \tag{10a}$$

where x is the distance from the center of the cavitation. The first term results from the applied stress and the second term results from the constraint, as derived from the radial normal stress in an elastic medium containing a spherical cavity subject to an internal pressure, $P^{I}/3$.[39] The average stress on the first peripheral zone (x ranges from ℓ to 2ℓ) is thus;

$$\langle\sigma\rangle_{\ell}^{o} = \left(\frac{3}{4}\right)\sigma_{\infty} + \frac{P^{I}}{8} \tag{10b}$$

The equivalent solutions at the large zone limit are;

$$\sigma_{\ell}^{o} = \sigma_{\infty} + p_{11}^{I} \left\{ 1 - x/\left[x^2 - (d/2)^2 \right]^{1/2} \right\} \tag{11a}$$

$$\langle\sigma\rangle_{\ell}^{o} = \sigma_{\infty} - P_{11}^{I} \left\{ 1 - \left[2(d+2\ell) \sqrt{(\ell^2+\ell d)} + d^2 \ell n \left(\frac{d+2\ell+2\sqrt{(\ell^2+\ell d)}}{d} \right) \right] \Big/ \left[4\ell(\ell+d) \right] \right\} \tag{11b}$$

3. CAVITY GROWTH

3.1 General Considerations

In order to model the growth of cavities, consider for simplicity the perfect hexagonal grain arrangement with a plane strain geometry and cavities of center to tip distance, a, and center to center spacing, 2b (=ℓ). The nucleation of cavities at a triple junction is assumed for present purpose to occur, quite readily, at junctions between boundaries with atypical diffusivities or dihedral angle. For fine-grained polycrystals the mass transport rate by volume diffusion is relatively small[40,41] and is neglected in the present analysis. The matter which diffuses from the cavity surfaces is assumed to diffuse along the grain boundary connecting the cavity array, such that the grain boundary thickening is spatially uniform (uniform thickening pertains because the transient time to reach steady state is relatively short for fine grained polycrystals[42]).

The problem of cavity nucleation has been studied by several workers.[43-46] It is simply noted here that triple junction nucleation can occur at relatively low stress levels (typical of the applied stresses employed in creep tests) when the local dihedral angle, Ψ. is small (e.g., $\Psi \sim 80^{o}$; as observed for Al_2O_3)[2]. Nucleation is thus expected to occur soon after the application of stress at that fraction of grain junctions comprising low local dihedral angles. Some subsequent nucleation at more resistant triple junctions (due to grain boundary sliding instabilities) may also occur. But, in the present analysis, the observed differences in cavity size are considered to

derive predominantly from differences in cavity growth rate, rather than from different nucleation times.

The cavities given initial consideration are equilibrium-shaped cylindrical cavities at triple junctions (Fig. 4a). This configuration is presumably preceded by spheroidal cavities along three grain junctions or at four grain junctions.[2] However, equilibrium shaped cavities extend rapidly after initial nucleation, and their growth into a cylindrical shape is assumed to provide an insignificant contribution to the cavity evolution time.

The equilibrium cavities are expected to exhibit a transition to crack-like cavities (Fig. 4b) as they extend along the intervening grain boundary. Chuang et al.[34] examined the entire spectrum of interfacial void shapes in diffusive cavitation and concluded that, in the absence of constraint, the transition occurs when the velocity computed for the crack-like cavities exceeds the equilibrium cavity velocity. The transition subject to constraint is undoubtedly more complex, but will presumably proceed in accord with the same velocity criterion, provided that the transition also results in a reduced constraint.

The system considered for the present analysis consists of several contiguous boundaries that exhibit atypical diffusivities D_b' or D_s' (relative to the average diffusivities D_b or D_s) or a low dihedral angle, Ψ'. Cavities are assumed to nucleate and grow uniformly at each triple junction encompassed by these boundaries.

3.2 Derivation of Governing Equations

When the grain boundary is subject to a normal tensile stress

$\sigma(x)$ the chemical potential of the atoms at the grain boundary is[47]

$$\Delta\mu = -\sigma\Omega \tag{12}$$

and it is known from diffusion theory that the difference in chemical potential gives the driving force for atom diffusion. The flux law has the form

$$J_b = \frac{D_b'\delta_b}{kT}\frac{d\sigma}{dx} \tag{13}$$

where J_b is the atom flux in the grain boundary and D_b' is the local grain boundary diffusivity. The atoms deposit at the grain boundary, forming a layer of uniform width, $\Delta\delta$. It thus follows from matter conservation requirement that

$$\frac{\partial\Delta\delta}{\partial t} = -\Omega\frac{\partial J}{\partial x} \tag{14}$$

Substitution of the grain boundary flux (Eq. (13)) into Eq. (14) yields a relationship between the grain boundary thickening, $\Delta\delta$, and normal tensile stress, σ.

$$\frac{d^2\sigma}{dx^2} = -\frac{\dot{\Delta\delta}kT}{D_b'\delta_b\Omega} \tag{15}$$

Solving the differential equation subject to the boundary conditions that the stress is symmetric at the midpoint, x = b, and that the stress is continuous at the cavity tip, x = a,

$$\sigma'(b) = o \qquad \text{and} \qquad \sigma(a) = \sigma_o$$

where σ_o is the sintering stress at the cavity tip, lead to

$$\sigma(x) = -\frac{\Delta\dot{\delta}kT}{2D_b\delta_b\Omega} x^2 + \frac{\Delta\dot{\delta}kT}{D_b\delta_b\Omega} bx + \sigma_o + \frac{\Delta\dot{\delta}kT}{D_b\delta_b\Omega} b^2\left(\frac{f^2}{2} - f\right) \quad (16)$$

where $f = a/b$. The condition of mechanical equilibrium requires

$$b\sigma_\ell = \int_a^b \sigma(x)\, dx \quad (17)$$

substituting Eq. (16) into Eq. (17) gives;

$$\frac{\sigma_\ell}{b^2} = \frac{\sigma_o}{b^2}(1-f) + \frac{\Delta\dot{\delta}kT}{D_b\delta_b\Omega} \frac{(1-f)^3}{3} \quad (18)$$

Recalling that the local stress can be related to the applied stress and the thickening rate by Eq. (8), it becomes possible to solve for both the local stress and the cavity growth rate. Solutions are obtained for both equilibrium cavity growth (cavities with a uniform curvature) and for crack-like cavity growth (a condition under which there is insufficient time for a cavity to develop a rounded shape and instead, remains thin and crack-like).

3.3 Equilibrium Cavities

The sintering stress is given by[47]

$$\sigma_o = \gamma_s C \quad (19)$$

where γ_s is the surface energy and C is the curvature evaluated at the cavity tip. For the equilibrium cavity, the sintering stress can be expressed by

$$\sigma_o = 2\gamma_s h(\Psi)/\sqrt{3}\, a \quad (20)$$

where $h(\Psi) = \sin[\Psi/2 - \pi/6]$

Matter conservation requires that, for unit width of the cavitation zone,

$$\dot{V}_{eqm} \approx \Delta\dot{\delta}\ell \tag{21}$$

where $\dot{V}$ is the rate of volume change of an individual cavity. The volume of an equilibrium-shaped, cylindrical, triple junction cavity is (for unit width)

$$V = 3\sqrt{3}\, a^2\, F(\Psi)/4 \tag{22}$$

where $F(\Psi) = 1 + \dfrac{\sqrt{3}\,[\Psi - \pi/3 - \sin(\Psi-\pi/3)]}{2\sin^2(\Psi/2 - \pi/6)}$.

The rate of volume change is thus;

$$\dot{V}_{eqm} = 3\sqrt{3}\, a\, \dot{a}_{eqm}\, (F(\Psi)/2) \quad . \tag{23}$$

The cavity velocity is related to the additional matter deposition, from Eqs. (21) and (23) by;

$$\Delta\dot{\delta} = (3\sqrt{3}/4)\, \dot{a}_{eqm}\, f\, F(\Psi) \tag{24}$$

Substituting Eq. (24) into Eq. (18), the growth rate of the cavity in an inhomogeneous region with a local grain boundary diffusivity, D_b', is

$$\dot{a}_{eqm} = \frac{16\Omega D_b'\delta_b}{\sqrt{3}kT\ell^2}\, \frac{\sigma_\ell^{\,i} - \sigma_o(1-f)}{F(\Psi)\, f(1-f)^3} \tag{25}$$

The magnitude of the local stress pertinent to Eq. (25) is deduced by noting that the matter deposition given by Eq. (24) must be compatible

with the development of the local stress induced by the constraint of the surrounding material. Using the upper bound constraint (Eq. (8)) pertinent to a small cavitation zone (e.g. Fig. 3), the local stress becomes;

$$\sigma_\ell = \left[(3/4)(1-f^3)\sigma_\infty + (24\sqrt{3}/7\pi)(D_b'/D_b)(1-f)\sigma_o\right] \Big/ \left[(1-f)^3 + (24\sqrt{3}/7\pi)(D_b'/D_b)\right] \quad (26)$$

Substituting the sintering stress and the local stress from Eqs. (20) and (26) into Eq. (25) the final relation for the cavity velocity, expressed in dimensionless form, becomes;

$$\dot{a}_{eqm}\left(\frac{kT\ell^3}{\delta\Omega D_b \delta_b \gamma_s}\right) = \frac{(16/\sqrt{3})[(3/4)(\sigma_\infty \ell/\gamma_s)f - (4/\sqrt{3})h(\Psi)(1-f)]}{F(\Psi)f^2[(1-f)^3(D_b/D_b') + (24\sqrt{3}/7\pi)]} \quad (27)$$

3.4 Crack-like Cavities

The analysis of crack-like cavity growth is facilitated by noting that both the cavity profile and the atom flux at the tip of well developed crack-like cavities depend on the instantaneous cavity velocity; viz. the prior, equilibrium morphology of the cavity is of minor significance.[34,43] The growth process can thus be adequately treated by focussing on the tip region, and neglecting complex morphological changes that may be occurring in the vicinity of the cavity center. Also, for present purposes the meniscus instability is neglected, because the wavelengths needed to permit the growth of perturbations is larger than the grain facet dimension for typical fine grained ceramics.[2]

Commencing with the expression for the curvature and the surface flux at the tip of a crack-like cavity[34]

$$C = 2 \sin(\Psi/4) \dot{a}_{crack}^{1/3} (kT/D_s\delta_s\Omega\gamma_s)^{1/3} \tag{28}$$

$$J_s = 2 \sin(\Psi/4) \dot{a}_{crack}^{2/3} (D_s\delta_s\gamma_s/kT\Omega^2)^{1/3} \tag{29}$$

where $D_s\delta_s$ is the surface diffusion parameter. Substituting Eq. (28) into Eq. (19), the sintering stress of the crack-like cavity becomes

$$\sigma_o = 2\gamma_s \sin(\Psi/4)(\dot{a}_{crack}\, kT/D_s\delta_s\Omega\gamma_s)^{1/3} \tag{30}$$

The matter removed from the cavity tip must be deposited on the grain boundary, in order to satisfy matter conservation; hence,

$$2J_s\Omega = \Delta\dot{\delta}\ell/2 \tag{31}$$

Combining Eq. (29) with Eq. (31), the boundary thickening rate becomes;

$$\Delta\dot{\delta} = 8 \sin(\Psi/4) \dot{a}_{crack}^{2/3} (D_s\delta_s\Omega\gamma_s/kT\ell^3)^{1/3} \tag{32}$$

Substituting Eqs. (30) and (32) into Eq. (18), the growth rate of the crack-like cavity in an inhomogeneous region, with a grain boundary diffusivity D_b', is;

$$\dot{a}_{crack} = \frac{D_s\sigma_s\Omega\gamma_s}{kT} \left\{ \frac{-1+[1+(2/3)(1-f)(D_s\delta_s/D_b'\delta_b)(\ell\sigma_\ell/\gamma_s \sin(\Psi/4))]^{1/2}}{(2/3)(1-f)^2\ell(D_s\delta_s/D_b'\delta_b)} \right\}^3 \tag{33}$$

Combining Eq. (32) with the relation for the local constraint, Eq. (8), yields the equation

$$\sigma_\ell = \left(\frac{3}{4}\right)\sigma_\infty - (16\sqrt{3}/7\pi)\sin(\Psi/4)(D_s\delta_s/D_b\delta_b)$$

$$\dot{a}^{2/3}_{crack}\,\gamma_s\ell\,(kT/D_s\delta_s\Omega\gamma_s)^{2/3} \tag{34}$$

Note that Eqs. (33) and (34) express the relation between the cavity velocity and the local stress. Combining the two equations permits the explicit determination of the cavity velocity and the local stress. For example, the velocity is given by;

$$v^{2/3}\Delta^{1/3}\left[(2/3)(1-f)^3(D_b/D_b') + (16\sqrt{3}/7\pi)\right] + 2v^{1/3}(1-f)\Delta^{-1/3} = (3/4)\,\sigma_\infty\ell/\gamma_s\,\sin(\Psi/4) \tag{35}$$

where $v = \dot{a}_{crack}(kT\ell^3/D_b\delta_b\Omega\gamma_s)$ and $\Delta = D_s\delta_s/D_b\delta_b$. However, in order to obtain a simple analytic expression for the cavity velocity and the local stress, some approximations are made. The parameters $\sigma_\infty\ell/\gamma_s$ and D_b'/D_b are typically ≥ 1, whereupon Eq. (35) reduces to

$$v = \frac{[(21\pi/256\sqrt{3})\;\sigma_\infty\ell/\gamma_s\;\sin(\Psi/4)]^{3/2}}{\Delta^{1/2}} \times \left\{1 - \left[\left(\frac{(7\sqrt{3}\pi/12)\gamma_s\sin(\Psi/4)}{\sigma_\infty\ell}\right)\;\frac{1}{\Delta}\right]^{1/2}(1-f)\right\} \tag{36a}$$

which, upon further simplification, becomes

$$v^{2/3} \approx \frac{0.15[\sigma_\infty\ell/\gamma_s\;\sin(\Psi/4)]}{\Delta^{1/3}} \tag{36b}$$

An almost steady velocity is thus anticipated in the crack-like region during initial cavitation. However, when the constraint is reduced in the later stages of cavitation, cavity acceleration is to be anticipated and Eq. (36) should not be used. The equivalent expression for the local stress is;

$$\frac{\sigma_{\ell}^{i}}{\sigma_{\infty}} = \frac{(\sqrt{3}/4)(1-f)[(7\pi/\sqrt{3})(\sigma_{\infty}\ell/\gamma_s \sin(\Psi/4))\Delta]^{1/2}}{\Delta\sigma_{\infty}\ell/\gamma_s \sin(\Psi/4)}$$

$$\frac{-(7\pi/16\sqrt{3})(1-f)^2}{} \qquad (37)$$

3.5 Velocity Trends

The solutions given in Eqs. (26), (27), (36) and (37) are based on the assumptions that the cavities grow with either an equilibrium shape or a crack-like shape, respectively. Chuang et al.'s criterion[34] can be used to consider the transition between the two shapes, which requires the transition to occur when the crack-like cavity velocity exceeds the equilibrium cavity velocity.

The local stress and the velocity of equilibrium cavities from Eqs. (26) and (27) and the exact solutions for crack-like cavities from Eqs. (33) and (34) are shown in Fig. 5, (where the two limiting cases are plotted for $\sigma_{\infty}\ell/\gamma_s = 20$, $\Delta = 0.5$ and $\Psi = 80^{o}$ as the data are pertinent to Al_2O_3 for diffusive creep). It is seen from Fig. 5a that when the applied stress is high enough to overcome the sintering stress, the cavity starts to grow and possesses an equilibrium shape. As the equilibrium cavity grows, the cavity velocity is affected by two factors; (a) the sintering stress, which is decreased by the cavity growth (Eq.(20))

and tends to increase the cavity velocity, and (b) the local stress, which decreases as the cavity grows (Eq. (18)) and tends to retard the cavity growth. At the cavity nucleation size the sintering stress is important and the cavity velocity increases rapidly up to a maximum value. Then, the constraint dominates and reduces the cavity velocity. On the other hand, the crack-like cavity velocity maintains an approximately constant value. Thus, as the equilibrium cavity grows to a transition size f^*, the crack-like cavity velocity exceeds the equilibrium cavity velocity (Fig. 5a). A reduced constraint obtains for the crack-like morphology (Fig. 5b). The transition to crack-like cavities is thus considered favorable when the crack-like velocity exceeds that for equilibrium cavities, and the local stress is assumed to adjust to this crack-like value, over the transition range.

The important trends in cavity velocity with cavity length, d, and with the dominant variables ($\sigma_\infty \ell/\gamma_s$, Ψ and Δ) are illustrated in Fig. 6.

Firstly, the strong influence of the constraint upon initial cavitation is noted (Fig. 6a). The effect of the constraint is manifest at the very earliest stages of cavity growth and continues to be amplified as the extension proceeds. As the cavitation region enlarges the constraint becomes smaller and the local stress becomes larger, hence the cavity velocity increases. It is also re-emphasized that the development of constraint leads to a relatively invariant cavity velocity in the crack-like regime. Secondly, the magnitude of the applied stress (Fig. 6b) has a substantial effect on the cavity velocity, over the entire range. The higher the applied stress, the higher the cavity

velocity. However, other notable effects of the stress include the decrease in transition size, f^*, as observed experimentally,[2] and the substantial reduction in the critical nucleation size, f_o. Setting $\dot{a}_{eqm}$ to zero in Eq. (27), the relative nucleation size is;

$$f_o = \left[1 + \frac{3\sqrt{3}}{16 \sin(\Psi/2-\pi/6)} \left(\frac{\sigma_\infty \ell}{\gamma_s}\right)\right]^{-1} \tag{38}$$

Thirdly, the material parameter, Ψ, the local value of the dihedral angle, has a dominant influence upon inhomogeneous cavitation (Fig. 6c). Specifically the growth of cavities with a small dihedral angle requires the removal of relatively small quantities of material; consequently, the cavity velocity increases as the dihedral angle decreases. Finally, the ratio Δ of the surface to boundary diffusity affects the cavity velocity (Fig. 6d) such that cavity growth in the crack-like mode is favored when grain boundary diffusion is more rapid than surface diffusion (i.e., when Δ is small).[34]

The local grain boundary diffusivity has a negligible influence on the cavity velocity. However, variations in this diffusivity would exert a much more significant influence on cavity growth at smaller values of cavity spacing. The transition, f^*, between the equilibrium and crack-like modes of cavity growth predicted by the above analysis can be compared with experimental data[2] obtained for Al_2O_3. The prediction, illustrated in Fig. 7 for $\Psi = 80^o$ and $\Delta = 0.5$, appears to adequately separate observations of the two cavity types; hence, some credence in the preceding analysis is established.

4. PROPAGATION TIME

The time taken for cavities to extend across grain facets is of principal importance for the creep rupture process. If cavity nucleation occurs soon after steady state is established, the time t_p needed to create a cavity of relative length f is simply,

$$2t_p/\ell = \int_{f_o}^{f^*} \frac{df}{\dot{a}_{eqm}} + \int_{f^*}^{f} \frac{df}{\dot{a}_{crack}} \quad . \tag{39}$$

By using $\dot{a}_{eqm}$ from Eq. (27) and $\dot{a}_{crack}$ from Eq. (35) and solving the integral numerically, some typical dimensionless propagation times are obtained as plotted in Fig. 8. The variation of propagation time with cavity length for $\Psi = 80^o$, $\sigma_\infty \ell/\gamma_s = 20$ and $\Delta = 0.5$ is shown in Fig. 8a. When the dihedral angle or the local surface diffusivity decrease and/or the applied stress increases, the cavity velocity increases (Sec. 3.4); hence, the propagation time decreases, as shown in Figs. 8b, 8c and 8d (for f=1). In the above cases, the transition to the crack-like mode occurs rapidly and most of the time required to develop a full facet length cavity is dictated by the growth in the crack-like mode (as might be anticipated from the velocity diagrams). The initial cavitation that occurs in local regions of a creeping polycrystal (due to small local values of Ψ or D_s) can thus be approximately characterized by the constant velocity relation (Eq. 36b); whereupon the propagation time becomes;

$$t_p \approx 20 \left(\frac{kT\ell^4}{D_b \delta_b \gamma_s \Omega} \right) \Delta^{1/2} \left(\frac{\gamma_s \sin(\Psi/4)}{\sigma_\infty \ell} \right)^{3/2} \tag{40}$$

If the initial cavitation consumes the major portion of the rupture process, Eq. (40) will also provide an approximate estimate of the failure time. However, the conditions wherein this approximation obtains can only be ascertained by examining the subsequent cavity evolution, as manifest in the zone spreading process.

5. ZONE SPREADING

The incidence of zone spreading is contingent upon the development of enhanced tensions and thus, accelerated cavity growth, around the periphery of the cavitation zone. Cavitation firstly occurs along several contiguous boundaries for which one (or both) of the parameters that dominate the cavitation rate (Ψ or D_s) deviates from the average value. The local stress outside the cavitation zone, on the contiguous boundaries, is larger than the applied stress (Fig. 9). The cavitation rates in this peripheral zone are presumably non-uniform. A complete solution of peripheral cavity growth is beyond the scope of the present work. Instead, a simplified intermittent spreading procedure is adopted. Cavity growth in each peripheral zone is assumed to occur uniformly (i.e., two uniformly approaching cavities on each peripheral boundary, Fig. 9) at a stress equal to the average stress over that boundary, determined from Eq. (10b), while cavitation on the original boundary continues at the initially deduced local stress. Then, at a time t^* when the cavity lengths in the cavitation zone and in the peripheral zone become equal (Fig. 10), the cavitation zone is considered to advance to the boundary of the peripheral zone. The process is then continued by considering the growth in the next peripheral zone, with a new value of the local stress assigned to the cavitation zone (based on the increase in the zone size, d). Proceeding in this way the time t_i needed to form a discrete macrocrack can be deduced, as schematically shown in Fig. 10. The cavity velocity in the first peripheral zone is deduced by substituting $\langle\sigma\rangle^o_\ell$ from Eq. (10b) for σ_∞ in Eq. (27) (the equilibrium regime) or Eq. (35) (the crack-like regime).

The cavity propagation times are compared in Fig. 11 with those on the initial boundary for several choices of Ψ', Ψ, D_s and D_s'.

Some general cavitation characteristics are established before examining the zone spreading process. Firstly, small local surface diffusivities cannot be the source of preferred cavitation, because the equilibrium cavity growth process is independent of D_s (although earlier transitions to crack-like cavitation can certainly be attributed to deviations in D_s). A prerequisite for the appearance of preferred cavitation is thus the existence of a dihedral angle smaller than the average value. Zone spreading considerations are therefore based on the premise that initial cavity development on certain boundaries resides in a small dihedral angle. However, subsequent cavity development on these boundaries can be further enhanced by small surface diffusivities.

The zone spreading process can be conveniently separated into three regimes. Firstly, when the deviations in Ψ and D_s are small, and the absolute values are close to the average values for the material, zone spreading occurs very rapidly, while the cavities are still quite small (Fig. 11a). Failure from these regions is expected to occur quite slowly, at a rate similar to that for homogeneous material. Conversely, when there are appreciable local deviations in both Ψ and D_s, a cavity can extend fully across a grain facet before significant cavitation can be induced on the contiguous boundaries (Fig. 11b). The cavitation can then be regarded as an essentially independent process. This cavitation regime is likely to pertain to isolated

regions† during the early stages of failure, and explains the observation of premature full-facet sized cavities.[2] Again, however, this mode of cavitation has little influence upon the failure process, because the full-facet cavities have a minor effect on cavitation in the contiguous boundaries and do not, therefore, lead to the generation of macrocracks (as noted experimentally).[2] An intermediate regime, that consists of appreciable deviations in Ψ, but small deviations in D_s, is of principal importance with regard to failure (Fig. 11c). Cavity propagation and coalescence under these conditions occurs most rapidly. Such regions are thus considered to be the principal sites for failure initiation.

The trends in constraint during zone spreading suggest that a large proportion of the failure time in the intermediate region should be consumed while cavitation is confined to a small number of contiguous grain facets. The approximate expression for the failure time (Eq. (40)) that pertains during this period should thus provide a first-order estimate of failure. Comparing this relation with that for diffusive creep (Eq. (1)), the following expression for the failure time, t_f, emerges;

$$t_f \dot{\varepsilon}_\infty \approx 50\pi(\gamma_s/\sigma_\infty \ell)^{1/2} \sin(\Psi/4)^{3/2} (D_s\delta_s/D_b\delta_b)^{1/2} \qquad (41)$$

The analysis thus anticipates a strong interdepedence of the failure time and the steady-state creep rate, as generally observed

---

†The number of these regimes would be dictated by the probability of locating a boundary with small values of both Ψ and D_s, based upon the appropriate statistical distributions of Ψ and D_s.

(the Monkman-Grant relationship);[48] although an additional dependence of the failure time on the stress $(\gamma_s/\sigma_\infty \ell)^{1/2}$ emerges from the present analysis. Important effects of the local dihedral angle and of the diffusity ratio are also predicted, in the sense that small values of these parameters encourage failure.

6. DISCUSSION AND CONCLUSIONS

The cavitation process in ceramic polycrystals is observed to be inhomogeneous, resulting from the presence of local variability in material properties, especially in the dihedral angle, Ψ, or in the diffusivity along the newly created cavity surfaces, D_s. Such variability in Ψ or D_s could arise from crystalline anisotropy, but appreciable effects of impurities may also be involved. The excess matter deposition from the cavitation induces constraints which retard the cavitation rate and contribute importantly to the rupture time. The magnitude of the constraint is dictated by the rate of cavity volume change relative to the viscous relaxation rate (associated with the creep of the surrounding material). Additionally, the constraint depends upon the morphology of the cavitation zone. Two limiting cases, the equilibrium cavity and the crack-like cavity are of practical importance. The transition is considered to occur when the crack-like cavity velocity exceeds the equilibrium cavity velocity and less constraint is derived from the transition. The failure characteristics exhibited by a material depend on the extent of the deviations in D_s or Ψ. Three possibilities are considered.

Large local deviations in the dihedral angle and in the diffusivity appear to be relatively innocuous, because the isolated full-facet sized cavities which form in these regions do not enhance the cavitation rate on contiguous boundaries. However, if there are a relatively large proportion of boundaries with a high cavitation susceptibility, premature failure may occur from contiguous accumulations of these boundaries.

The probabilistic aspects of failure under similar conditions have been examined by Evans.[3]

Exclusion of failure from large statistical accumulations of susceptible boundaries results in a creep rupture process dominated by cavity propagation in regions containing several contiguous boundaries with significant deviations in dihedral angle (and small deviations in the diffusivity along the cavity surfaces created at the boundary). The failure time that obtains under these conditions may be approximately expressed by Eq. (40); a result that indicates important influences on rupture of the steady-state creep rate (i.e., Monkman-Grant behavior), the local dihedral angle Ψ and the ratio of the surface to the boundary diffusivity, D_s/D_b. Small values of Ψ or D_s/D_b encourage creep rupture. Such effects should be apparent in creep rupture experiments. It has already been observed, in fact, that cavitating boundaries in Al_2O_3 exhibit smaller dihedral angles than those typically measured during sintering or grain boundary grooving experiments[2] ($\sim 80^o$ compared with $100\text{-}120^o$).

In materials of relative uniformity, cavitation is expected to develop homogeneously, by virtue of a rapid zone spreading process. The stress in these regions thus remains at a level essentially similar to the applied stress. Homogeneous cavitation models that exclude an explicit dependence on the steady-state creep rate are then most pertinent. The cavitation rate exceeds that in materials containing regions of low Ψ and/or D_s, because the more rapid cavitation associated with the smaller Ψ or D_s is not sufficiently counteracted by the development of constraint. This trend is evident from a comparison of cavity

propagation times in regions with a relatively uniform, average dihedral angle (Fig. 11a) and regions with a particularly low dihedral angle (Fig. 11c). However, probabilistic studies of the distribution of grain boundary properties are needed in order to distinguish the principal modes of creep rupture experienced by specific ceramic polycrystals.

Finally, some correlations between creep rupture and sintering are examined. As low ratio of the surface to boundary diffusivity is a prerequisite for initial stage sintering.[49] Most ceramic polycrystals should thus be susceptible to the cavitation failure processes described in this work. Also, it is probable that regions of a polycrystalline aggregate that are the last to sinter to full density are also the regions subject to cavitation during creep. Pore removal rates during final stage sintering can be determined by setting σ_∞ to zero in Eq. (27):

$$\dot{a}_{sinter} = - \frac{64 \sin(\Psi/2 - \pi/6)(1-f)}{3F(\Psi)f^2 \left[(1-f)^3(D_b/D_b) + (24\sqrt{3}/7\pi)\right]} \qquad (42)$$

Some typical sintering characteristics are plotted in Fig. 12.

Inspection of Fig. 12 indicates that pores with small dihedral angles, $\Psi \to \pi/3$, will be removed very slowly; cavities which, as already noted, extend most rapidly. Such regions are the principal candidates for creep rupture initiation. It may be surmised, therefore, that the addition of solutes that enlarge the dihedral angle should encourage final stage sintering as well as retarding creep rupture. Prospects for identifying solutes with this capability should be explored in future studies.

APPENDIX

CONSTRAINT ON THE CAVITATION ZONE

The constraint exerted on a zone subject to a transformation strain e^T_{ij} can be conveniently separated into dilational p^I and deviatoric component $'p^I_{ij}$. The dilational constraint is independent of the zone size and is given for an elastic solid by;[38]

$$p^I = - \frac{e^T}{1/\left(4\ \mu_m\right) + 1/\left(3\kappa_p\right)} \tag{A1}$$

where μ is the shear modulus, κ is the bulk modulus and the subscripts p and m prefer to the material inside and outside the transformation zone, respectively. The deviatoric constraint is shape dependent. For example, the deviatoric constraint associated with a spherical zone is given by;[38]

$$'p^I_{ij} = - \frac{'e^T_{ij}}{1/\left(2\ \mu_p\right) + (4-5\nu_m)/\left[(7-5\nu_m)\ \mu_m\right]} \tag{A2}$$

where ν is Poisson's ratio. The relative influence of the dilational and deviatoric constraints on the stress normal to the grain boundaries (the driving force for cavitation) depends on the grain boundary orientations within the zone (which determines the unconstrained transformation strains ε^T_{11}, ε^T_{22}, ε^T_{33}, Fig. 3b) and on the zone shape.

For the grain boundary orientations and zone shape depicted in Fig. 3 the stress is dominated by the dilational transformation strain. Specific calculations conducted using the Eshelby tensor for an ellipsoidal cavitation zone (Fig. 13) indicate that P^I_{11} differs from $P^I/3$ by a small amount if the cavitation zone is small. A dilation dominated

constraint can thus be considered to exist for zones of small lateral extent, typified by Fig. 3. This is the basis for the upper bound solution presented in this work.

For an elongated zone, $d>>\ell$, wherein the majority of grain boundaries subject to enhanced matter deposition are nearly normal to the applied stress, the constraint is simulated by the solution of a disc-shaped crack with diameter d in a homogeneous linear elastic solid;[33]

$$p_{11}^{I} = - \frac{3\pi\mu<\Delta\delta>}{4(1-\nu)d} \tag{A3}$$

where $<\Delta\delta>$ is the average matter deposition along the cavitation zone. This solution approximates the constraint level attained within transformation zones of lateral extent $d\tilde{>}6\ell$ (Fig. 13).

By the analogy between linear elastic and linear viscoelastic materials,[36] the equivalent solution for a viscous solid which exhibits diffusive creep can be obtained if μ is replaced by ηs and ν by $(3\kappa - 2\eta s)/(6\kappa + 2\eta s)$, where s is given by the Laplace transform;

$$\bar{F}(s) = \int_0^\infty e^{-st} F(t)dt \tag{A4}$$

Eqs. (A1) and (A3) can thus be directly transformed into the equivalent viscous equation

$$\bar{p}^{I} = \frac{- \bar{e}^{T}}{\frac{1}{4\eta s} + \frac{1}{3\kappa_p}} \tag{A5}$$

for zones of small lateral extend and,

$$p_{11}^{-I} = -\frac{3\pi\eta s\langle\overline{\Delta\delta}\rangle}{4d}\ \frac{6\kappa + 2\eta s}{3\kappa + 4\eta s} \tag{A6}$$

for elongated zones.

By setting $\kappa = \infty$, Inversion then gives;

$$p^{I} = -4\eta_m \dot{e}^{T} \tag{A7}$$

for zones of small lateral extent and,

$$p_{11}^{I} = 3\pi\eta_m \dot{\Delta\delta}/2d \tag{A8}$$

for elongated zones.

REFERENCES

1. G. W. Greenwood, Fracture 1977, ICF4 1, (1977) 293.
2. J. R. Porter, W. Blumental and A. G. Evans, to be published.
3. A. G. Evans and A. S. Rana, Acta Met. 28 (1980) 129.
4. B. F. Dyson and D. McLean, Metal Sci. J. 6 (1972) 220.
5. R. C. Folweiler, J. Appl. Phys. 32 (1961) 773.
6. G. W. Greenwood, Acta Met. 2 (1954) 250.
7. R. M. Cannon, W. H. Rhodes and A. H. Heuer, J. Am. Ceram. Soc. 63 (1980) 46.
8. D. Hull and D. E. Rimmer, Phil. Mag. 4 (1959) 673.
9. J. Weertman, Scri. Met. 7 (1973) 1129.
10. F. H. Vitovec, J. Mat. Sci. 7 (1972) 615.
11. M. V. Speight and J. E. Harris, Metal Sci. J. 1 (1967) 83.
12. T. J. Chuang and J. R. Rice, Acta Met. 21 (1973) 1625.
13. V. Vitek, Acta Met. 26 (1978) 1345.
14. G. M. Pharr and W. D. Nix, Acta Met. 27 (1979) 1615.
15. M. V. Speight, W. B. Beere and G. Roberts, Mater. Sci. Eng. 36 (1978) 155.
16. R. Raj and M. F. Ashby, Met. Trans. 2 (1971) 1113.
17. T. G. Langdon, Phil. Mag. 22 (1970) 689.
18. J. R. Spingarn, D. M. Barnett and W. D. Nix, Acta Met. 27 (1979) 1549.
19. W. D. Nix, D. K. Matlock and R. J. Dimelfi, Acta Met. 25 (1977) 495.
20. A. Needleman and J. R. Rice, Acta Met. 28 (1980) 1315.
21. R. Raj and A. K. Rhosh, Acta Met. 29 (1981) 283.

22. F. W. Crossman and M. F. Ashby, Acta Met. 23 (1975) 425.

23. W. Beere and M. V. Speight, Metal Sci. 12 (1978) 172.

24. D. A. Miller and T. G. Langdon, Scri. Met. 14 (1980) 179.

25. G. H. Edward and M. F. Ashby, Acta Met. 27 (1979) 1505.

26. W. Beere, Acta Met. 28 (1980) 143.

27. P. G. Shewmon, Diffusion in Solid, (McGraw-Hill, New York) 1963.

28. R. M. Cannon, Ph.D. Thesis, MIT (1975)

29. A. K. Ghosh and R. Raj, Acta Met. 29 (1981) 607.

30. J. H. Schneibel, R. L. Coble and R. M. Cannon, Acta Met. 29 (1981) 1258.

31. S. Johnson and A. G. Evans, to be published.

32. B. F. Dyson, Metal Sci. 10 (1976) 349.

33. J. R. Rice, Acta Met. 29 (1981) 675.

34. T. J. Chuang, K. I. Kagawa, J. R. Rice and L. B. Sills, Acta Met. 27 (1979) 265.

35. J. D. Eshelby, Proc. Roy. Soc. 241A (1957) 376.

36. Schaum's outline series, Theory and Problems of Continuum Mechanics.

37. A. G. Evans, J. R. Rice and J. P. Hirth, J. Am. Ceram. Soc. 63 (1980) 368.

38. A. G. Evans and A. H. Heuer, J. Am. Ceram. Soc. 63 (1980) 241.

39. S. P. Timoshenko and J. N. Goodier, Theory of Elasticity, (McGraw-Hill, New York) 1951.

40. R. L. Coble, J. Appl. Phys. 34 (1963) 1679.

41. C. Herring, J. Appl. Phys. 21 (1950) 437.

42. R. Raj, Met. Trans. 6A (1975) 1499.

43. R. M. Cannon and A. G. Evans, to be published.

44. R. Raj and M. F. Ashby, Acta Met. 23 (1975) 653.

45. W. Pavinich and R. Raj, Met. Trans. 8A (1977) 1917.

46. R. Raj, Acta Met. 26 (1978) 995.

47. T. J. Chuang, Ph.D. Thesis, Brown University 1974.

48. C. Monkman and J. Grant, Proc. ASTM 56 (1956) 593.

FIGURE CAPTIONS

Fig. 1. A scanning electron micrograph of cavity arrays in Al_2O_3, showing preferred regions of cavitation.[2]

Fig. 2. A schematic illustrating the two dominant cavity configurations, equilibrium triple point cavities, and crack-like cavities and the nature of the transition.

Fig. 3. Schematics indicating localized diffusive flow from cavities and the resultant development of constraint (a) the grain configuration and (b) the unconstrained strain in the cavitation zone separated from the matrix (c) the constrained cavitation zone showing the regions of grain boundary sliding and intensive diffusion flow (d) the resultant stress distribution.

Fig. 4. The geometry of the cavity arrays used for analysis (a) equilibrium cavities (b) crack-like cavities.

Fig. 5. a) Cavity velocity as a function of the relative cavity length indicating the equilibrium to crack-like transition.
b) The local stress in the equilibrium and crack-like regions.

Fig. 6. Plots of cavity velocity for several choices of the important variables, (a) the effect of constraint, (b) the influence of the applied stress, (c) the effect of the dihedral angle, (d) the effect of small changes in the surface diffusivity.

Fig. 7. A comparison of crack-like and equilibrium cavity for Al_2O_3 with the predicted transition length, f^*: $\Delta = 0.5$, $\Psi = 80^o$.

Fig. 8. The cavity propagation time characteristics (a) the variation of time with cavity length, (b) the effect of strain on the time taken to reach f = 1.0, (c) the effect of dihedral angle, and (d) the influence of surface diffusivity.

Fig. 9. A schematic indicating the cavitation and peripheral zones considered in the analysis.

Fig. 10. A schematic indicating the stages of zone spreading through three peripheral zones, prior to coalescence.

Fig. 11. The zone spreading process characteristics (a) small deviations in Ψ and D_s, (b) large deviations in Ψ and D_s, (c) appreciable deviations in Ψ, but small deviations in D_s: $\sigma_\infty \ell/\gamma_s = 20$.

Fig. 12. Sintering characteristics (a) the variation of pore shrinkage time with pore length for $\Psi = 80^o$ (b) the effect of Ψ on the pore shrinkage time for f = 0.1.

Fig. 13. A plot of the normalized constraint $p^I_{11}/\mu e^T$ as a function of the shape of the cavitation zone, for $\nu = 1/2$ and $e^T_{33} = e^T_{22} = \sqrt{3}\, e^T_{11}$. Also shown are the limit solutions for a dilational zone and a crack-like zone.

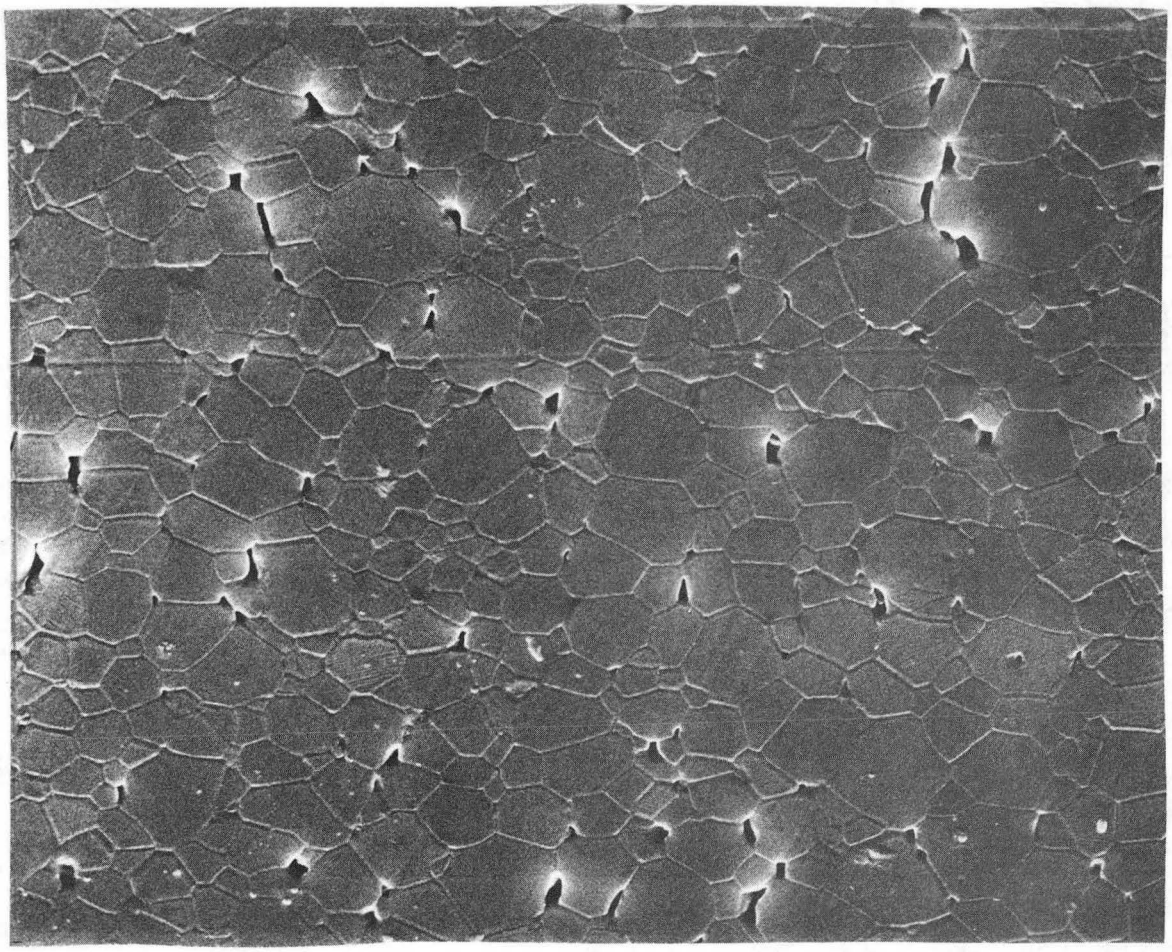

XBB 804-4499

Fig. I-1

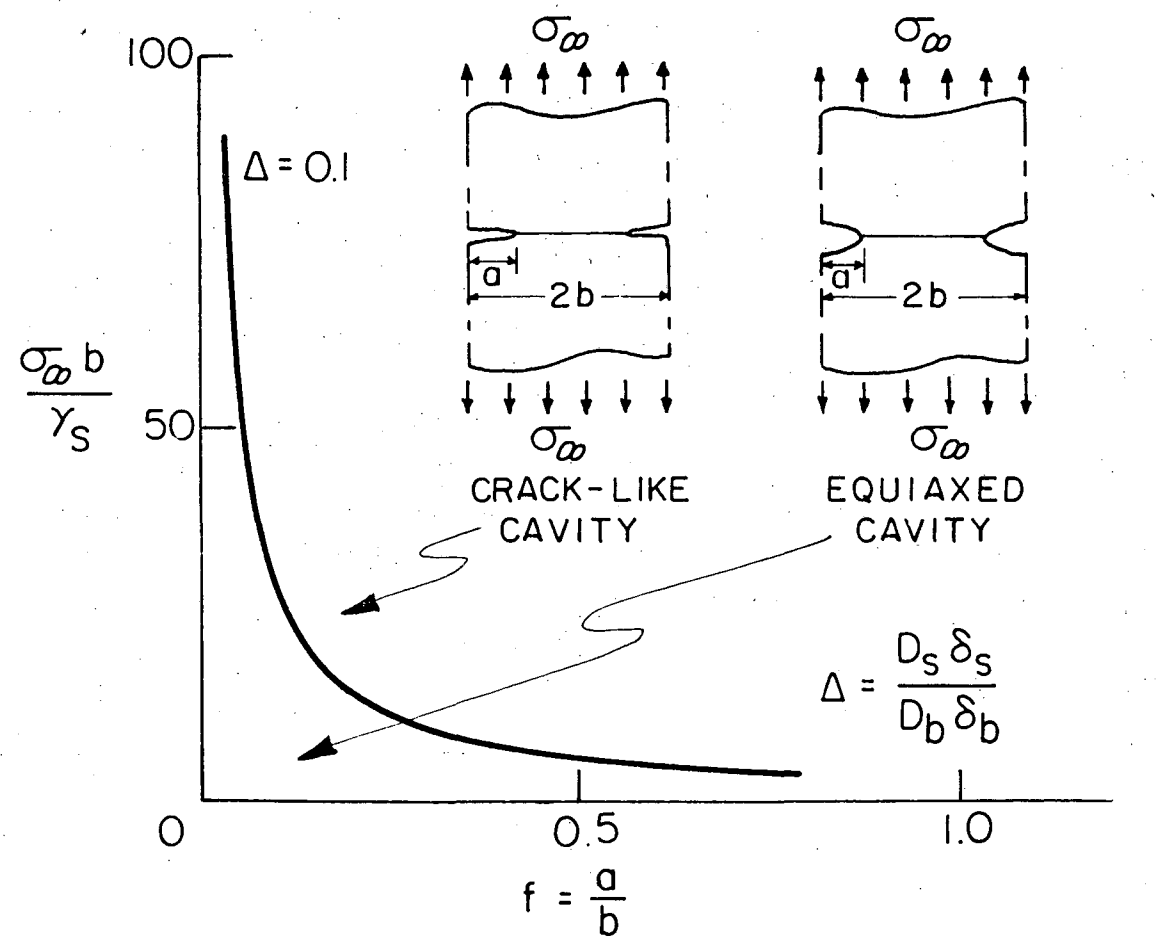
100
50
0
0.5
1.0
$\frac{\sigma_\infty b}{\gamma_s}$
$f = \frac{a}{b}$
$\Delta = 0.1$
σ_∞
a
2b
CRACK-LIKE CAVITY
EQUIAXED CAVITY
$\Delta = \frac{D_s \delta_s}{D_b \delta_b}$
XBL8110-6664

Fig. I-2

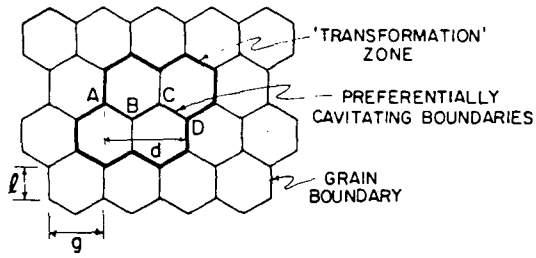

a) INITIAL CONDITION

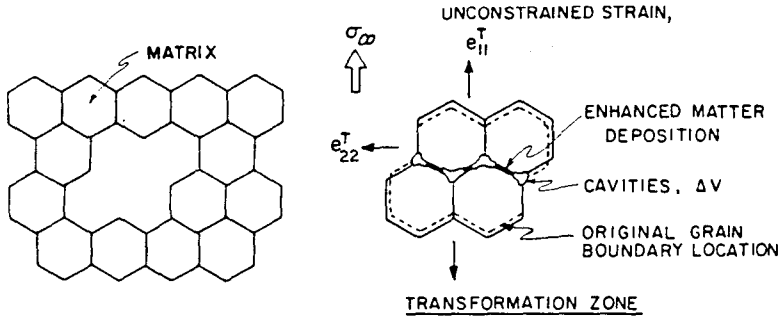

b) UNCONSTRAINED STRAIN

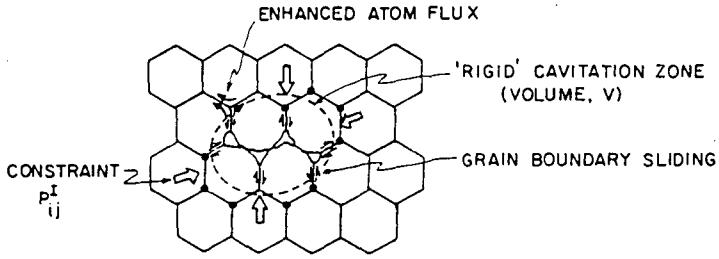

c) CONSTRAINED STRAIN

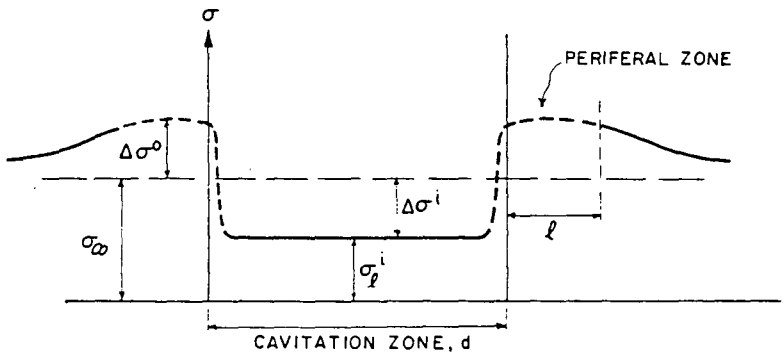

d) STRESS DISTRIBUTION

XBL 813-5321

Fig. I-3

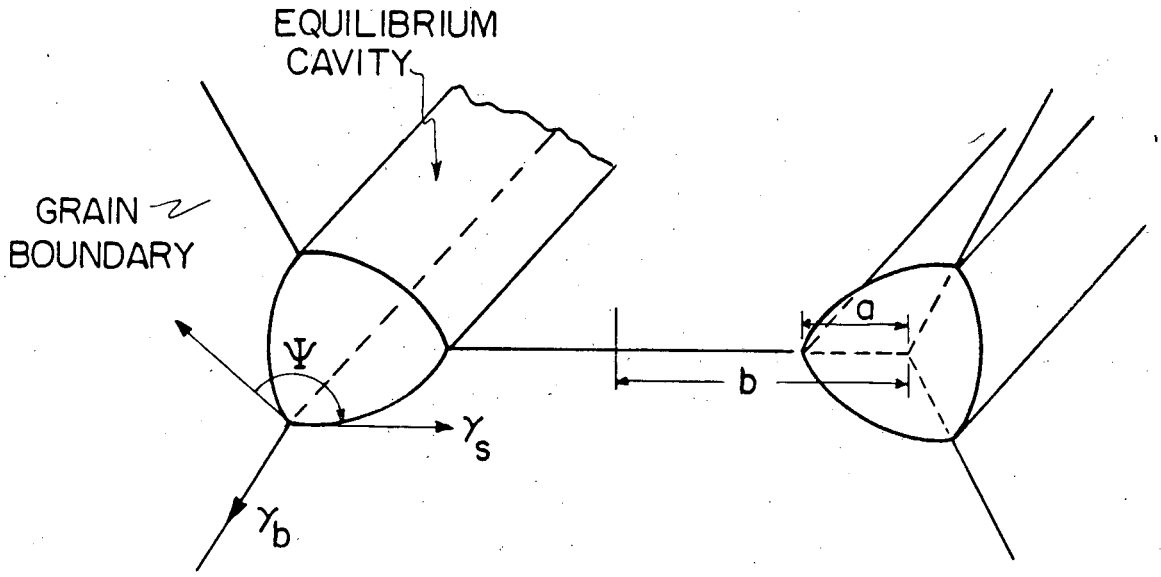

a) EQUILIBRIUM CAVITIES

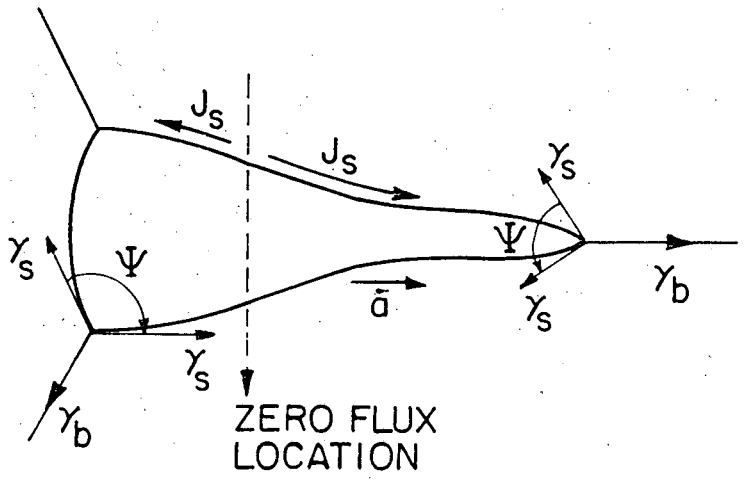

b) CRACK-LIKE CAVITY

XBL8010-6151

Fig. I-4

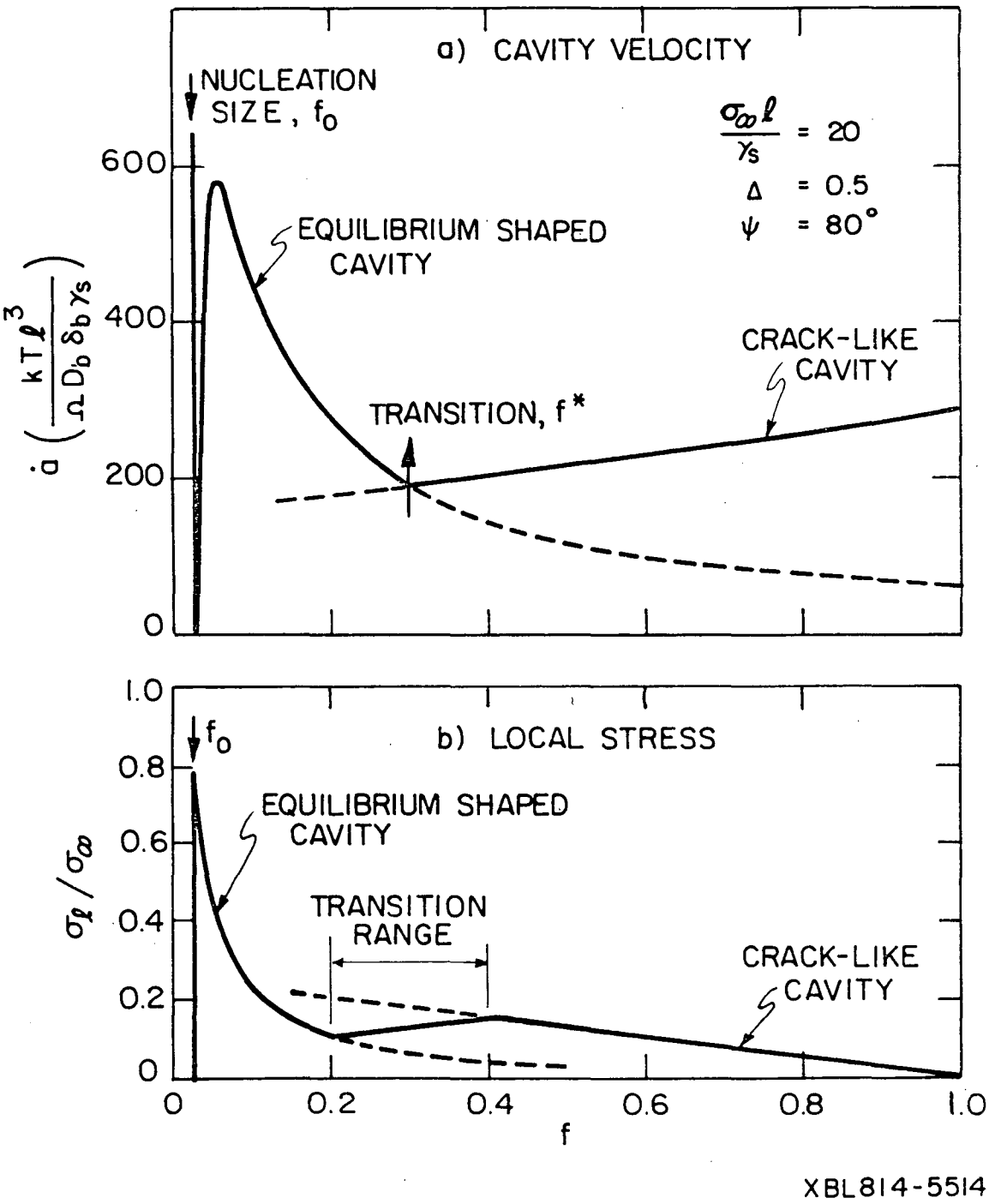
a) CAVITY VELOCITY
NUCLEATION SIZE, f_o
$\frac{\sigma_\infty \ell}{\gamma_s}$ = 20
Δ = 0.5
ψ = 80°
EQUILIBRIUM SHAPED CAVITY
CRACK-LIKE CAVITY
TRANSITION, f*
$\dot{a}\left(\frac{kT\ell^3}{\Omega D_b \delta_b \gamma_s}\right)$
600
400
200
0
b) LOCAL STRESS
f_o
EQUILIBRIUM SHAPED CAVITY
TRANSITION RANGE
CRACK-LIKE CAVITY
$\sigma_\ell / \sigma_\infty$
1.0
0.8
0.6
0.4
0.2
0
0
0.2
0.4
0.6
0.8
1.0
f
XBL814-5514

Fig. I-5

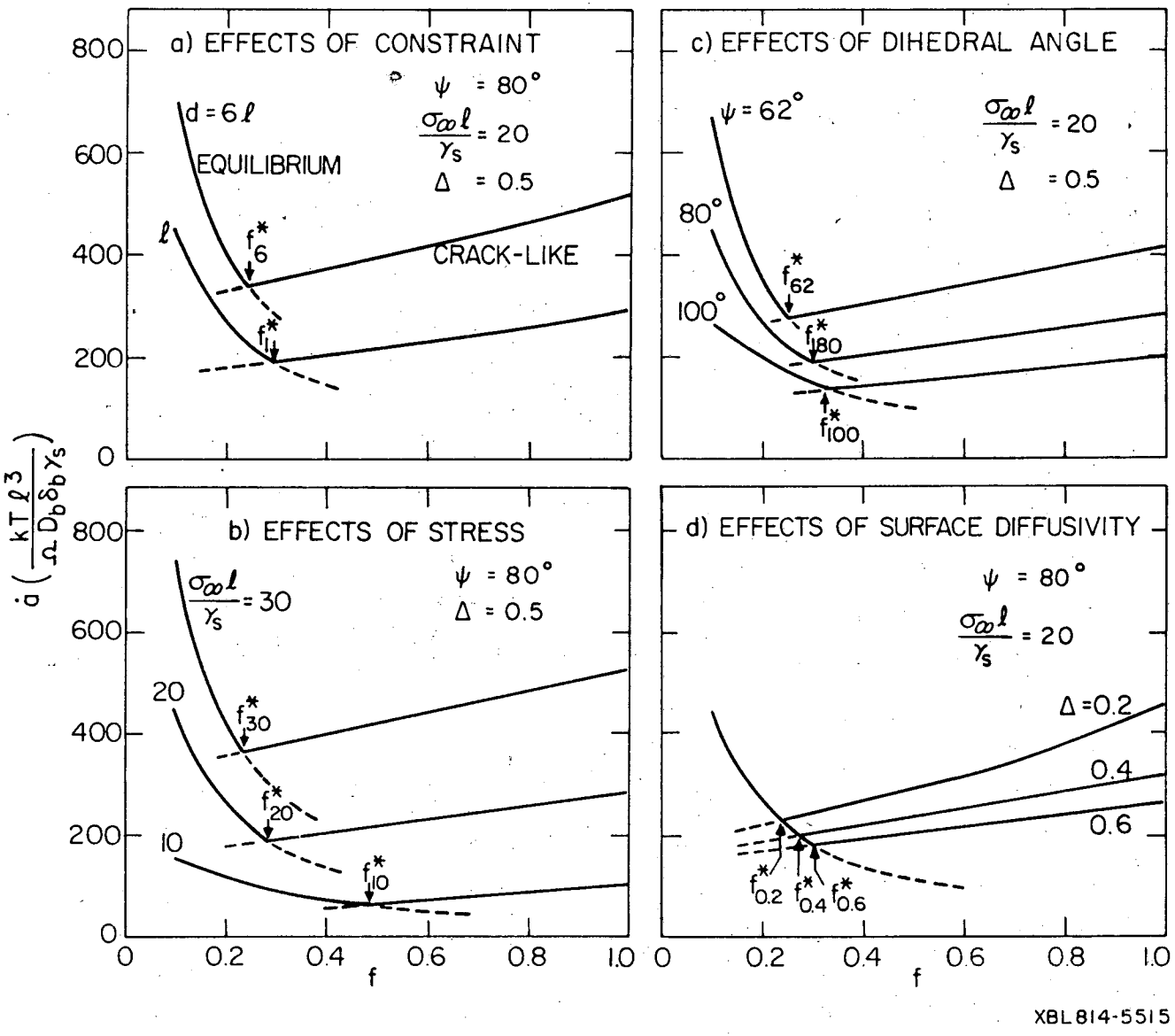
a) EFFECTS OF CONSTRAINT
ψ = 80°
σ∞ℓ/γs = 20
Δ = 0.5
d = 6ℓ
EQUILIBRIUM
ℓ
CRACK-LIKE
f*6
f*1
c) EFFECTS OF DIHEDRAL ANGLE
ψ = 62°
80°
100°
σ∞ℓ/γs = 20
Δ = 0.5
f*62
f*80
f*100
b) EFFECTS OF STRESS
σ∞ℓ/γs = 30
20
10
ψ = 80°
Δ = 0.5
f*30
f*20
f*10
d) EFFECTS OF SURFACE DIFFUSIVITY
ψ = 80°
σ∞ℓ/γs = 20
Δ =0.2
0.4
0.6
f*0.2
f*0.4
f*0.6
ḋ (kTℓ³/Ω Db δb γs)
f
0
200
400
600
800
0.2
0.4
0.6
0.8
1.0
XBL814-5515

Fig. I-6

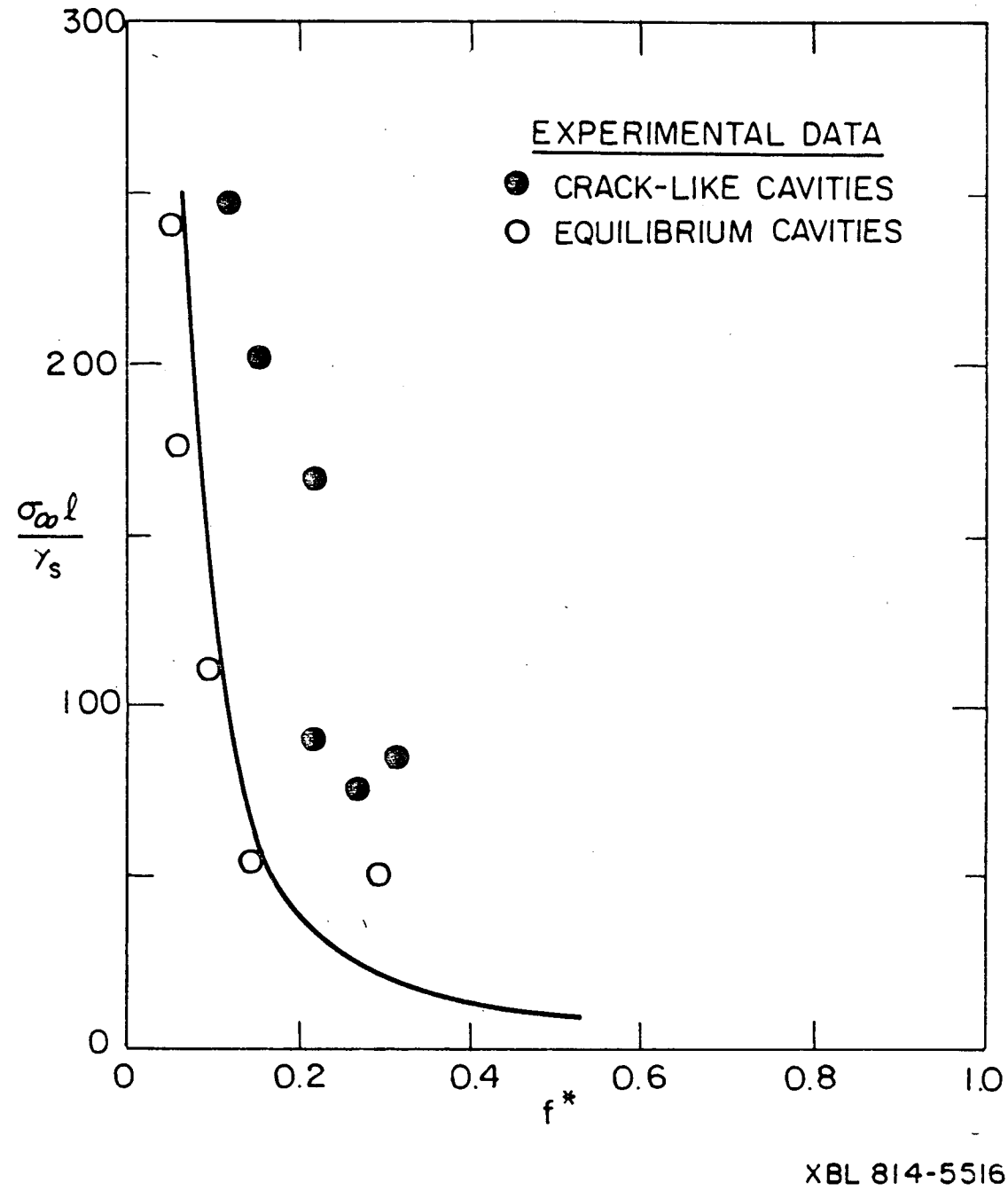
300
200
100
0
$\frac{\sigma_\infty \ell}{\gamma_s}$
EXPERIMENTAL DATA
CRACK-LIKE CAVITIES
EQUILIBRIUM CAVITIES
0
0.2
0.4
0.6
0.8
1.0
f*
XBL 814-5516

Fig. I-7

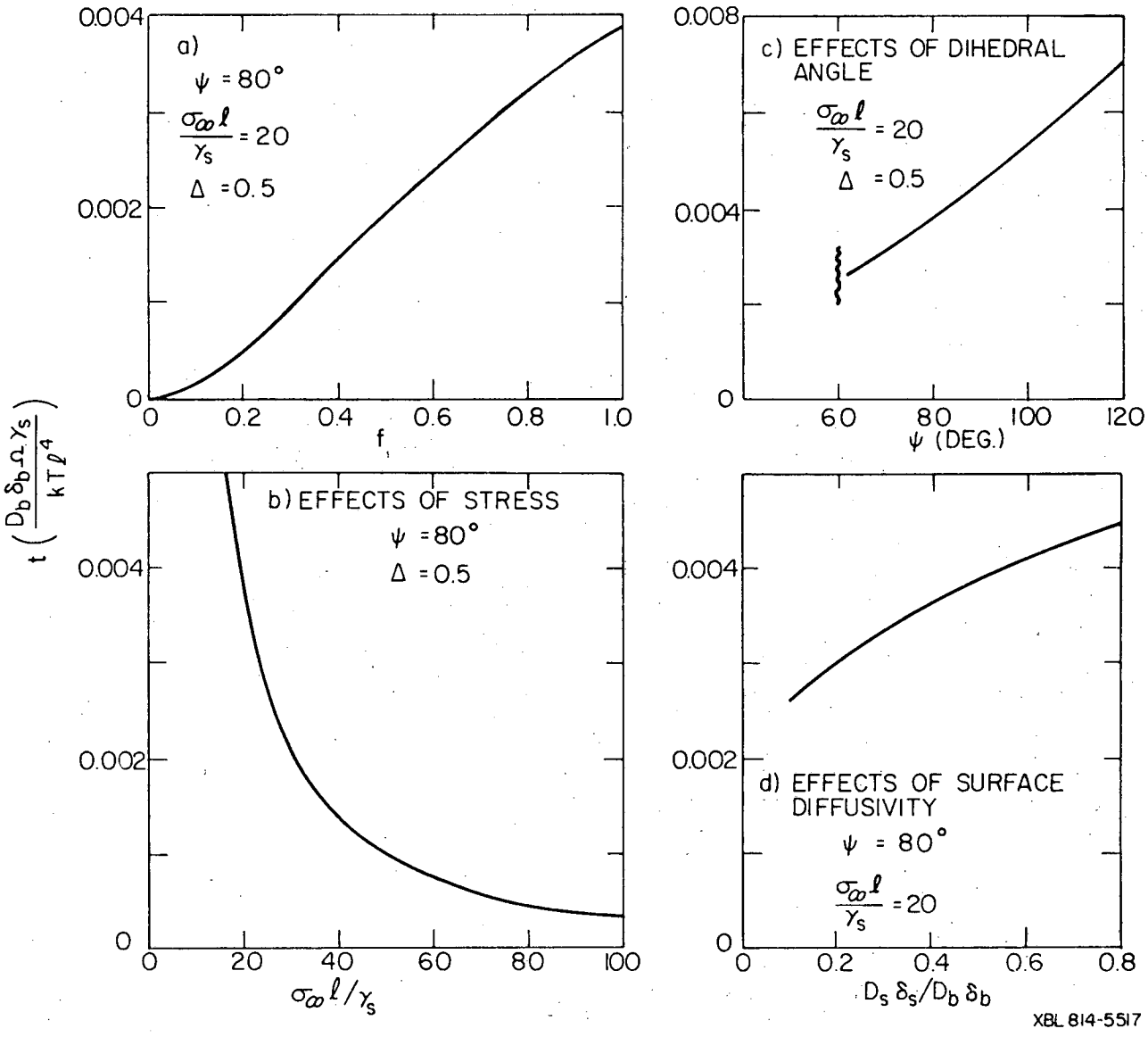
a)
ψ = 80°
σ∞ℓ/γs = 20
Δ = 0.5
f
c) EFFECTS OF DIHEDRAL ANGLE
σ∞ℓ/γs = 20
Δ = 0.5
ψ (DEG.)
b) EFFECTS OF STRESS
ψ = 80°
Δ = 0.5
σ∞ℓ/γs
d) EFFECTS OF SURFACE DIFFUSIVITY
ψ = 80°
σ∞ℓ/γs = 20
Ds δs/Db δb
t(Db δb Ω γs / kT ℓ⁴)
XBL 814-5517

Fig. I-8

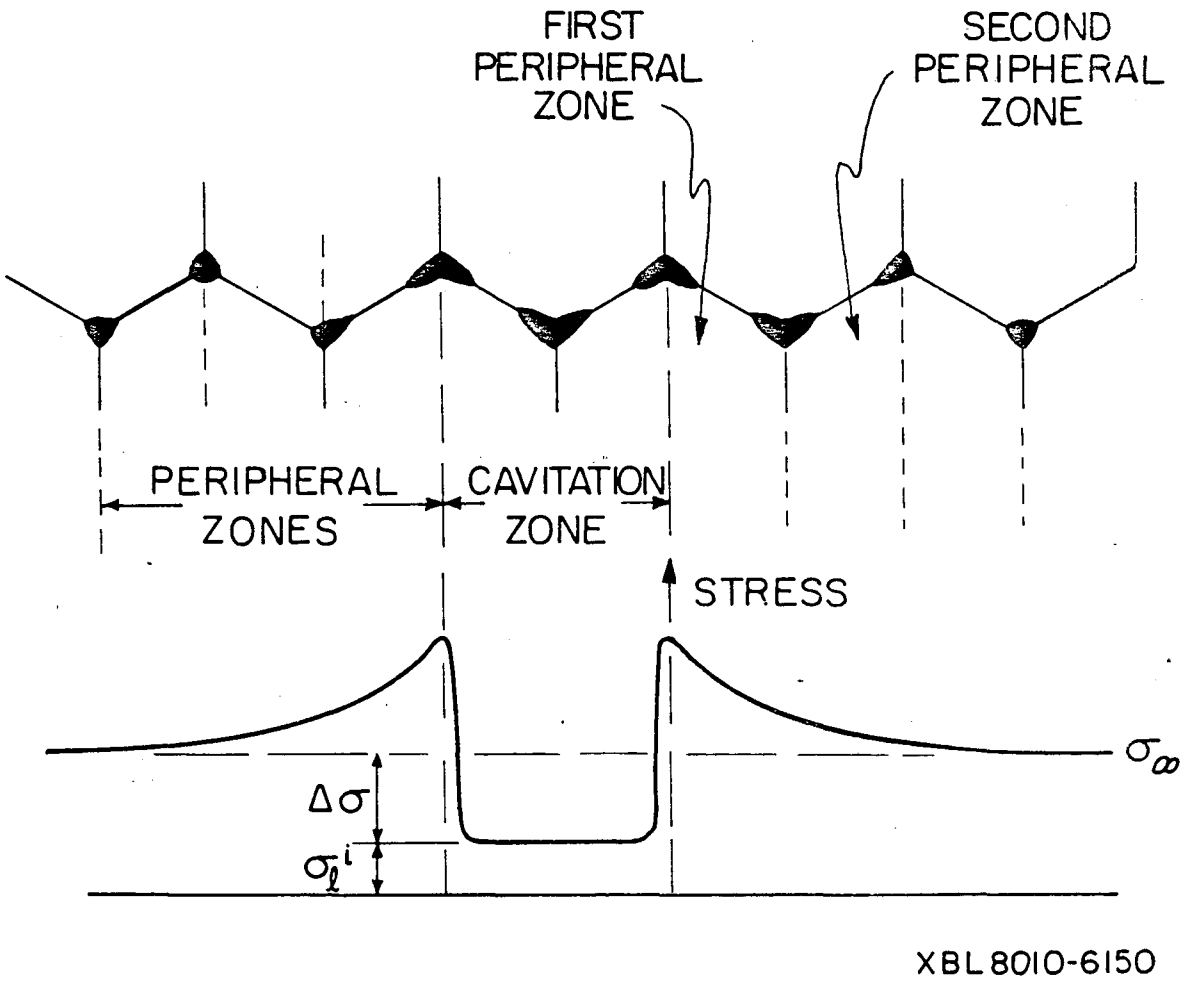
FIRST
PERIPHERAL
ZONE
SECOND
PERIPHERAL
ZONE
PERIPHERAL
ZONES
CAVITATION
ZONE
STRESS
σ_∞
$\Delta\sigma$
σ_ℓ^i
XBL8010-6150

Fig. I-9

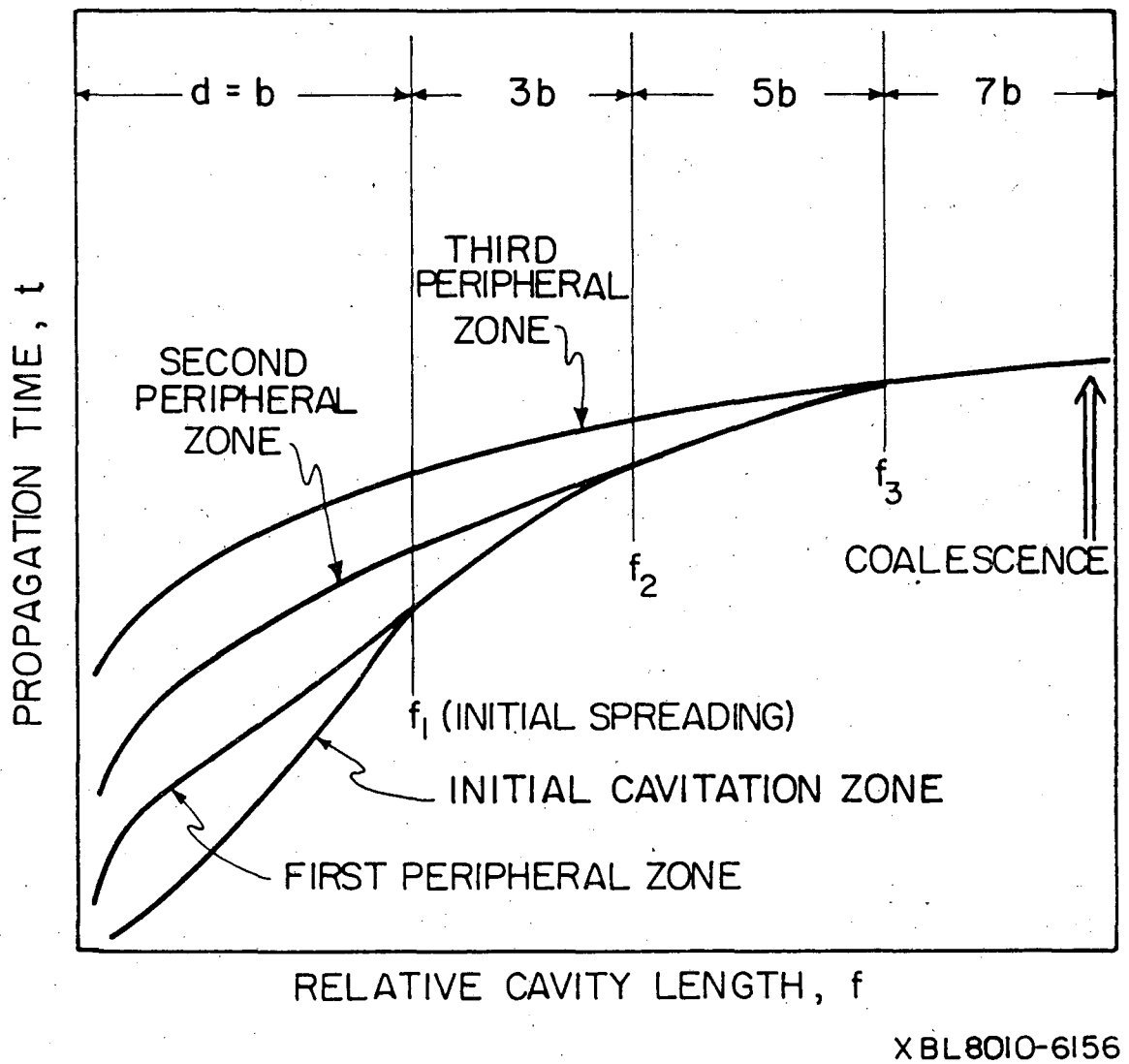
d = b
3b
5b
7b
THIRD PERIPHERAL ZONE
SECOND PERIPHERAL ZONE
f_3
f_2
COALESCENCE
f_1 (INITIAL SPREADING)
INITIAL CAVITATION ZONE
FIRST PERIPHERAL ZONE
PROPAGATION TIME, t
RELATIVE CAVITY LENGTH, f
XBL8010-6156

Fig. I-10

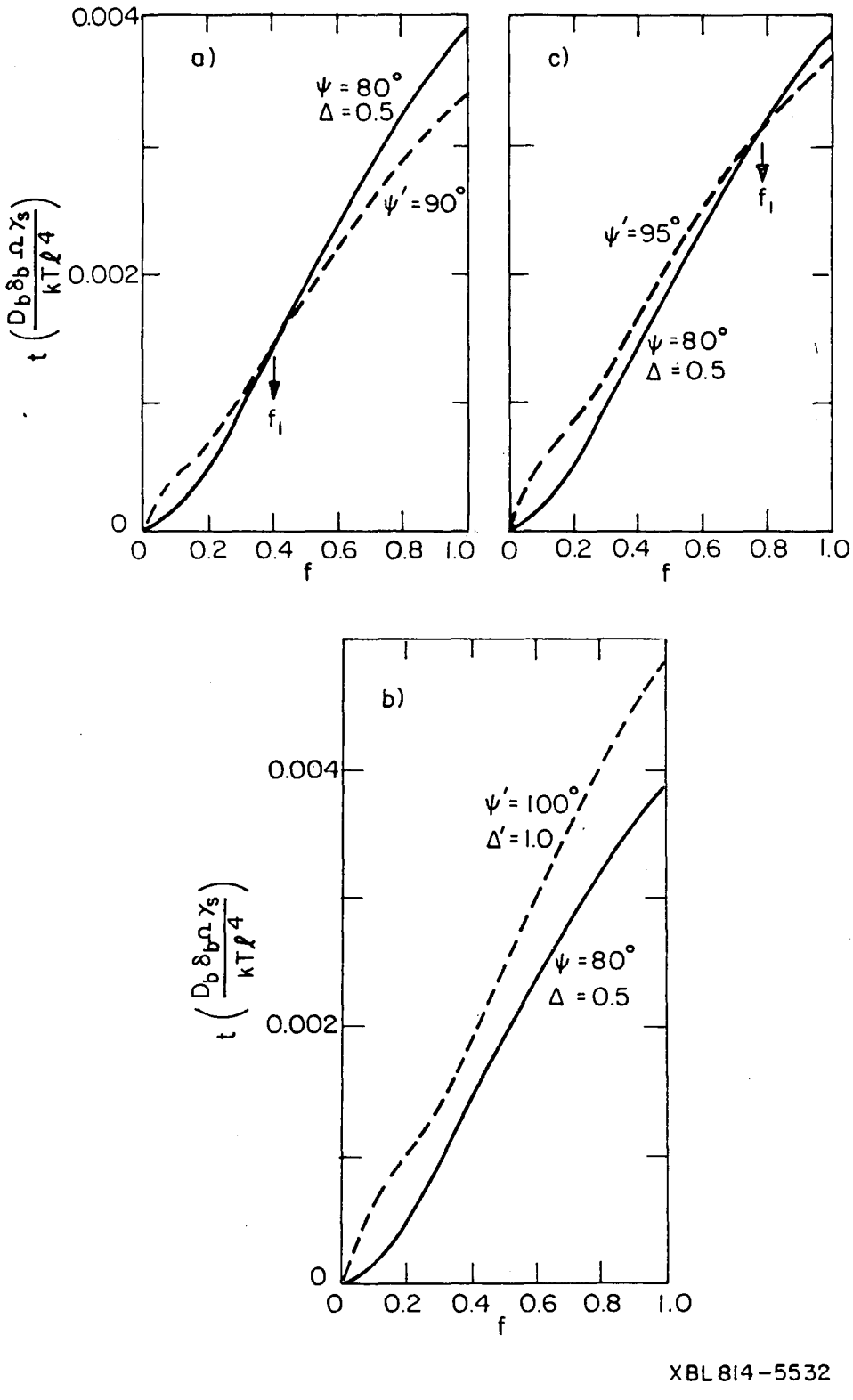
a)
ψ = 80°
Δ = 0.5
ψ' = 90°
f1
c)
ψ' = 95°
ψ = 80°
Δ = 0.5
f1
b)
ψ' = 100°
Δ' = 1.0
ψ = 80°
Δ = 0.5
0.004
0.002
0
0.2
0.4
0.6
0.8
1.0
f
t (Db δb Ω γs / kT ℓ4)
XBL 814-5532

Fig. I-11

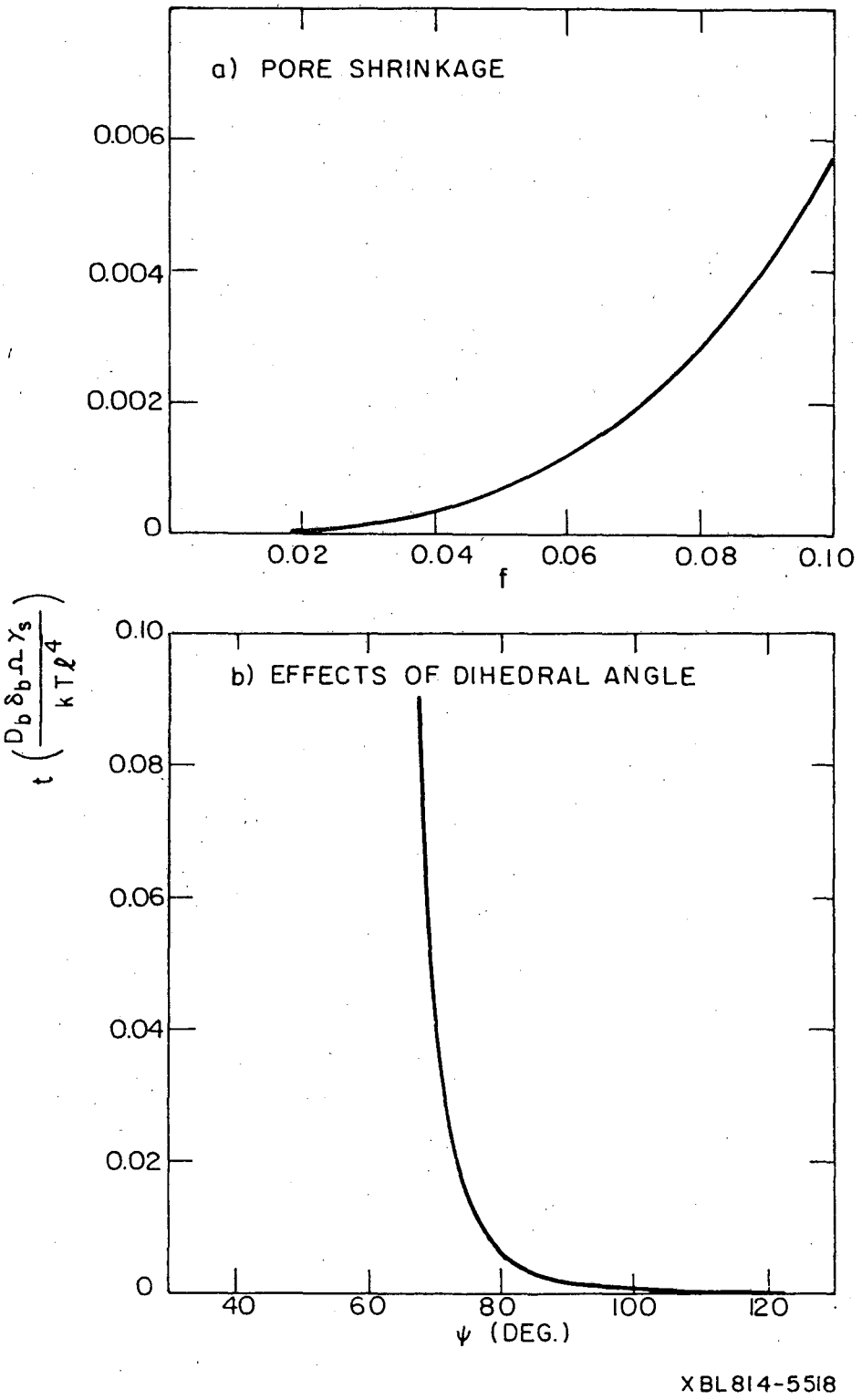
a) PORE SHRINKAGE
0.006
0.004
0.002
0
0.02
0.04
0.06
0.08
0.10
f
b) EFFECTS OF DIHEDRAL ANGLE
$t\left(\frac{D_b \delta_b \Omega \gamma_s}{kT\ell^4}\right)$
0.10
0.08
0.06
0.04
0.02
0
40
60
80
100
120
ψ (DEG.)
XBL814-5518

Fig. I-12

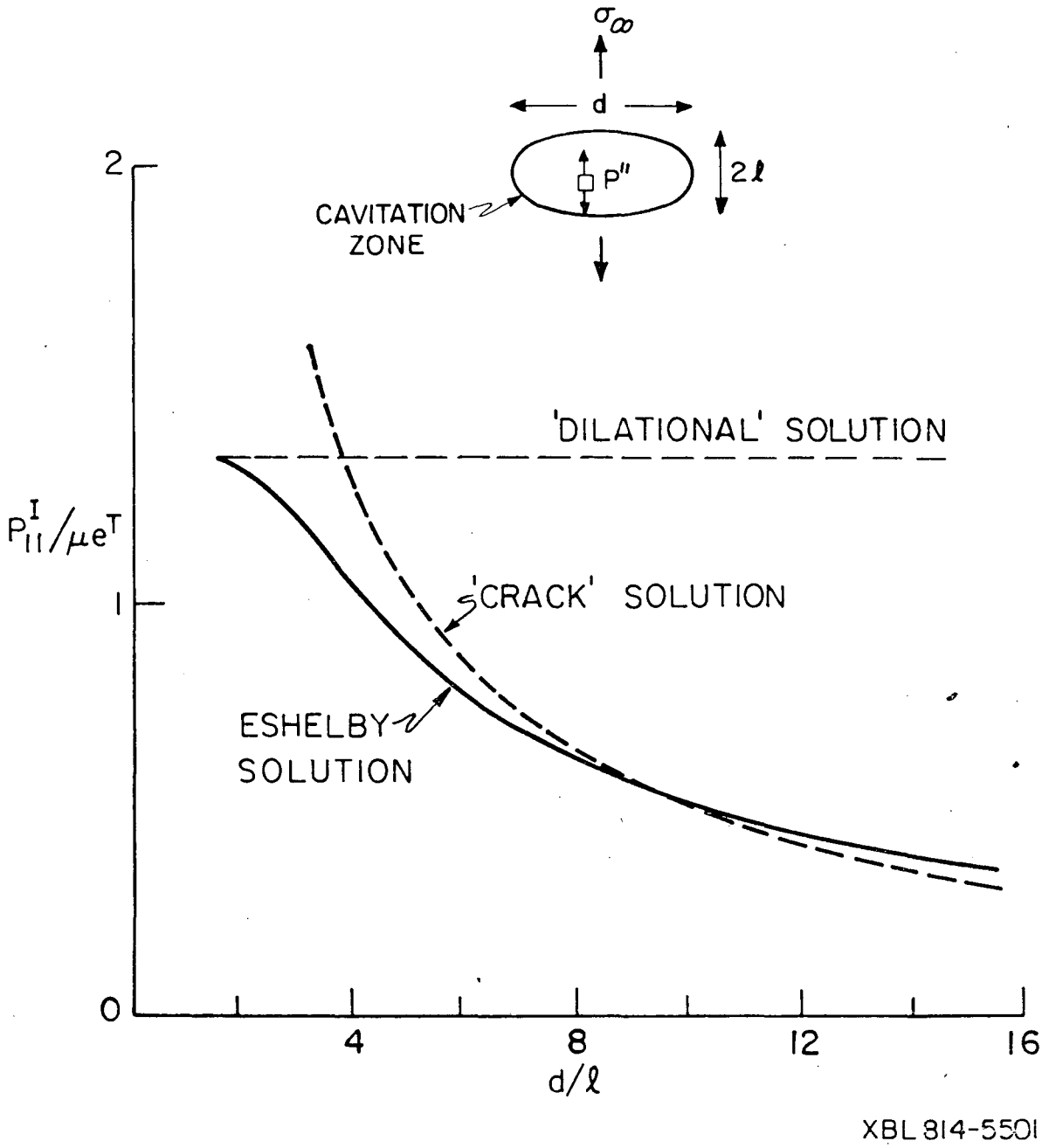
σ_∞
d
P''
2ℓ
CAVITATION ZONE
'DILATIONAL' SOLUTION
'CRACK' SOLUTION
ESHELBY SOLUTION
$P^I_{11}/\mu e^T$
2
1
0
4
8
12
16
d/ℓ
XBL 814-5501

Fig. I-13

PART II

PORE/GRAIN BOUNDARY SEPARATION

1. INTRODUCTION

The separation of pores from grain boundaries during final stage sintering is a preeminent barrier to the complete densification of a powder compact. Pores attached to grain boundaries shrink by a grain boundary diffusion process; but once a pore is detached, and locates within the grain, it can only shrink by the (usually) much slower mechanism of lattice diffusion. Consequently, observations indicate that once trapped inside a grain, the pore does not exhibit significant shrinkage.[1,2] Additionally, the separation process may be an important element in the initiation of exaggerated grain growth.[3-5]

To forestall separation, many researchers have focused on process variables, such as additives,[6-8] atmosphere,[9,10] particle size,[11] and size distribution.[12] For example, small particles and a narrow size distribution generally yield high densities; also, certain impurities may (a) decrease the grain boundary mobility or increase the surface (pore) mobility to encourage pore attachment for most of the sintering process, (b) inhibit boundary migration by a solute drag mechanism.[13,14] However, the observations are mostly empirical and do not readily extend to new materials. Each time, a unique process must be developed, most often by trial and error.

Recent literature[3,4,15-17] has focused on a phenomenological approach to explain the effects of the process variables, by introducing simplified concepts of the physical interaction between the pore and grain boundary during breakaway. The final result of the analysis can be expressed in terms of a separation diagram in pore, grain size

space, as illustrated in Fig. 1. The present analysis emphasizes the physical mechanism involved in the separation process and thereby, identifies several quantitative differences from the phenomenological analysis.

The phenomenological analysis is essentially based upon solutions for the interaction of a boundary with a rigid second-phase particle. Specifically, the interaction between a pore and a moving grain boundary assumes a spherical pore, moving through an isotropic, homogeneous material at some velocity determined by the surface diffusion coefficient. A unique pore mobility has thereby been derived by retaining the spherical symmetry of the pore (hence, neglecting the changes in pore shape needed to maintain the atom flux over the pore surface). The approximate pore mobility deduced in this manner is given by;[18]

$$M_p = \frac{D_s \delta_s \Omega}{kT\pi a_o^4} \tag{1}$$

where $D_s \delta_s$ is the surface diffusion parameter, a_o is the pore radius, Ω is the atomic volume, and kT has the usual meaning.

The force, F, exerted by the grain boundary on the pore (which eventually dictates separation) is also derived from the rigid particle (spherical pore) analog by assuming that the contact line between the boundary and the pore can move freely over the pore surface; whereupon the force becomes;

$$F = 2\pi a_o \gamma_b \cos\theta \sin\theta \tag{2}$$

where θ is the boundary intersection angle and γ_b is the grain boundary

energy. The force has a maximum value $\hat{F}$ at $\theta = \pi/4$ given by;

$$\hat{F} = \pi a_o \gamma_b \tag{3}$$

This force maximum, coupled with the pore mobility (Eq. (1)) yields a peak pore velocity;

$$\hat{v}_p = \frac{\Omega D_s \delta_s \gamma_b}{kT a_o^3} \tag{4}$$

In mechanically undeformed materials the driving force for grain boundary migration stems only from the energy of the grain boundary. This driving force can be thought of as a pressure difference between the two touching grains, caused by the curvature of their interface.[19] Breakaway is considered to occur when the grain boundary velocity exceeds the peak pore velocity in Eq. (4). However, a determination of the separation condition requires that some assumptions be made concerning the velocity of pores attached to grain boundaries. This is achieved by requiring that the motion of each grain boundary be impeded by the presence of pores, such that the grains and pores are treated as average entities. Specifically, the grain boundaries are considered to contain N pores per atom and the spacing between pores is assumed to be proportional to the average grain size.[4,15] With these assumptions, the separation condition can be expressed as

$$\dot{R} = 2 \left(\frac{\pi a_o}{R^2} + \frac{D_s \delta_s \Omega^{1/3}}{M_b a_o^3 kT} \right)^{-1} \tag{5}$$

where R is the grain radius and M_b is the grain boundary mobility. The two limiting cases

$$R \leqslant \frac{2M_b kTa_o^3}{D_s \delta_s \Omega^{1/3}} \tag{6a}$$

and

$$R \geqslant \frac{\pi a_o}{2} \tag{6b}$$

provide the boundaries of the separation diagram depicted in Fig. 1.

The significance of this diagram for the development of fully dense materials can be appreciated by imposing a typical grain, pore size trajectory.[20] When this trajectory avoids the separation region, breakaway is prohibited and the attainment of full density is not impeded by pore isolation within the grains.

The quantitative application of this separation diagram to the avoidance of breakaway is suspect, because none of the physical details of pore motion and breakaway have been considered in the analysis; besides, neither the theoretical nor the experimental basis for choosing the spherical pore has been established. The present model intends to address this deficiency by providing a self-consistent physical description of attached pore motion. This is achieved by first determining the shape changes that accompany the motion of a pore attached to a grain boundary. Then, the shapes of grain boundaries attached to pores subject to grain growth are deduced. The grain boundry shapes are determined within the context of the grain disappearance process

that actually accompanies grain growth. Finally, expressions for the pore and grain sizes that characterize the separation event are derived and implications for the avoidance of breakaway are discussed.

2. PORE VELOCITIES

The complete separation of pores from grain boundaries occurs when the pores are located on two-grain interfaces (Fig. 2). The separation of pores from three-grain junctions onto two-grain interfaces must precede this complete separation event. However, this process is complex and is assumed to occur more readily than the ultimate separation. The present analysis is thus devoted to a determination of the pore separation criticality at two grain interfaces. The motion of pores attached to three grain junctions has been considered by Spears.[20]

The motion of pores with grain boundaries is achieved by inducing a flux of atoms from the leading to the trailing surface of the pore (Fig. 3). The driving force for the atom flux is associated with the existence of a gradient in the curvature of the pore surface. Pore distortion is thus a necessary consequence of pore motion. This section is primarily concerned with a determination of the pore distortion as a function of pore velocity. However, a corollary of pore distortion is a change in the location and inclination of the grain boundary tangent at the pore, grain boundary intersection (Fig. 3). This boundary tangent change is uniquely related to the pore distortion and thereby, provides the important link with breakaway.

The configuration selected for analysis is an axisymmetric pore[21] subject to motion by surface diffusion.[22,23†] Initially, steady-state motion (all locations on the surface moving at the same velocity)

---

†Surface diffusion is likely to be the dominant mode of pore motion in many practical situations, but equivalent analysis for evaporation/condensation and lattice diffusion will eventually be needed.

is considered, followed by some considerations pertinent to non-steady-state behavior. The axisymmetric pore exhibits two curvatures (see Fig. 11): an in-plane curvature, κ_1, and an axisymmetric curvature, κ_2. These curvatures are related to the coordinates of the problem (x,y) by;

$$\kappa_1 = (d^2y/dx^2)[1 + (dy/dx)^2]^{-3/2}$$
$$\kappa_2 = (1/x)(dy/dx)\ [1 + (dy/dx)^2]^{-1/2} \tag{7}$$

The chemical potential associated with the curvature is

$$\mu = \Omega\gamma_s(\kappa_1 + \kappa_2) \tag{8}$$

where γ_s is the surface energy. A varying curvature along the pore surface gives the gradient of chemical potential, which in turn, gives the driving force for surface diffusion, and the flux equation has the form

$$J_s = -\left(\frac{D_s\delta_s\gamma_s}{kT}\right)\frac{d(\kappa_1 + \kappa_2)}{ds} \tag{9}$$

where J_s is the number of atoms per unit time crossing unit length of the surface, and ds is an element of pore surface in the flow direction (Fig. 3). Letting the angle between the surface tangent and x-axis be denoted by α as shown in Fig. 3 $ds = dx/\cos\alpha$; thus Eq. (9) can be expressed

$$J_s = -\left(\frac{D_s\delta_s\gamma_s}{kT}\right)\frac{d(\kappa_1 + \kappa_2)}{dx}\cos\alpha \tag{10}$$

Symmetry permits consideration of one quadrant of the pore. For a pore moving with a velocity v_p (positive) in the Y direction (Fig. 3b), conservation of matter requires that

$$2\pi x\, J_s = \pm\, \pi x^2 v_p/\Omega \tag{11}$$

where the positive sign refers to the leading surface and the negative sign to the trailing surface.

Using the symbols, p and q ($\equiv dy/dx$) for the slopes of the trailing and leading surfaces respectively, Eqs. (7), (10) and (11) give;

$$p''\,(1+p^2) - 3pp'^2 + (1/x)p'(1+p^2)^2 - (1/x)p^2p'(1+p^2) - (1/x^2)p(1+p^2)^2 = \frac{v_p kT}{2\Omega D_s \delta_s \gamma_s}\, x\, (1+p^2)^3 \tag{12a}$$

and

$$q''\,(1+q^2) - 3qq'^2 + (1/x)q'(1+q^2)^2 - (1/x)q^2q'(1+q^2) - (1/x^2)q(1+q^2)^2 = -\frac{v_p kT}{2\Omega D_s \delta_s \gamma_s}\, x\, (1+q^2)^3 \tag{12b}$$

The motion of the pore is subject to the requirement that the total dihedral angle Ψ between the grain boundary and pore surfaces (Fig. 3) be invariant. Hence, in terms of the constituent dihedral angles $\Psi_1(v_p)$, and $\Psi_2(v_p)$;

$$\Psi_1(v_p) + \Psi_2(v_p) = \Psi \tag{13a}$$

which can be conveniently re-expressed for further analysis in the form

$$p + q = c - cpq \tag{13b}$$

at the pore tip, where $c = \tan\Psi$. It is also required that the chemical potential be continuous at the intersection of the leading and trailing surfaces; hence,

$$p' (1+p^2)^{-3/2} + (p/x)(1+p^2)^{-1/2} = q' (1+q^2)^{-3/2} + (q/x)(1+q^2)^{-1/2} \tag{14}$$

at the pore tip. Finally, it is noted that the atom flux and surface slope must be zero at the axis of symmetry.

The solution of Eq. (12) subject to the above boundary conditions is a non-linear problem. A solution is thus obtained by linearizing about a trial solution and then using a finite difference scheme, in which the region is divided into N+1 points with uniform spacing Δx (Fig. 3b). The resultant linearized equations (Appendix I) are in the form of coupled, tridiagonal matrices which can be solved by iteration. The iteration procedure commences with the slope solution for a stationary pore (with a uniform surface curvature) as the trial solution and procedes to solve for the slope of a moving pore for a series of successive small increments in pore velocity. Convergence is assured by a proper linearization and suitably small increments in pore velocity. The pore shape can be determined from the slope (Appendix II). Some resultant pore shapes, computed in accord with this procedure, expressed in terms of the dimensionless pore velocity,

$$\nu_p = \frac{v_p kT a_o^3}{\Omega D_s \delta_s \gamma_s} \tag{15}$$

are plotted in Fig. 4 for $\Psi = \pi/3$, where a_o is the radius of contact between the boundary and the stationary pore. Shapes similar to these predictions have been observed experimentally (Fig. 5).[21]

The grain boundary bisects the dihedral angle Ψ and satisfies the relation (for a non-equilibrium case, a correction factor may be needed)

$$\theta = (\Psi_1 - \Psi_2)/2 \tag{16}$$

The inclination θ of the grain boundary tangent to the plane of contact between the grain boundary and the pore (Fig. 3) emerges from the analysis as a unique function of the normalized pore velocity ν_p, and dihedral angle as plotted in Fig. 6a. The radius of contact, a, between the boundary and pore can also be deduced by requiring that the pore volume be independent of pore velocity, in order to permit a unique comparison between the dimensions of the stationary and moving pores. The resultant trend in contact radius with normalized pore velocity is plotted in Fig. 6b, indicating a slow decrease in contact radius, a, with increase in pore velocity.

Convergent pore shape solutions are found to exist over a limited range of pore velocities, as inferred by the terminations in Fig. 6. A steady-state velocity maximum, $\hat{v}_p(\Psi)$, is thus implied.† This maximum

†Attempts at obtaining pore shapes in excess of the maximum always result in divergent solutions.

exhibits an appreciable dependence on the dihedral angle, as plotted in Figs. 7a and 7b, where the dimensionless pore velocity is normalized by the stationary pore radius in Fig. 7a and by the current moving pore radius in Fig. 7b. The pore shapes that develop at the maximum are constructed for several different dihedral angles in Fig. 8. The existence of a velocity maximum is associated with an inability to simultaneously satisfy the requirements that the dihedral angle be specified, that the curvature be continuous and finite and that the pore velocity be uniform. Specifically, attempts to increase the velocity above $\hat{v}_p(\Psi)$ must violate one of these imposed conditions. The consequences of increasing the velocity above v_p can be readily visualized when the dihedral angle $\Psi \approx \pi$ (Fig. 9). Shape changes which induce a continuous atom flux in the requisite direction for pore motion (i.e., a continuous gradient in surface curvature) cannot be constructed. Regions subject to a counter-flux are inevitable (Fig. 9). Steady-state motion by surface diffusion of a pore with $\Psi \sim \pi$ is thus impossible (in marked contrast with the expectations of the phenomenological analysis).[4,15†] This steady-state velocity maximum may be regarded as the present equivalent of the peak velocity derived using the phenomenological analysis (Eq. (4)), and can be expressed as

---

† The inability of a pore with $\Psi \sim \pi$ to exhibit steady-state motion implies that such pores will always detach from grain boundaries. This is intuitively reasonable because, when $\Psi = \pi$, the grain boundary energy is zero and there is no preference for pores to locate on grain boundaries.

$$\hat{v}_p \approx \frac{\Omega D_s \delta_s \gamma_s}{kTa_o^3} (17.9 - 6.2\Psi) \quad (17a)$$

or

$$\hat{v}_p \approx \frac{\Omega D_s \delta_s \gamma_s}{kTa_o^3} (10.8 - 3.44\Psi) \quad (17b)$$

The consequences of a maximum in the steady-state pore velocity are central to the breakaway problem. Non-steady-solutions, in which the velocity varies over the pore surface (with a maximum at the axis of the leading surface) can be found for net velocities in excess of $\hat{v}_p$. These solutions coincide with a marked change in pore shape and an appreciable decrease in the grain boundary contact radius, a, as illustrated by the shape depicted in Fig. 10. It is presumed, therefore, that the contact radius, a, will rapidly diminish to zero when the net velocity exceeds $\hat{v}_p$, causing the grain boundary to converge onto the pore axis and thereby, to initiate breakaway. Hence, the upper bound steady-state pore velocity will hereafter be used as a velocity which, if exceeded, will inevitably result in non-steady-state pore motion and breakaway.

Finally, it is instructive to note that the pore mobility defined in terms of the pore velocity and the force exerted by the grain boundary ($F_p = 2\pi a\gamma_b \sin\theta$) is not unique; but changes as the pore velocity changes. Analyses that utilize a unique pore mobility are thus subject to uncertainty.

3. GRAIN BOUNDARY SHAPES

The evolution of grain boundary shapes within the vicinity of a dragging pore constitute an important physical link with the breakaway process (even though a knowledge of grain boundary shapes is not explicitly required in order to estimate the breakaway condition). Pore drag will initiate when the velocity of the pore becomes smaller than the grain boundary velocity at some remote location on the boundary (Fig. 11). The incidence of pore drag yields a grain boundary with two dominant curvatures (Fig. 11): the in-plane radius of curvature R_1 and the axisymmetric radius of curvature R_2. The driving force F_b for grain boundary motion is thus;

$$\begin{aligned} F_b &= \gamma_b \Omega^{2/3} \left[1/R_1 + 1/R_2\right] \\ &\equiv \gamma_b \Omega^{2/3} \Big[-(d^2y/dx^2) \left[1+(dy/dx)^2\right]^{-3/2} \\ &\quad + (1/y)\left[1 + (dy/dx)^2\right]^{-1/2} \Big] \end{aligned} \tag{18}$$

where (x,y) are the grain boundary coordinates (Fig. 11). For the dragging pore, R_1 is negative. However, a driving force with a component acting in the direction of the pore velocity still exists whenever $R_2 < |R_1|$; a situation which must prevail during pore drag. The existence of the axisymmetric curvature accounts for the observed motion of pores away from their in-plane center of curvature, Fig. 5 (contrasting with the usual observation of boundary motion toward their in-plane center of curvature).

Grain boundary shapes can be determined from Eq. (18) if some assumption is made concerning the disposition of driving forces along

the boundary. Preliminary estimates of the shape of a grain boundary containing a pore, pertinent to a three-sided grain, are determined for the simplest possible postulate: that of uniform driving force (i.e., constant chemical potential). The governing differential equation is then;

$$dp/dx = - (2/R)(1+p^2)^{3/2} + (1/y)(1+p^2) \qquad (19)$$

where $p = dy/dx$ and R is the radius of curvature of the two boundaries devoid of pores. On a pore free grain boundary, the grain boundary inclination, θ_o, at the three-grain junction is $\pi/6$ (Fig. 12). However, pore drag increases the inclination. The shapes calculated from Eq. (19) using a finite difference scheme, subject to the condition that the angle at the three-grain junction be $2\pi/3$, are plotted in Fig. 12 for several different θ_o.

The grain boundary shapes within the vicinity of the pore are similar in form to those observed experimentally (Fig. 5), but deviate appreciably at more remote locations. The dragging pore thus has an influence zone (Fig. 11) which appears to be smaller than predicted by imposing a uniform chemical potential. Hence, further progress toward a detailed understanding of the observed grain boundary shapes requires that some insights be gained concerning the gradient of driving force along the grain boundary. However, these details are not essential to the development of a mechanistic description of breakaway.

The grain boundaries subject to pore drag exhibit a velocity component normal to the axis of symmetry (Fig. 12), indicative of a tendency toward instability. More specifically, when v_b exceeds v_p,

the axisymmetric radius of curvature R_2 decreases during the motion of the pore, grain boundary configuration (Fig. 13) especially within the immediate vicinity of the pore. The decrease in R_2 exceeds the change in R_1, and hence, the configuration is intrinsically metastable. Steady-state motion of the complete pore/grain boundary ensemble is impossible. Presumably, therefore, pore drag will increasingly distort the boundary, and eventually induce separation. The actual separation will occur when the pore velocity exceeds the steady-state maximum (section 2) and the pore contact radius, a, diminishes rapidly with further small increments in net pore velocity (thereby, permitting convergence of the boundary onto the pore axis).

4. PORE BREAKAWAY

The specific condition that dictates the separation of pores from grain boundaries depends upon the grain configuration to which the pore is attached. Two specific configurations, pertinent to the earliest separation events that occur during grain growth, are considered in this section:† a pore located on one boundary of a three-sided grain (Fig. 2b) (the configuration that invariably precedes grain disappearance), and a pore located on one boundary of a five-sided grain at the perimeter of a large grain (Fig. 2a) subject to exaggerated grain growth. Pore drag observations (Fig. 5) indicate that the pore perturbs grain boundary motion over a certain influence distance, z. It is appropriate, therefore, to examine the motion of the grain boundary outside this influence distance, relative to that of the pore. This approach is, of course, only appropriate when the influence distance is less than the grain radius.

The velocity of the grain boundary outside the influence zone, in the direction of pore motion (Fig. 11) is,

$$v_b = \sqrt{3}\gamma_b M_b \Omega^{2/3}/R \qquad (20)$$

---

†Other configurations, such as several pores on one grain boundary, will provide different separation conditions. However, these separation events usually occur after the first separations have been induced and are, probably, less critical. For example, a modified phenomenological analysis with a pore spacing α R gives the two limiting cases (Appendix III)

$$R \leqslant 2M_b kT\gamma_b a_o^3/D_s\delta_s\gamma_s\Omega^{1/3}(17.9 - 6.2\Psi)$$

$$R \geqslant \delta_s\gamma_s\Omega^{1/3}(17.9 - 6.2\Psi)/2\gamma_b a_o$$

where R is the grain boundary radius of curvature. By allowing this velocity to exceed the peak steady-state pore velocity (Eq. 17), separation should be inevitable, provided that a grain boundary displacement (i.e., grain dimension) sufficient to create boundary convergence at the dragging pore (section 3) is available. This criterion yields a pore size for separation given by;

$$a_o^2 \geq \left(\frac{R}{a_o}\right)\left(\frac{\Omega^{1/3} D_s \delta_s \gamma_s}{kTM_b \gamma_b}\right) \frac{(17.9 - 6.2\Psi)}{\sqrt{3}} \qquad (21)$$

For the five-sided grain, R remains essentially constant, yielding a separation boundary, depicted in Fig. 14, reminiscent of that predicted by the phenomenological theory (Fig. 1). However, the most stringent condition for breakaway exists when R attains its smallest value. This condition develops in the three-sided grain configuration, preceding grain disappearance (Fig. 2b). For this grain configuration, separation is averted if the pore converges onto the prospective three grain junction, $R \backsim 2a$, before Eq. (21) can be satisfied. The critical condition thus becomes

$$(a_o)_c^2 = (\Omega^{1/3} D_s \delta_s \gamma_s / kTM_b \gamma_b)(2/\sqrt{3})(17.9 - 6.2\Psi) \qquad (22)$$

as plotted in Fig. 14. This critical pore size represents a lower bound for pore separation at all reasonable values of a_o/R.

An alternate approach for assessing separation would be to regard the onset of pore drag as an inevitable precursor to separation. The onset of drag can be ascertained by firstly determining the velocity developed by pores attached to boundaries of cylindrical (or spherical)

profile (the steady-state grain boundary shape) and then allowing the pore velocity to become incrementally smaller than the boundary velocity. Attachment of a pore to a spherical boundary requires that the grain boundary tangent, θ, satisfy a geometric requirement, dependent upon the pore radius, a, given by;

$$\tan\theta = a / \sqrt{R^2 - a^2} \tag{23}$$

But θ dictates the pore velocity (section 2, Fig. 6a), and R establishes the boundary velocity (Eq. (20)). Hence, by requiring v_p to be incrementally smaller than v_b, the condition for initiating instability becomes;

$$a_o^2 \gtrsim \frac{16(\Omega^{1/3} D_s \delta_s \gamma_s / kTM_b \gamma_b)}{\sqrt{1 - (a_o/R)^2}} \tag{24}$$

Hence, an instability is most likely to initiate when R is at its largest value (because θ decreases as R increases). The five-sided grain is thus the configuration with the greater propensity for pore drag. The drag initiation requirement (for $R \gtrsim 3a_o$) is then;

$$(a_o)^2_{drag} \approx 16(\Omega^{1/3} D_s \delta_s \gamma_s / kTM_b \gamma_b) \tag{25}$$

as plotted on Fig. 14. It is noted that drag initiation occurs at pore sizes just in excess of the lower separation bound $(v_b > \hat{v}_p)^{\dagger}$ and hence, that Eq. (22) invariably represents the lower limit for pore separation.

---

†Pore separation events should thus initiate at disappearing three-sided grains, just after observing pore drag.

Finally, it is noted tht pores cannot exist at two grain interfaces unless they are smaller than a fraction f of the grain facet dimension. The magnitude of this fraction can be ascertained from certain geometric considerations pertinent to the transfer of pores from three grain junctions onto two grain interfaces. The sequence of pore morphological changes that accompany final stage sintering initiate with the pores as continuous channels along three grain junctions (Fig. 15). These channels must dissociate into isolated pores at three grain junctions (by means of Rayleigh instability associated with pore surface changes in the presence of surface diffusion).[24] The largest possible isolated pore dimension, 2h, that can develop in this manner (Fig. 15) is equal to the grain facet length ℓ. This pore must then detach from the three grain junction onto a two grain interface. Determination of the relative volumes of pores at three and two grain interfaces[25] indicates that for a specified volume, the grain boundary contact diameter $2a_o$, must be smaller than the contact length 2h. Specifically, by equating 2h to ℓ, the largest admissable dimension, a_{max}, of a pore located at a two grain interface becomes;

$$a_{max}/\ell \approx 0.5[(1.28\Psi - 1.42)/(1.27\Psi - 0.556)]^{1/3} \qquad (26)$$

This condition is plotted on Fig. 14, ($\ell \approx R$) in order to outline the inadmissable region. Again, some similarity with the phenomenological result emerges (Fig. 1); but now the physical origin (based upon inadmissibility is apparent.

5. IMPLICATIONS AND CONCLUSIONS

The analysis of pore motion indicates that the pore distortion that necessarily accompanies pore motion results in a maximum possible steady-state pore velocity, $\hat{v}_p$. The separation of pores from grain boundaries is intimately associated with this peak velocity. Ancilliary studies of grain boundary shapes during pore drag indicate that the grain boundary is metastable during pore drag and hence, that the boundary can converge onto the axis of symmetry, causing breakaway, whenever the remote grain boundary velocity v_b exceeds $\hat{v}_p$.

The actual pore separation process based upon the requirement that $v_b > \hat{v}_p$ depends upon the grain configuration. The grain geometry that provides the lower bound for separation is the three-sided grain associated with grain disappearance during grain growth. This configuration yields a critical pore size for the onset of separation. This critical size increases as the surface diffusivity increases or as the grain boundary mobility and dihedral angle decrease. For other grain configurations, separation occurs at large values of pore size. However, since grain disappearance is an integral part of grain growth, these other separation conditions are considered less significant. The separation processes at the lower bound pore size occurs while the grain boundary exhibits uniform (spherical) curvature. Pore drag configurations would not, therefore, be observed at the lower bound. An ability to observe pore drag (Fig. 5) requires the development of microstructures well within the separation region (Fig. 14).

The material modifications that suppress breakaway may be ascertained by comparing the critical pore size with the pore, grain size

trajectory associated with final stage sintering. This issue is more comprehensively addressed by Spears.[20]

APPENDIX I

Linearization of Differential Equations Governing Pore Shape

A determination of the pore shape based on Eqs. (12), (13) and (14) requires a linearization procedure. This is achieved by commencing with a trial solution which approximates the final shape, such that $p(j)$, $p'(j)$ and $p''(j)$ can be replaced by initial trial values $p_o(j)$, $p_o'(j)$ and $p_o''(j)$. Similar substitutions can be made for q and its derivatives. Then we can write, for example,

$$p(j)p'(j) = [p_o(j)+\Delta p(j)][p_o'(j)+\Delta p'(j)]$$

$$\approx p_o(j)p_o'(j)+p_o'(j)\Delta p'(j)+p_o'(j)\Delta p(j) \qquad \text{(A1)}$$

where the quadratic term in the small quantities $\Delta p(j)$ and $\Delta p'(j)$ has been neglected. Replacing $\Delta p(j)$ by $p(j) - p_o(j)$ and $\Delta p'(j)$ by $p'(j) - p_o'(j)$, we can write

$$p(j)p'(j) \approx p(j)p_o'(j) + p_o(j)p'(j) - p_o(j)p_o'(j) \qquad \text{(A2)}$$

The linearized form of Eq. (12a) can now be written as†;

---

†an equivalent form exists for q, with p_o replaced by q_o and v_p replaced by $-v_p$.

$$[1+p_o^2(j)]\,p''(j) + \left\{-6P_o(j)p_o'(j) + \frac{[1+p_o(j)^2]^2}{x(j)} - \frac{p_o(j)^2[1+p_o(j)^2]}{x(j)}\right\} p'(j)$$

$$+ \left\{2p_o(j)p_o''(j) - 3p_o'(j)^2 + \frac{4p_o(j)p_o'(j)[1+p_o(j)^2]}{x(j)} - \frac{2p_o(j)p_o'(j)[1+2p_o(j)^2]}{x(j)}\right.$$

$$\left. - \frac{3V_p kT}{\Omega D_s \delta_s \gamma_s}\, x(j)p_o(j)\,[1+p_o(j)^2]^2 - \frac{1}{x(j)^2}\,[1+p_o(j)^2][1+5p_o(j)^2]\right\} p(j)$$

$$= 2p_o(j)^2 p_o''(j) - 6p_o(j)p_o'(j)^2$$

$$+ \frac{4p_o(j)p_o'(j)[1+p_o(j)^2]}{x(j)} - \frac{2p_o(j)^2 p_o'(j)[1+2p_o(j)^2]}{x(j)}$$

$$- \frac{4}{x(j)^2}\,p_o(j)^3\,[1+p_o(j)^2]$$

$$+ \frac{V_p kT}{2\Omega D_s \delta_s \gamma_s}\, x(j)\,[1-3p_o(j)^2-9p_o(j)^4-5p_o(j)^6] \qquad \text{(A3)}$$

while the boundary conditions can be expressed as;

$$[1+cq_o(1)]\, p(1) + [1+cp_o(1)]\, q(1) = c\, [1+p_o(1)\, q_o(1)] \qquad \text{(A4)}$$

and,

$$ep'(1) + fq'(1) + gp(1) + hq(1) = k \qquad \text{(A5)}$$

where

$$e = 2[1+q_o(1)^2]^3 \left\{ p_o'(1) + \frac{p_o(1)[1+p_o(1)^2]}{x(1)} \right\}$$

$$f = -2[1+p_o(1)^2]^3 \left\{ q_o'(1) + \frac{q_o(1)[1+q_o(1)^2]}{x(1)} \right\}$$

$$g = [2/x(1)][1+3p_o(1)^2][1+q_o(1)^2]^3 \left\{ p_o'(1) + \frac{p_o(1)}{x(1)} [1+p_o(1)^2] \right\}$$

$$- 6p_o(1) [1+p_o(1)^2]^2 \left\{ q_o'(1) + \frac{q_o(1)}{x(1)} [1 + q_o(1)^2] \right\}^2$$

$$h = -[2/x(1)][1+3q_o(1)^2]^2 [1+p_o(1)^2]^3 \left\{ q_o'(1) + \frac{q_o(1)}{x(1)} [1+q_o(1)^2] \right\}$$

$$+ 6q_o(1) [1+q_o(1)^2]^2 \left\{ p_o(1) + \frac{p_o(1)}{x(1)} [1+p_o(1)^2] \right\}^2$$

$$k = f[p_o(1),q_o(1)] - f[q_o(1),p_o(1)]$$

$$f(p_o,q_o) = p_o'^2 (1+9q_o^2 + 15q_o^4 + 7p_o^6) + [2/x(1)]p_o'p_o[1+9q_o^2 + 15q_o^4 + 7q_o^6$$

$$+ 3p_o^2 (1 + 5q_o^2 + 7q_o^4 + 3q_o^6)] + [1/x(1)^2]p_o[1 + 6p_o^2 + 9q_o^2 + 5p_o^4$$

$$+ 30p_o^2 q_o^2 + 15q_o^4 + 42p_o^2 q_o^4 + 21p_o^4 q_o^2 + 7q_o^6 + 18p_o^2 q_o^6$$

$$+ 27p_o^4 q_o^4 + 11p_o^4 q_o^6]$$

for purposes of finite difference analysis the derivatives are approximated by;

$$p'(j) = \frac{p(j+1) - p(j-1)}{2\Delta x} \qquad (j = 1 \sim N) \qquad (A6)$$

$$p''(j) = \frac{p(j+1) - 2p(j) + p(j-1)}{(\Delta x)^2}$$

where N+1 is the number of points in the finite difference scheme for each quadrant of the pore surface. Symmetry requires that;

$$p(N+1) = 0 \qquad (A7)$$

There is no point below j = 1. However, in order to define p'(1) and p''(1) an imaginary point 0 is added. The finite difference forms of the boundary conditions, coupled with the differential equations at j=1, permit the imaginary point to be eliminated. The problem then reduces to two tridiagonal matrices, and the standard methods of forward reduction and backward substitution can be used to solve for p(j) and q(j). Successive iteration is used to obtain convergent values. Finally, the pore shape is determined from the slopes p and q.

APPENDIX II

Determination of the Pore Shape

The pore shape can be determined from the slope solutions of Appendix I, starting with the finite difference expression for the slope[†]

$$p(j) = \frac{Y(j+1) - Y(j-1)}{2\Delta x} \qquad (j = 2 \sim N)$$

$$Y(j+1) = Y(j-1) + 2P(j)\Delta x \tag{B1}$$

with the pore tip located on the x-axis,

$$Y(1) = 0 \tag{B2}$$

However, the position of point 2 (or the imaginary point) is still needed in order to solve for the pore shape.

The slope and the derivative of the slope at point 1 can be expressed by

$$p(1) = \frac{Y(2) - Y(0)}{2\Delta x} \tag{B3}$$

$$p'(1) = \frac{Y(2) - 2Y(1) + Y(0)}{(\Delta x)^2} \tag{B4}$$

[†]A similar calculation may be used for q(j)

Combining Eqs. (B2), (B3) and (B4), we can derive

$$Y(2) = \left\{P(1) + [P(2) - P(0)]/4\right\} \Delta x \qquad \text{(B5)}$$

Eqs. (B1), (B2) and (B5) allow us to derive the pore shape.

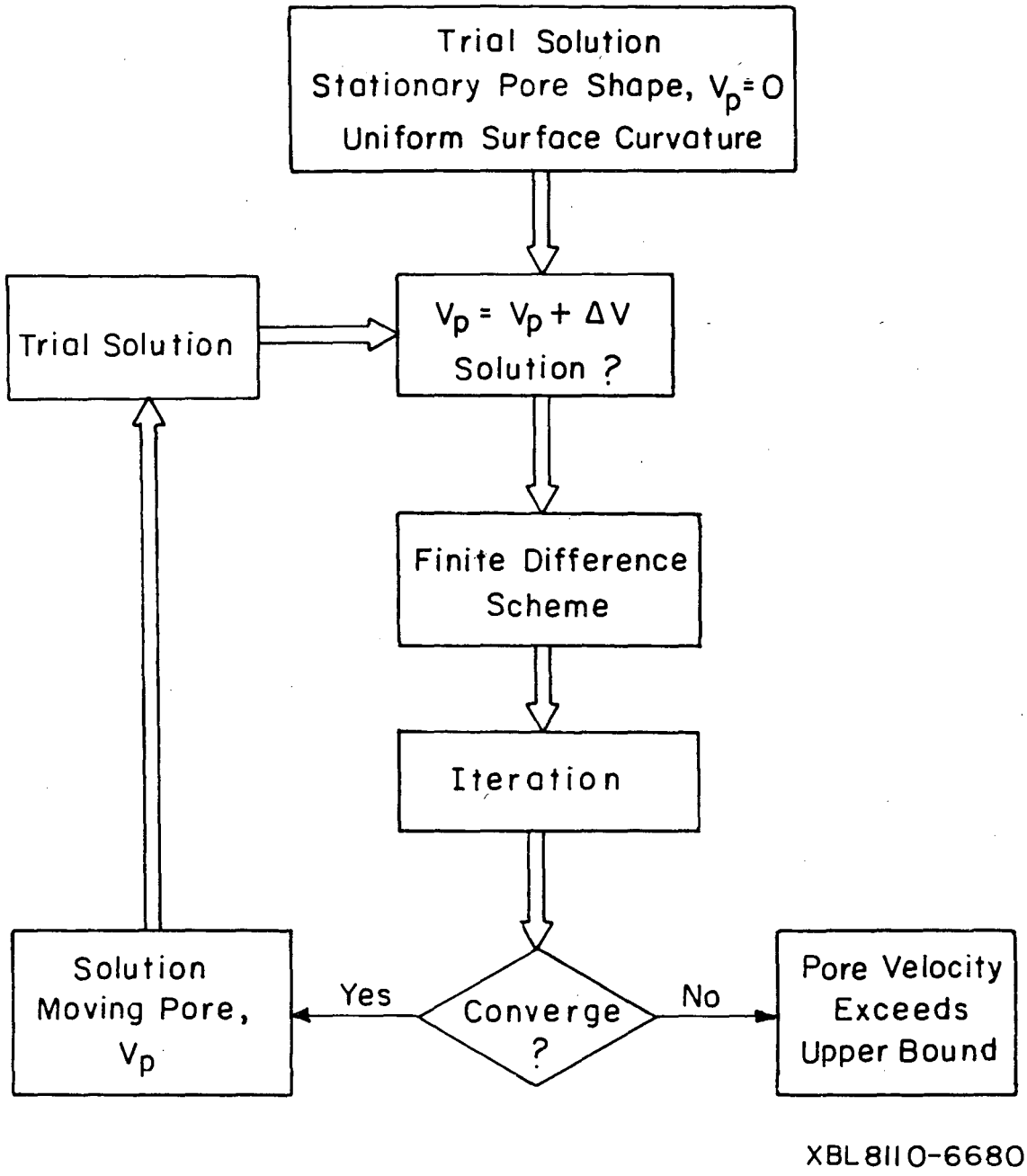

Flow chart of the program.

```
      PROGRAM HSUEH(INPUT,OUTPUT)
C                              CHUN-HWAY HSUEH
C                 DEPARTMENT OF MATERIALS SCIENCE AND MINERAL ENGINEERING
C                              UNIVERSITY OF CALIFORNIA, BERKELEY
C                                       APRIL 1981
C     OBJECTIVE *PORE SHAPE ANALYSIS*
C     THE PORE SHAPE IS DETERMINED BY THE DIHEDRAL ANGLE AND THE PORE VE
C     LOCITY. SURFACE DIFFUSION IS THE TRANSPORT MECHANISM. LINEARIZATIO
C     N OF A NON-LINEAR DIFFERENTIAL EQUATION IS USED TO SOLVE THE PROBL
C     EM. STARTING FROM THE SOLUTION FOR THE STATIONARY PORE, A SERIES O
C     F SUCCESSIVE ITERATIONS BY SMALL INCREMENTS OF PORE VELOCITY IS US
C     ED TO OBTAIN THE SOLUTION FOR A MOVING PORE.
C     ------------------------------------------------------------------
C     ***INPUT DATA***
C     1. TOTAL DIHEDRAL ANGLE.
C     2. PORE RADIUS.
C     3. NUMBER OF POINTS USED IN THE FINITE DIFFERENCE SCHEME.
C     4. NUMBER OF ITERATIONS IN EACH SET.
C     5. PORE VELOCITY (CONTINUOUS READING BY SMALL INCREMENTS)
C     ***OUTPUT SOLUTIONS FOR EACH PORE VELOCITY***
C     1. SLOPE AT SEVERAL POINTS FOR EACH ITERATION.
C     2. PARTIAL DIHEDRAL ANGLES, PSI 1 AND PSI 2.
C     3. PORE SHAPE.
C     4. PORE RADIUS.
C     4. PORE VOLUME.
C     5. PORE RADIUS, NORMALIZED BY THE STATIONARY PORE VOLUME.
C     ***IF THE PORE VELOCITY EXCEEDS THE UPPER BOUND, THE ITERATION
C        WILL NOT CONVERGE.
C     ------------------------------------------------------------------
      DIMENSION X(101),P(101),Q(101),AR(101),AS(101),AT(101),AU(101),BR(
     1101),BS(101),BT(101),BU(101),YU(101),YL(101)
      READ 1,PSI,PR,N,NO
    1 FORMAT(2F5.1,2I3)
      PI=4.*ATAN(1.)
      C=TAN(PSI*PI/180.)
      CO=TAN(PSI*PI/360.)
      DX=PR/FLOAT(N)
      DX2=DX**2
      DXX=2.*DX
      DXY=DX/2.
C-----P(I) IS THE SLOPE AT POINT I OF THE TRAILING SURFACE OF THE PORE
C-----Q(I) IS THE SLOPE AT POINT I OF THE LEADING SURFACE OF THE PORE
C-----X(I) IS THE X POSITION AT POINT I
      N1=N+1
      DO 11 I=1,N1
      X(I)=-PR+PR*FLOAT(I-1)/FLOAT(N)
   11 CONTINUE
C-----SET SLOPE VALUE OF THE STATIONARY PORE
      R=PR**2*(1.+1./CO**2)
      DO 19 I=1,N1
      P(I)=-X(I)/SQRT(R-X(I)**2)
      Q(I)=P(I)
```

```
   19 CONTINUE
      PO=-(X(1)-DX)/SQRT(R-(X(1)-DX)**2)
      QO=PO
      NI=IFIX(N/10+0.001)
C-----CALCULATION OF THE VOLUME OF THE STATIONARY PORE
      VP=PI*(2.*R*SQRT(R)/3.-PR*(2.*R/3.+PR**2/3.)/CO)*2.
C-----COTINUOUS READING OF VELOCITY DATA BY SMALL INCREMENTS
   18 CONTINUE
      READ 8,V
    8 FORMAT(F6.2)
      IF(V.EQ.0.) STOP
      PRINT 2,PSI,PR,V,N,NO
    2 FORMAT(*1PORE SHAPE ANALYSIS   (LINEARIZATION OF NON-LINEAR DIFFER
     1ENTIAL EQUATION)*/* DIHEDRAL ANGLE(DEGREE)=*F5.1/* PORE RADIUS=*F5
     2.1/* NORMALIZED PORE VELOCITY=*F6.2/* NUMBER OF POINTS IN FINITE D
     3IFFERENCE SCHEME=*I3/* NUMBER OF ITERATIONS=*I3)
      PRINT 3,(X(I),I=1,N1,NI)
    3 FORMAT(//* SOLUTIONS   */* P IS THE SLOPE OF THE TRAILING SURFACE
     1OF THE PORE*/* Q IS THE SLOPE OF THE LEADING SURFACE OF THE PORE *
     2/* N.O.I. IS THE NUMBER OF ITERATIONS*/* ----------------------
     3----------------------------------------------------------------
     4----------------------------------------*/*    N.O.I.*54X,*X POSIT
     5ION*/13X,*IMAGINARY*,F8.2,10F10.2/* -------------------------------
     6----------------------------------------------------------------
     7-------+-------------------------*)
      PRINT 4,PO,(P(I),I=1,N1,NI)
    4 FORMAT(/F18.2,11F10.2)
      PRINT 5,QO,(Q(I),I=1,N1,NI)
    5 FORMAT(/F23.2,11F10.2)
C-----ITERATION FOR THE FOLLOWING STEPS (WITH NEW P(I) AND Q(I))
      DO 12 NOI=1,NO
C-----SET FIRST DERIVATIVE OF SLOPE AT POINT 1
      DP=(P(2)-PO)/DXX
      DQ=(Q(2)-QO)/DXX
C-----DEFINE VARIABLES WHICH RELATE TO BOUNDARY CONDITIONS
      P2=P(1)**2
      P4=P2**2
      P6=P4*P2
      Q2=Q(1)**2
      Q4=Q2**2
      Q6=Q4*Q2
      PP=1.+P2
      QQ=1.+Q2
      PP3=PP**3
      QQ3=QQ**3
      A=1.+C*Q(1)
      B=1.+C*P(1)
      D=C*(1.+P(1)*Q(1))
      E=2.*QQ3*(DP+P(1)*PP/X(1))
      F=-2.*PP3*(DQ+Q(1)*QQ/X(1))
      G=2.*(1.+3.*P2)*QQ3*(DP+P(1)*PP/X(1))/X(1)-6.*P(1)*PP*PP*(DQ+Q(1)*
     1QQ/X(1))**2
      H=-2.*(1.+3.*Q2)*PP3*(DQ+Q(1)*QQ/X(1))/X(1)+6.*Q(1)*QQ*QQ*(DP+P(1)
     1*PP/X(1))**2
      AK=DP*DP*(1.+9.*Q2+15.*Q4+7.*Q6)+2.*DP*P(1)*(1.+9.*Q2+15.*Q4+7.*Q6
     1+3.*P2*(1.+5.*Q2+7.*Q4+3.*Q6))/X(1)+P(1)*(1.+6.*P2+9.*Q2+5.*P4+30.
     2*P2*Q2+15.*Q4+42.*P2*Q4+21.*P4*Q2+7.*Q6+18.*P2*Q6+27.*P4*Q4+11.*P4
```

```
     3*Q6)/X(1)**2-DQ*DQ*(1.+9.*P2+15.*P4+7.*P6)-2.*DQ*Q(1)*(1.+9.*P2+15
     4.*P4+7.*P6+3.*Q2*(1.+5.*P2+7.*P4+3.*P6))/X(1)-Q(1)*(1.+6.*Q2+9.*P2
     5+5.*Q4+30.*P2*Q2+15.*P4+42.*Q2*P4+21.*Q4*P2+7.*P6+18.*Q2*P6+27.*Q4
     6*P4+11.*Q4*P6)/X(1)**2
      AE=E/DXX
      AF=F/DXX
C-----DEFINE VARIABLES FOR THE TRI-DIAGONAL MATRIX
      DO 13 J=1,N
      IF(J.EQ.1) GO TO 14
      I=J-1
      K=J+1
      DP=(P(K)-P(I))/DXX
      DQ=(Q(K)-Q(I))/DXX
      DDP=(P(K)-2.*P(J)+P(I))/DX2
      DDQ=(Q(K)-2.*Q(J)+Q(I))/DX2
      GO TO 15
   14 CONTINUE
      DDP=(P(2)-2.*P(1)+PO)/DX2
      DDQ=(Q(2)-2.*Q(1)+QO)/DX2
   15 CONTINUE
      PJ2=P(J)**2
      PJ4=PJ2**2
      PJ6=PJ4*PJ2
      DP2=DP**2
      AA=1.+PJ2
      AB=-6.*P(J)*DP+AA/X(J)
      AC=2.*P(J)*DDP-3.*DP2+2.*P(J)*DP/X(J)-3.*V*P(J)*AA*AA*X(J)-AA*(1.+
     15.*PJ2)/X(J)**2
      AD=2.*PJ2*DDP-6.*P(J)*DP2+2.*PJ2*DP/X(J)+V*(1.-3.*PJ2-9.*PJ4-5.*PJ
     16)*X(J)/2.-4.*PJ2*P(J)*AA/X(J)**2
      AR(J)=AA-AB*DXY
      AS(J)=-2.*AA+AC*DX2
      AT(J)=AA+AB*DXY
      AU(J)=AD*DX2
      QJ2=Q(J)**2
      QJ4=QJ2**2
      QJ6=QJ4*QJ2
      DQ2=DQ**2
      BA=1.+QJ2
      BB=-6.*Q(J)*DQ+BA/X(J)
      BC=2.*Q(J)*DDQ-3.*DQ2+2.*Q(J)*DQ/X(J)+3.*V*Q(J)*BA*BA*X(J)-BA*(1.+
     15.*QJ2)/X(J)**2
      BD=2.*QJ2*DDQ-6.*Q(J)*DQ2+2.*QJ2*DQ/X(J)-V*(1.-3.*QJ2-9.*QJ4-5.*QJ
     16)*X(J)/2.-4.*QJ2*Q(J)*BA/X(J)**2
      BR(J)=BA-BB*DXY
      BS(J)=-2.*BA+BC*DX2
      BT(J)=BA+BB*DXY
      BU(J)=BD*DX2
   13 CONTINUE
C-----VARIABLE STORAGE, USED LATER TO CALCULATE NEW SLOPE VALUE AT THE I
C-----MAGINARY POINT
      ASS=AS(1)
      ATS=AT(1)
      AUS=AU(1)
      BSS=BS(1)
      BTS=BT(1)
      BUS=BU(1)
```

```
C-----DEFINE FIRST ROW OF THE TRI-DIAGONAL MATRIX (COOPERATE WITH B.C.)
      AS1=AS(1)+AR(1)*(G-H*A/B-AF*BS(1)*A/(BR(1)*B))/AE
      AT1=AT(1)+AR(1)
      AU1=AU(1)-AR(1)*AF*(1.+BT(1)/BR(1))*Q(2)/AE+AR(1)*(AK-H*D/B+AF*(BU
     1(1)-BS(1)*D/B)/BR(1))/AE
      BS1=BS(1)+BR(1)*(H-G*B/A-AE*AS(1)*B/(AR(1)*A))/AF
      BT1=BT(1)+BR(1)
      BU1=BU(1)-BR(1)*AE*(1.+AT(1)/AR(1))*P(2)/AF+BR(1)*(AK-G*D/A+AE*(AU
     1(1)-AS(1)*D/A)/AR(1))/AF
      AS(1)=AS1
      AT(1)=AT1
      AU(1)=AU1
      BS(1)=BS1
      BT(1)=BT1
      BU(1)=BU1
C-----SOLUTION OF THE TRI-DIAGONAL MATRIX-----1. FORWARD REDUCTION
      DO 16 L=2,N
      L1=L-1
      ARS=AR(L)/AS(L1)
      AS(L)=AS(L)-ARS*AT(L1)
      AU(L)=AU(L)-ARS*AU(L1)
      BRS=BR(L)/BS(L1)
      BS(L)=BS(L)-BRS*BT(L1)
      BU(L)=BU(L)-BRS*BU(L1)
   16 CONTINUE
C-----SOLUTION OF THE TRI-DIAGONAL MATRIX-----2. BACK SUBSTITUTION
      P(N)=AU(N)/AS(N)
      Q(N)=BU(N)/BS(N)
      DO 17 M=2,N
      II=N+1-M
      JJ=II+1
      P(II)=(AU(II)-AT(II)*P(JJ))/AS(II)
      Q(II)=(BU(II)-BT(II)*Q(JJ))/BS(II)
   17 CONTINUE
C-----DEFINE NEW SLOPE VALUE AT THE IMAGINARY POINT
      PO=(AUS-ATS*P(2)-ASS*P(1))/AR(1)
      QO=(BUS-BTS*Q(2)-BSS*Q(1))/BR(1)
C-----PRINT SLOPE VALUES FOR SEVERAL POINTS FOR EACH ITERATION
      PRINT 6,NOI,PO,(P(I),I=1,N1,NI)
    6 FORMAT(/* P*,I5,F11.2,11F10.2)
      PRINT 7,NOI,QO,(Q(I),I=1,N1,NI)
    7 FORMAT(/* Q*,I5,F16.2,11F10.2)
   12 CONTINUE
C-----CALCULATION OF THE DIHEDRAL ANGLE
C-----PSI1 IS THE DIHEDRAL ANGLE OF THE TRAILING PART
C-----PSI2 IS THE DIHEDRAL ANGLE OF THE LEADING PART
C-----SI IS THE INCLINATION ANGLE
      PSI1=ATAN(P(1))*180./PI
      PSI2=ATAN(Q(1))*180./PI
      SI=(PSI1-PSI2)/2.
      PRINT 9,PSI1,PSI2,SI
    9 FORMAT(/* ----------------------------------------------------------
     1*/* DESCRIPTION OF THE PORE SHAPE*/* ----------------------------
     2--------------------------*/* DIHEDRAL ANGLE (DEGREE) OF THE TRAI
     3LING PART=*F6.2/* DIHEDRAL ANGLE (DEGREE) OF THE LEADING PART=*F7.
     42/* INCLINATION ANGLE (DEGREE)=*F7.2)
C-----CALCULATION OF THE PORE SHAPE
```

```
C-----YU(I) IS THE Y POSITION OF THE TRAILING PART AT POINT I
C-----YL(I) IS THE Y POSITION OF THE LEADING PART AT POINT I
      YU(1)=0.
      YL(1)=0.
      YU(2)=(P(1)+(P(2)-PO)/4.)*DX
      YL(2)=(Q(1)+(Q(2)-QO)/4.)*DX
      DO 21 J=2,N
      I=J-1
      K=J+1
      YU(K)=YU(I)+P(J)*DXX
      YL(K)=YL(I)+Q(J)*DXX
   21 CONTINUE
C-----CALCULATION OF THE PORE VOLUME AND THE SURFACE AREA
C-----VU IS THE VOLUME OF THE TRAILING PART
C-----VL IS THE VOLUME OF THE LEADING PART
      VU=0.
      VL=0.
      AREA=0.
      DO 20 J=1,N
      K=J+1
      XR=(X(J)+DXY)**2*PI
      VU=VU+XR*(YU(K)-YU(J))
      VL=VL+XR*(YL(K)-YL(J))
      AREA=AREA-(X(J)+DXY)*2.*PI*(SQRT((YU(K)-YU(J))**2+DX2)+SQRT((YL(K)
     1-YL(J))**2+DX2))
   20 CONTINUE
      VOL=VU+VL
      AREA=AREA*(VP/VOL)**(2./3.)
C-----CALCULATION OF THE PORE RADIUS ( V VELOCITY) WHICH HAS THE SAME PO
C-----RE VOLUME OF THE STATIONARY PORE
      RR=PR*(VP/VOL)**(1./3.)
C-----RV IS THE PORE VELOCITY NORMALIZED BY THE STATIONARY PORE RADIUS
      RV=V*VOL/VP
      PRINT 10,(X(I),I=1,N1,NI),(YU(I),I=1,N1,NI),(YL(I),I=1,N1,NI),VU,V
     1L,VOL,VP,RR,RV,AREA
   10 FORMAT(//* X POSITION   *11F10.3/* Y POSITION*/* TRAILING PART*11F
     110.3/* LEADING PART *11F10.3//* VOLUME (TRAILING PART)=*F7.3/* VOL
     2UME (LEADING PART)=*F8.3/* TOTAL PORE VOLUME=*F12.3//* VOLUME OF T
     3HE STATIONARY PORE=*F10.3/* PORE RADIUS (NORMALIZED BY THE STATION
     4ARY PORE)=*F6.2/* PORE VELOCITY (NORMALIZED BY STATIONARY PORE RAD
     5IUS)=*F6.3/* PORE SURFACE AREA=*F7.3)
      GO TO 18
      END
'
C-----EXAMPLE (INPUT)
 60.0001.0100020
  1.0
  2.0
  3.0
  4.0
  5.0
  6.0
  6.5
  6.7
  6.8
  6.9
```

APPENDIX III

Modified Phenomenological Analysis

A constant pore mobility (Eq. (1)), a fixed maximum driving force exerted on the pore (Eq. (3)) and hence a constant maximum pore velocity (Eq. (4)) are used in the phenomenological analysis. However, the detailed numerical pore velocity analysis indicates that the maximum pore velocity depends on the dihedral angle (Eq. (17)). A modified phenomenological analysis is thus needed.

Instead of choosing the mobility for a spherical pore, let us consider the pore mobility (by surface diffusion) per atom

$$M_p = \frac{D_s}{kT} \tag{C1}$$

The maximum driving force per atom for the pore motion can be derived from Eqs. (17) and (C1)

$$\hat{F}_p = \frac{\Omega\delta_s\gamma_s}{a_o^3}(17.9 - 6.2\Psi) \tag{C2}$$

which depends on the dihedral angle. Taking into account the reduction of the driving force for grain boundary motion in the case of attachment by the dragging force F_p of the pore, the grain boundary velocity becomes;

$$V_b = M_b(F_b - N\hat{F}_p) \tag{C3}$$

where F_b is the driving force acting on the pore free grain boundary (per atom)

$$F_b = \frac{2\gamma_b \Omega^{2/3}}{R} \tag{C4}$$

$N = a_o^2/R^2$ is the ratio of the number of atoms between the pore surface and the boundary, (assuming that the interpore distance is the grain size). A limiting velocity of separation can now be defined $V_b = \hat{V}_p$, which, in an R, a_o diagram, occurs when,

$$R \frac{D_s \delta_s \gamma_s \Omega^{1/3}}{2 D_b \gamma_b a_o^3} (17.9 - 6.2\Psi) = \frac{1}{1 + \frac{a_o^2 D_b}{R^2 D_s}} \tag{C5}$$

The two limiting cases are

$$R \leqslant \frac{2 D_b \gamma_b a_o^3}{D_s \delta_s \gamma_s \Omega^{1/3} (17.9-6.2\Psi)} \tag{C6}$$

and

$$R \geqslant \delta_s \gamma_s \Omega^{1/3} (17.9-6.2\Psi)/2\gamma_b a_o \tag{C7}$$

REFERENCES

1. J. E. Burke, J. Amer. Ceram. Soc. 40 (1957) 80.

2. B. H. Alexander and R. W. Baluffi, Acta Met. 5 (1957) 666.

3. F. M. A. Carpay, J. Amer. Ceram. Soc. 60 (1977) 82.

4. F. M. A. Carpay, Ceramic Microstructure '76, ed. by R. M. Fulrath and J. A. Pask, Westview Press.

5. M. Hillert, Acta Met. 13 (1965) 227.

6. J. E. Burke, K. W. Lay and S. Prochazka, Sintering Processes, ed. by G. C. Kuczynski, Plenum, New York 1980.

7. A. H. Heuer, J. Amer. Ceram. Soc. 62 (1979) 317.

8. M. P. Harmer and R. J. Brook, J. Mat. Sci. 15 (1980) 3017.

9. P. Kofstad, Nonstoichiometry, Diffusion and Electrical Conductivity in Binary Metal Oxides, Wiley, New York 1972.

10. F. A. Kroger, The Chemistry of Imperfect Crystals, Wiley, New York 1964.

11. M. F. Ashby, Acta Met. 22 (1974) 275.

12. R. L. Coble, J. Amer. Ceram. Soc. 56 (1973) 461.

13. M. F. Ashby and R. M. A. Centamore, Acta Met. 16 (1968) 1081.

14. J. W. Cahn, Acta Met. 10 (1962) 789.

15. R. J. Brook, J. Amer. Ceram. Soc. 52 (1969) 56.

16. M. V. Speight and G. W. Greenwood, Phil. Mag. 9 (1964) 683.

17. R. J. Brook, Treatise on Materials Science and Technology 9 (1976) 331.

18. P. G. Shewmon, Trans. AIME 230 (1964) 1134.

19. J. E. Burke and D. Turnbull, Progress in Metal Physics, ed. by B. Chalmers, Pergamon Press, London, 1952.

20. M. A. Spears and A. G. Evans, to be published.

21. M. Sakarcan and A. G. Evans, to be published.

22. G. W. Greenwood and M. V. Speight, J. Nuclear Mater. 10 (1963) 140.

23. R. S. Barnes and D. J. Mazey, Proc. R. Soc. 275 (1963) 47.

24. T. K. Gupta, J. Amer. Ceram. Soc. 61 (1978) 191.

25. M. Dory and A. G. Evans, to be published.

FIGURE CAPTIONS

Fig. 1. A schematic of the pore separation region given by the phenomenological analysis.

Fig. 2. A schematic of the grain disappearance process involved in grain growth a) exaggerated grain growth involving five-sided grains b) the three-sided configuration associated with ultimate grain disappearance.

Fig. 3. a) A schematic of a moving pore indicating the atom flux and the inclination of the grain boundary, θ.
b) A schematic of the trailing and the leading surfaces in the finite difference scheme.

Fig. 4. Predicted pore shapes for several values of the normalized pore velocity ($\Psi = \pi/3$).

Fig. 5. Pores in MgO subject to motion with the grain boundary.

Fig. 6. a) A plot of the grain boundary inclination as a function of pore velocity for several dihedral angles.
b) A plot of the grain boundary contact radius as a function of the normalized pore velocity.

Fig. 7. The maximum steady-state pore velocity as a function of dihedral angle normalized by a) stationary pore radius b) moving pore radius.

Fig. 8. The shapes of pores when the velocity attains the maximum value.

Fig. 9. A schematic illustrating the development of a counter flux with $\Psi = \pi$ is distorted to achieve a net atom flux and hence, pore motion with the grain boundary.

Fig. 10. A schematic illustrating the shapes of a pore under non-steady-state conditions. For the pore volume to remain contact, the matter removed from the leading surface V_ℓ must equal the matter deposited on the trailing surface, V_t. Additionally, under non-steady state conditions, the average velocity of the leading surface, $\bar{v}_\ell$, must excede that for the trailing surface, $\bar{v}_t$. In order to satisfy these requirements the contact radius a must decrease rapidly with increase in net pore velocity.

Fig. 11. The axisymmetric configuration associated with pore drag, illustrating the important curvatures, the influence distance and the pore and grain boundary velocities.

Fig. 12. Calculated grain boundary shapes for an axisymmetric configuration, subject to uniform chemical potential along the boundary.

Fig. 13. A schematic indicating the change in the axisymmetric radius of curvature that accompanies pore drag with $v_b > v_p$.

Fig. 14. The various separation and admissibility conditions identified in the present analysis, plotted for three values of the dihedral angle.

Fig. 15. A pore created at a three grain junction by a Rayleigh instability and the corresponding pore at a two grain interface.

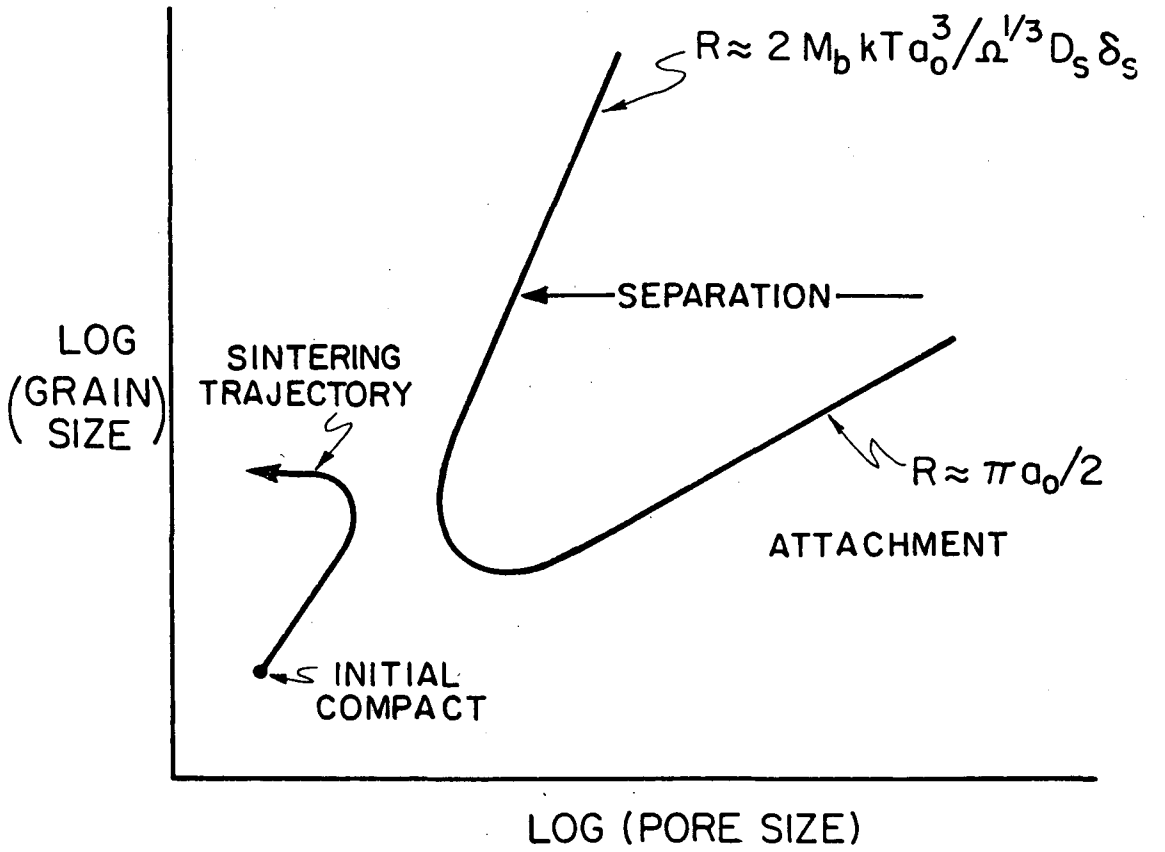
$R \approx 2 M_b kT a_o^3 / \Omega^{1/3} D_s \delta_s$
SEPARATION
LOG (GRAIN SIZE)
SINTERING TRAJECTORY
$R \approx \pi a_o / 2$
ATTACHMENT
INITIAL COMPACT
LOG (PORE SIZE)
XBL816-5971

Fig. II-1

(a)

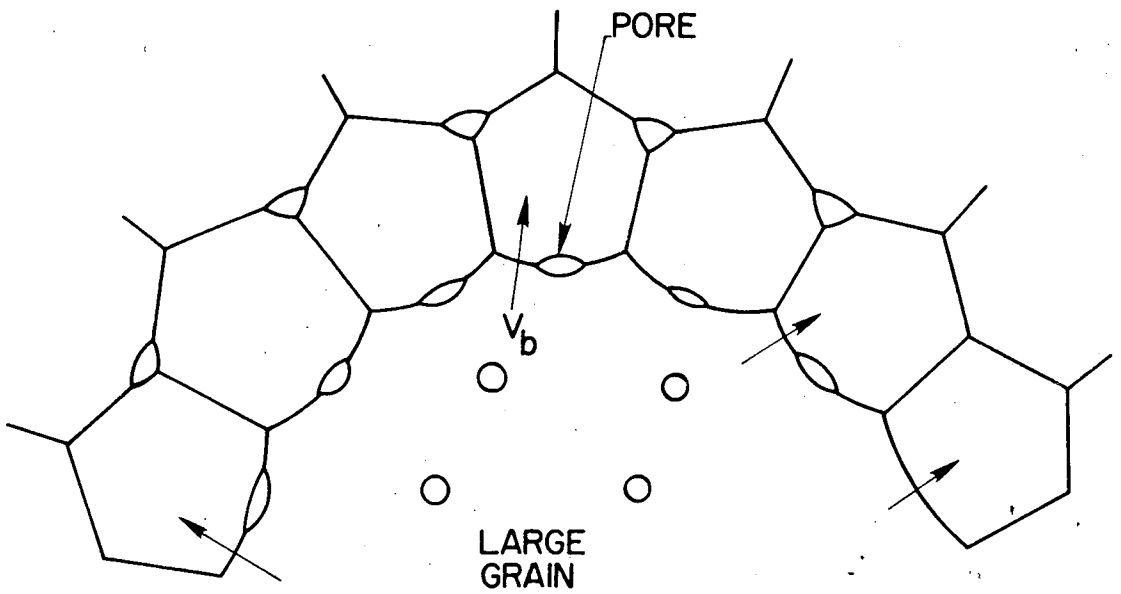

(b)

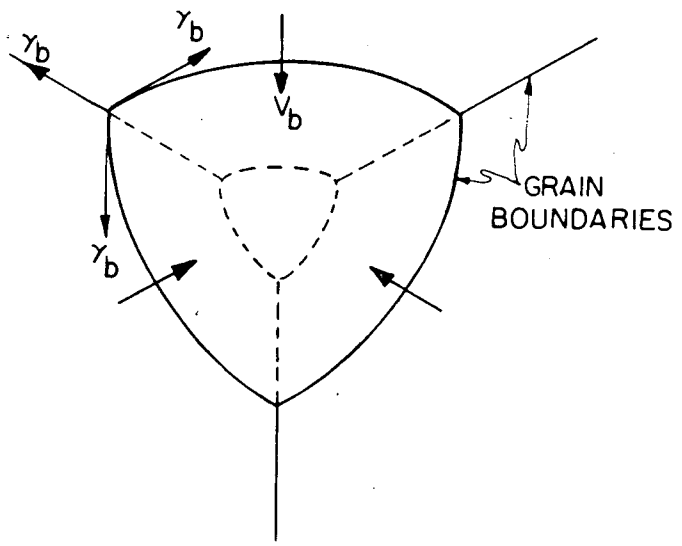

XBL 814-9385

Fig. II-2

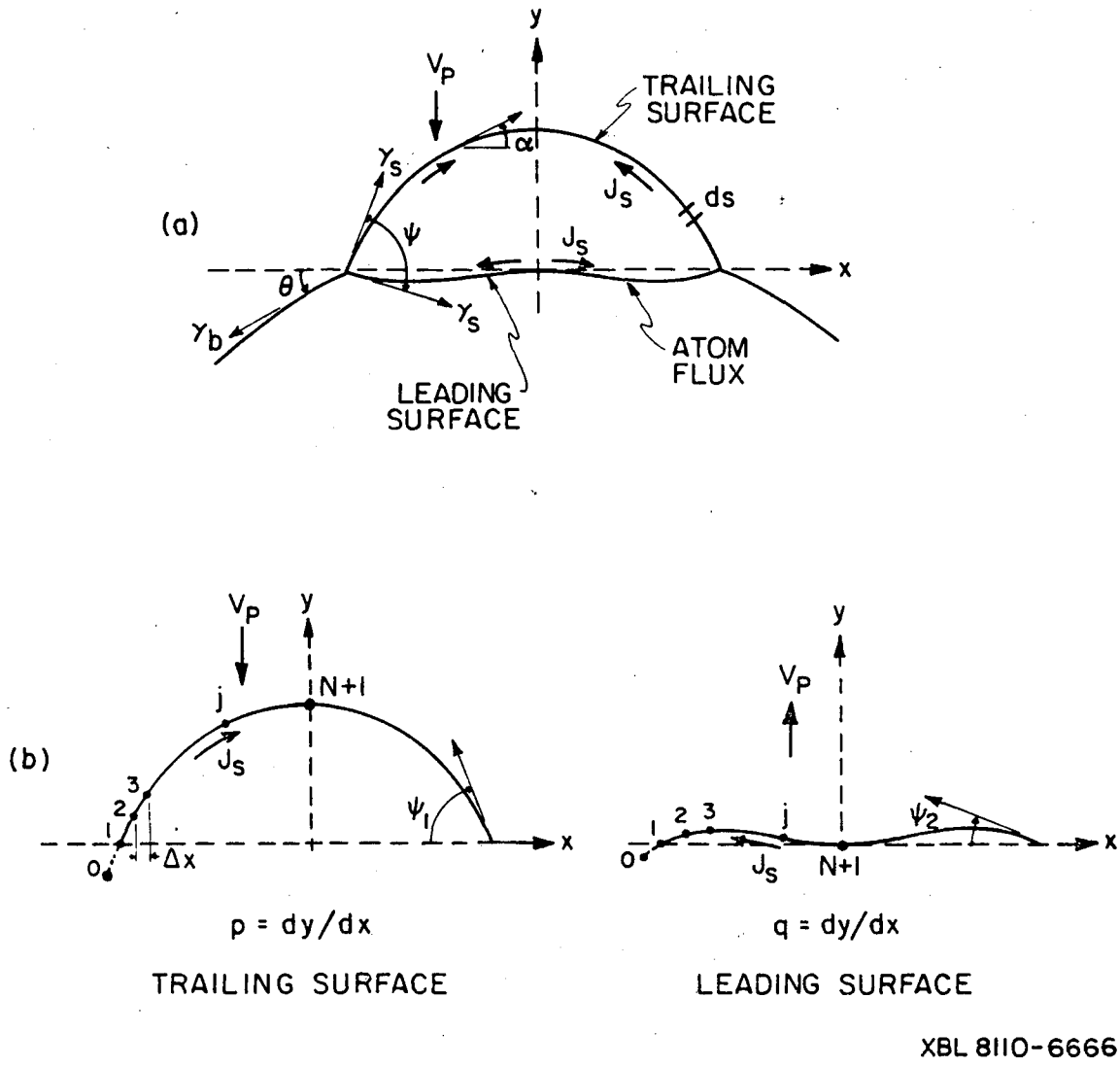
(a)
y
x
V_P
TRAILING SURFACE
α
γ_s
J_s
ds
ψ
J_s
θ
γ_s
γ_b
ATOM FLUX
LEADING SURFACE
(b)
V_P
y
j
N+1
J_s
3
2
1
0
Δx
ψ_1
x
p = dy/dx
TRAILING SURFACE
y
V_P
1
2
3
j
ψ_2
0
J_s
N+1
x
q = dy/dx
LEADING SURFACE
XBL 8110-6666

Fig. II-3

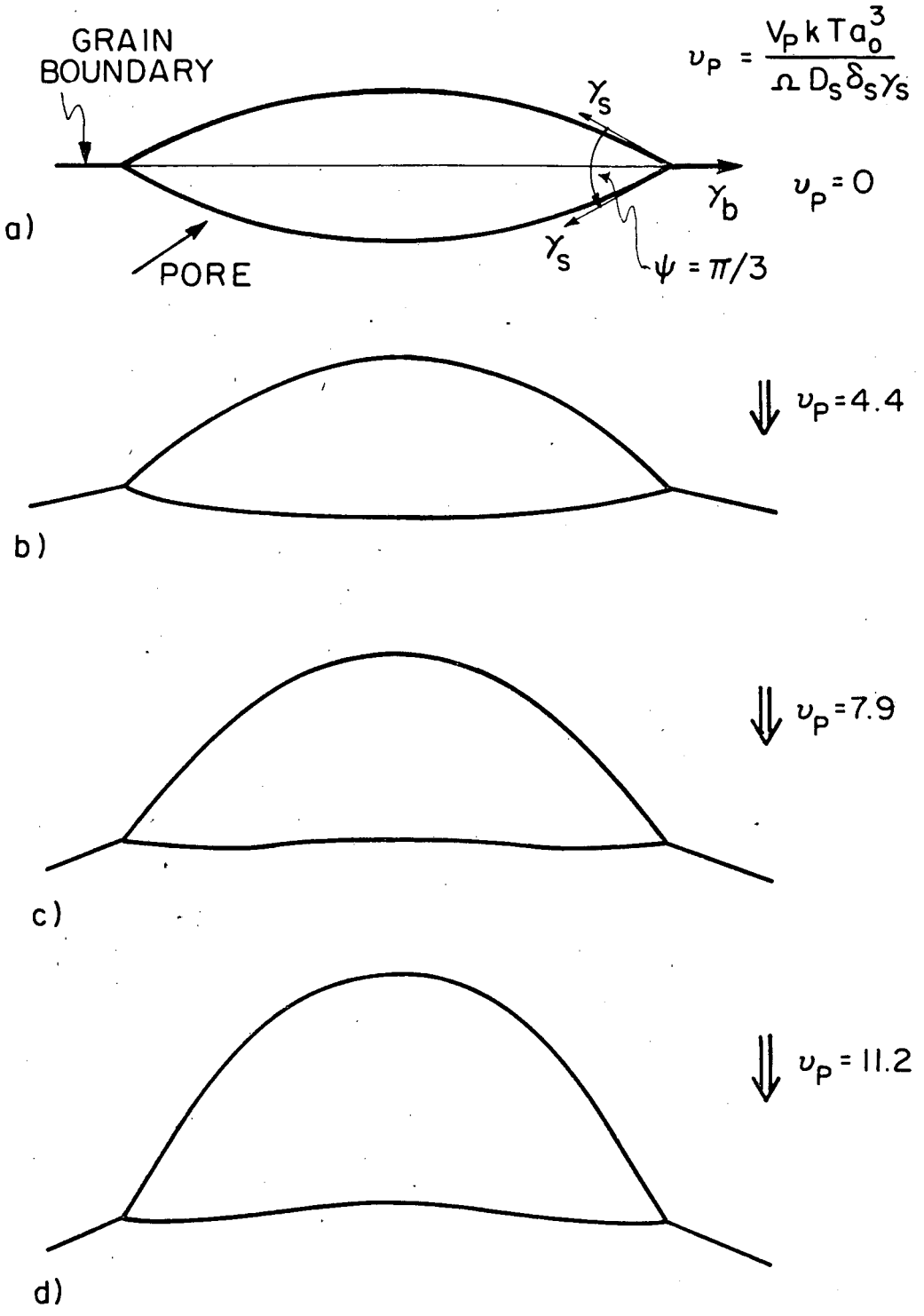
GRAIN BOUNDARY
$v_P = \frac{V_P k T a_o^3}{\Omega D_s \delta_s \gamma_s}$
γ_s
γ_b
$v_P = 0$
a)
PORE
γ_s
$\psi = \pi/3$
$v_P = 4.4$
b)
$v_P = 7.9$
c)
$v_P = 11.2$
d)
XBL 816-5973

Fig. II-4

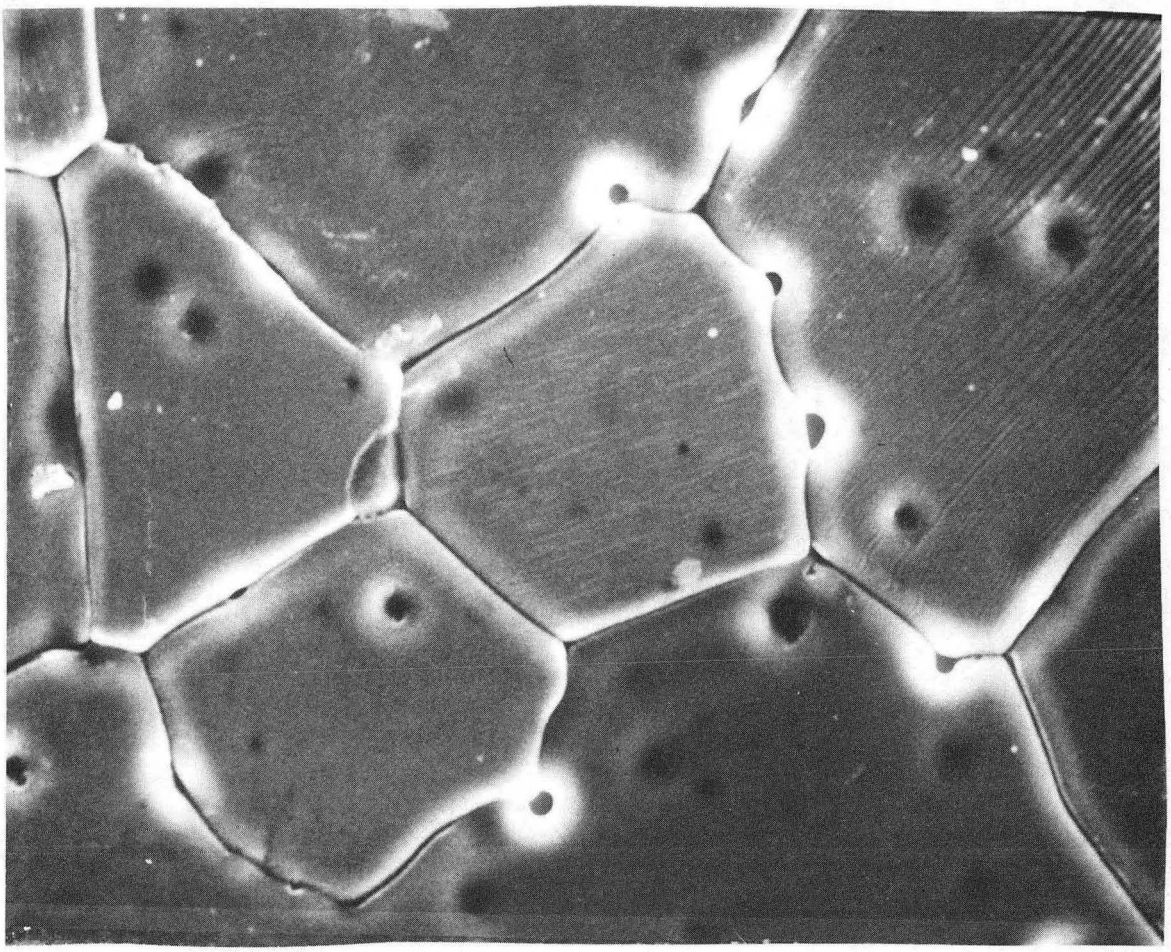

XBB 810-9795

Fig. II-5

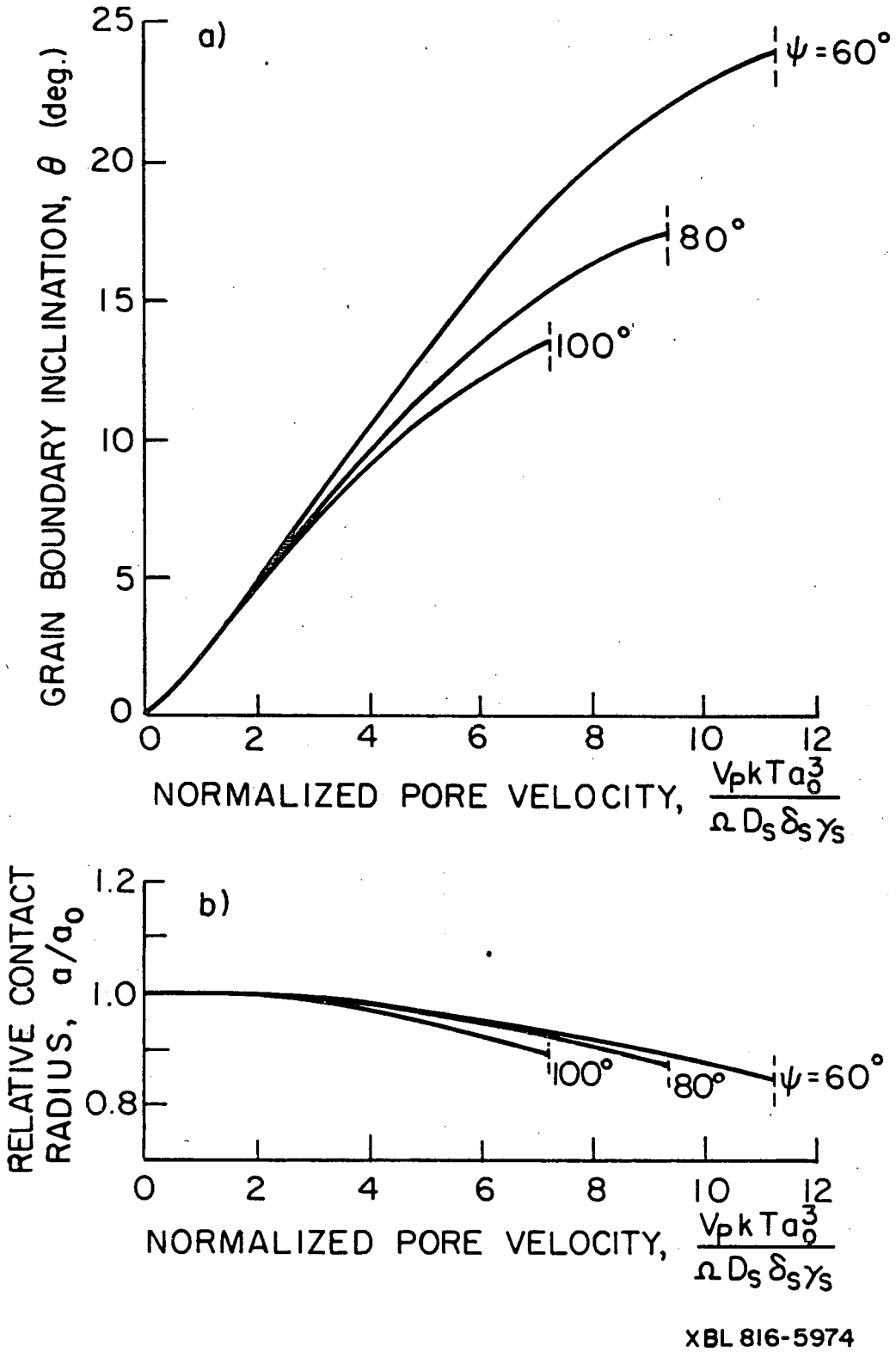
a)
GRAIN BOUNDARY INCLINATION, θ (deg.)
25
20
15
10
5
0
ψ=60°
80°
100°
0
2
4
6
8
10
12
NORMALIZED PORE VELOCITY, $\frac{V_p k T a_o^3}{\Omega D_s \delta_s \gamma_s}$
b)
RELATIVE CONTACT RADIUS, a/a_o
1.2
1.0
0.8
100°
80°
ψ=60°
0
2
4
6
8
10
12
NORMALIZED PORE VELOCITY, $\frac{V_p k T a_o^3}{\Omega D_s \delta_s \gamma_s}$
XBL 816-5974

Fig. II-6

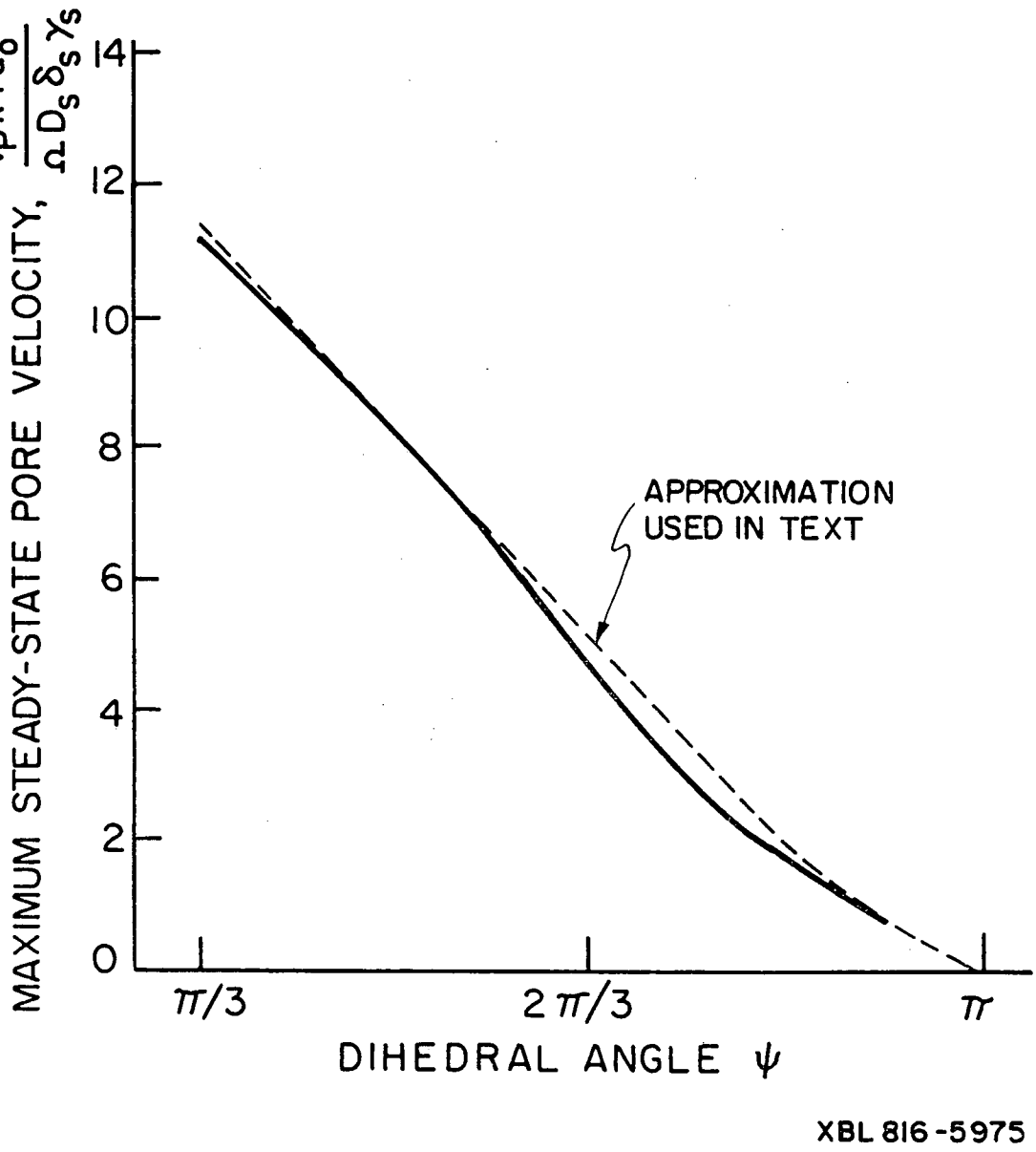
MAXIMUM STEADY-STATE PORE VELOCITY, $\frac{V_p k T a_o^3}{\Omega D_s \delta_s \gamma_s}$
0
2
4
6
8
10
12
14
APPROXIMATION
USED IN TEXT
π/3
2π/3
π
DIHEDRAL ANGLE ψ
XBL 816-5975

Fig. II-7a

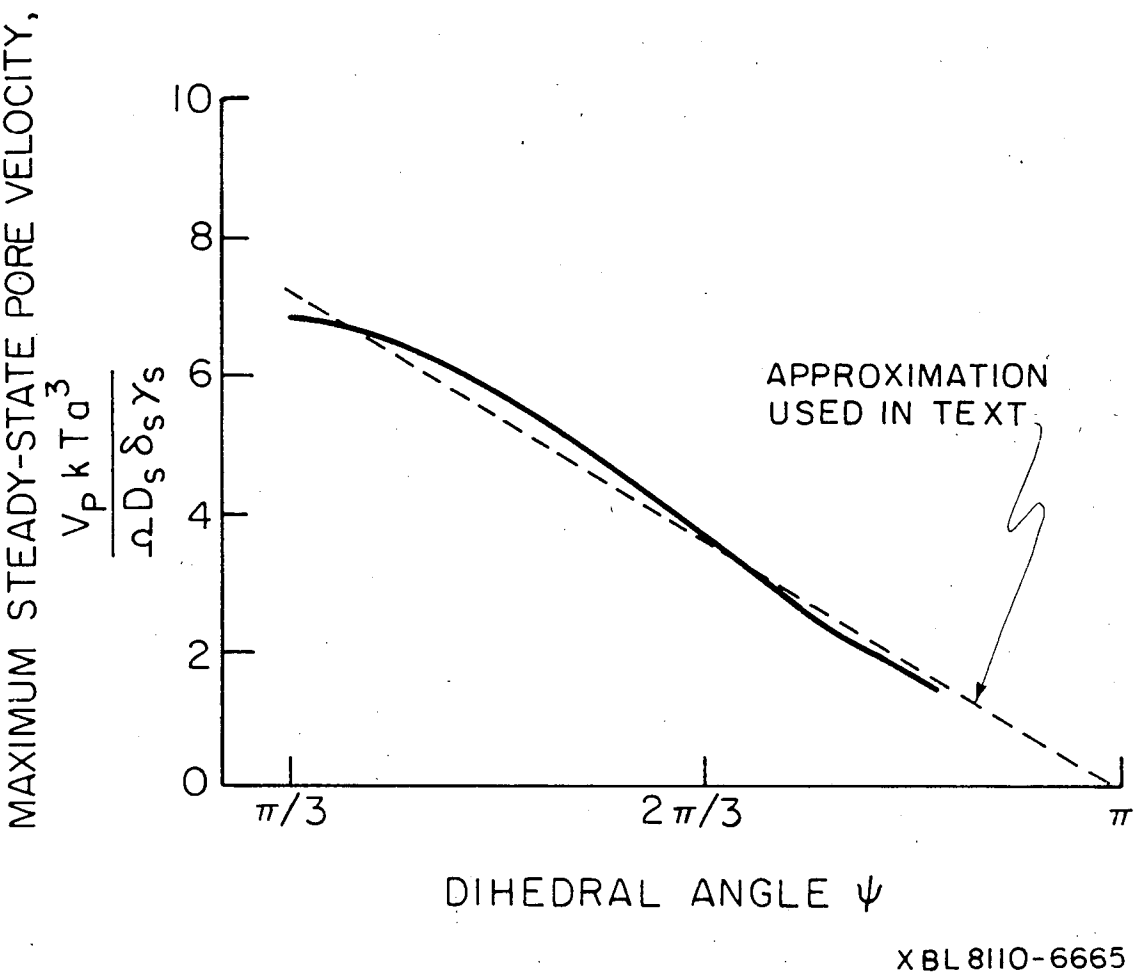
MAXIMUM STEADY-STATE PORE VELOCITY, $\frac{V_p k T a^3}{\Omega D_s \delta_s \gamma_s}$
10
8
6
4
2
0
π/3
2π/3
π
APPROXIMATION USED IN TEXT
DIHEDRAL ANGLE ψ
XBL 8110-6665

Fig. II-7b

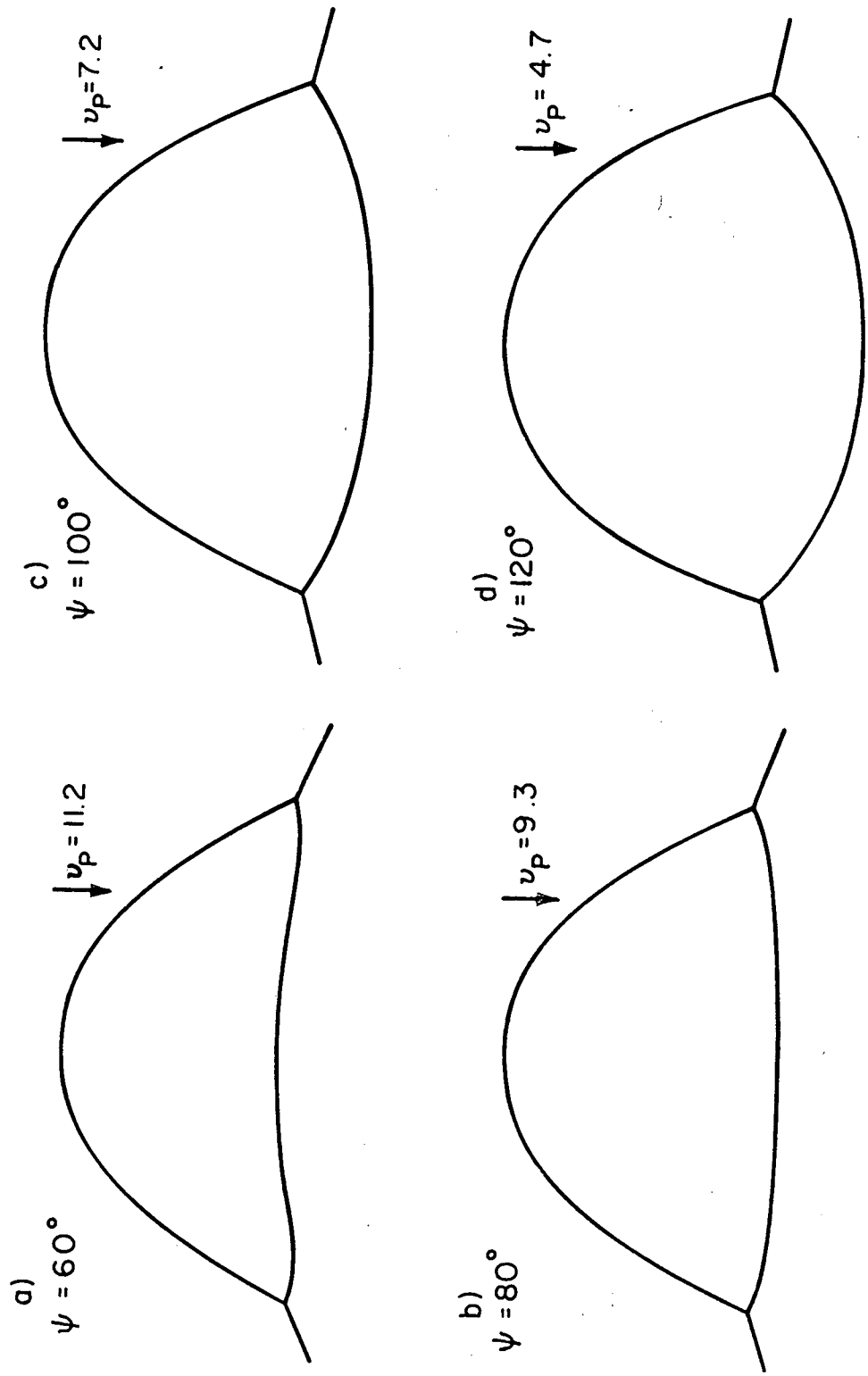

XBL816-5976

Fig. II-8

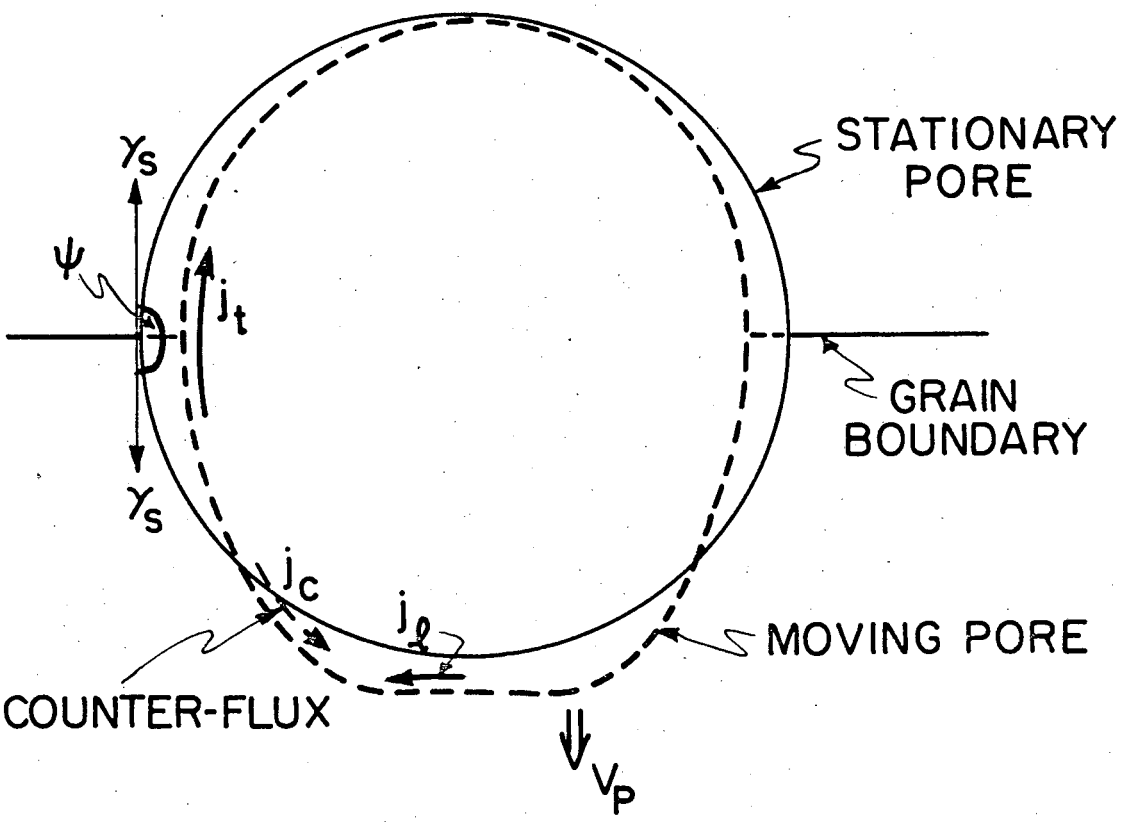
STATIONARY PORE
γ_s
ψ
j_t
GRAIN BOUNDARY
γ_s
j_c
j_ℓ
MOVING PORE
COUNTER-FLUX
V_p
XBL 816-5977

Fig. II-9

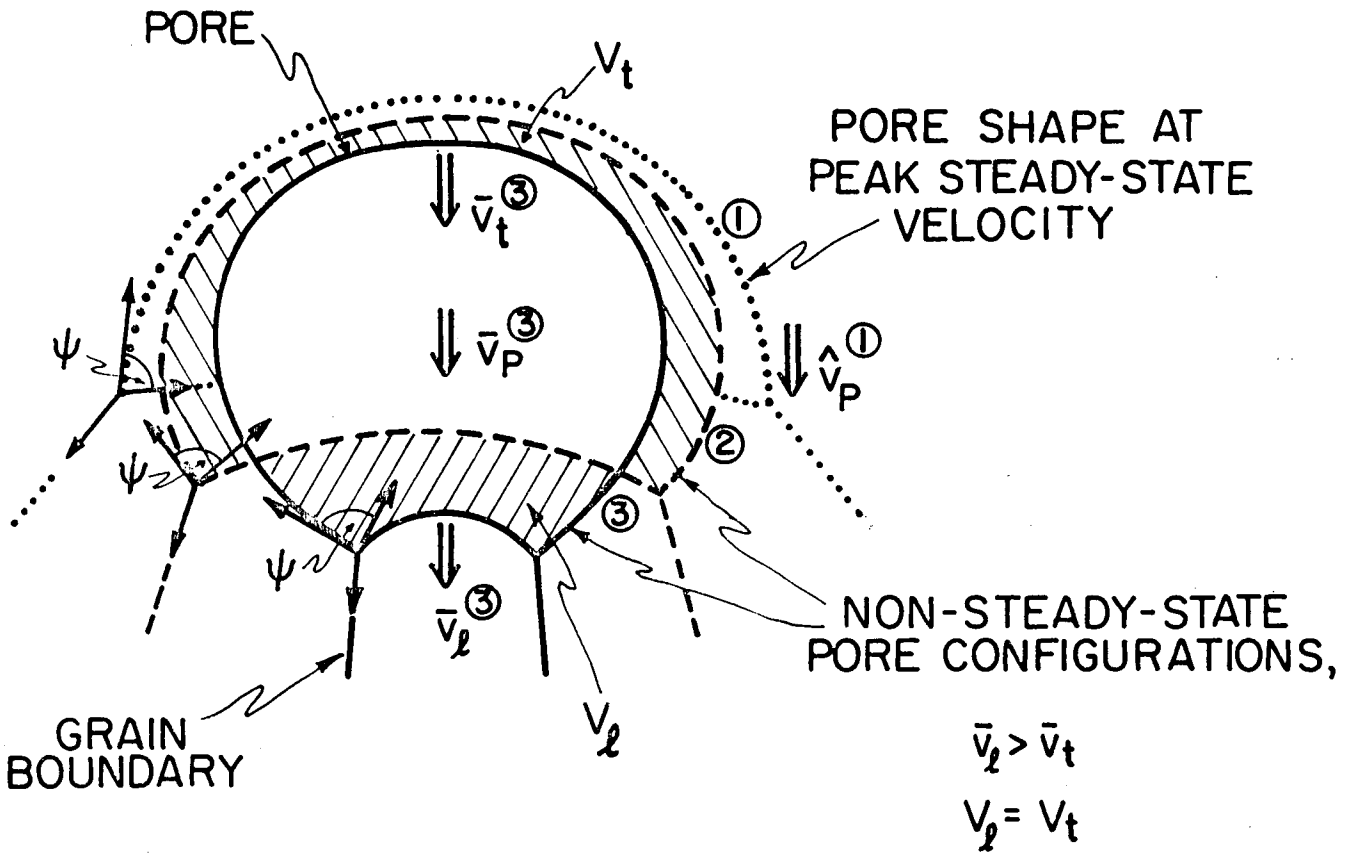
PORE
V_t
PORE SHAPE AT
PEAK STEADY-STATE
VELOCITY
$\bar{v}_t^{③}$
$\bar{v}_P^{③}$
$\hat{v}_P^{①}$
①
②
③
ψ
ψ
ψ
$\bar{v}_\ell^{③}$
NON-STEADY-STATE
PORE CONFIGURATIONS,
$\bar{v}_\ell > \bar{v}_t$
$V_\ell = V_t$
GRAIN
BOUNDARY
V_ℓ
XBL 816-5978

Fig. II-10

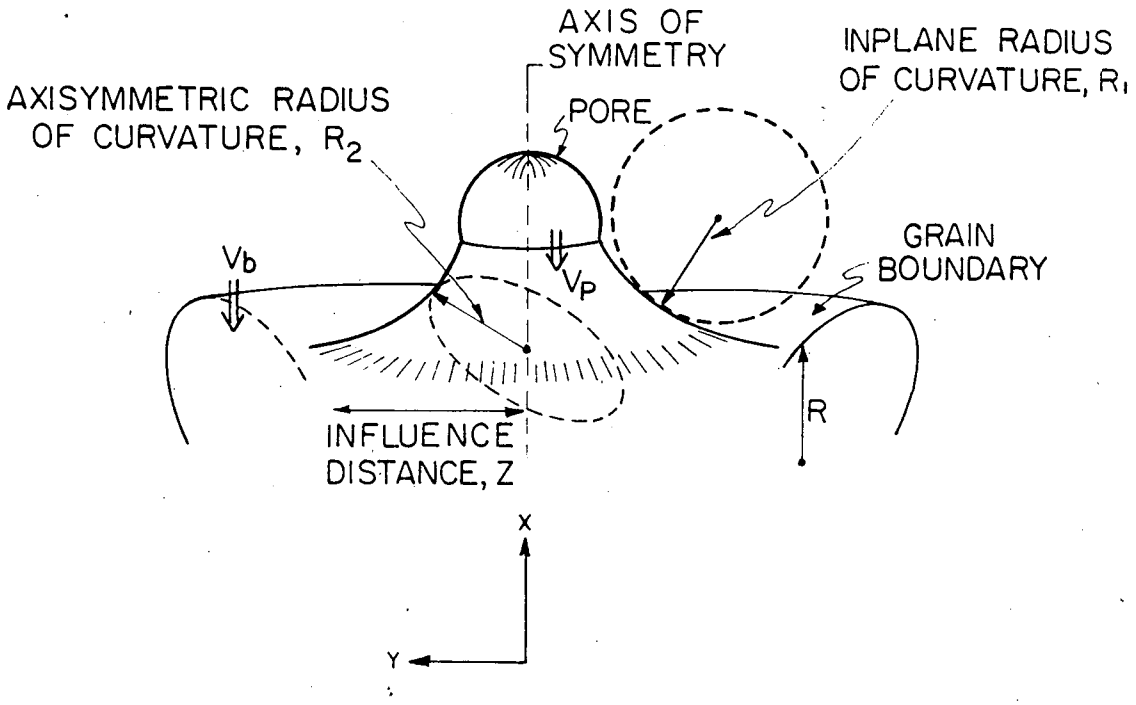
AXIS OF
SYMMETRY
INPLANE RADIUS
OF CURVATURE, R1
AXISYMMETRIC RADIUS
OF CURVATURE, R2
PORE
GRAIN
BOUNDARY
Vb
VP
R
INFLUENCE
DISTANCE, Z
X
Y
XBL 816-5979A

Fig. II-11

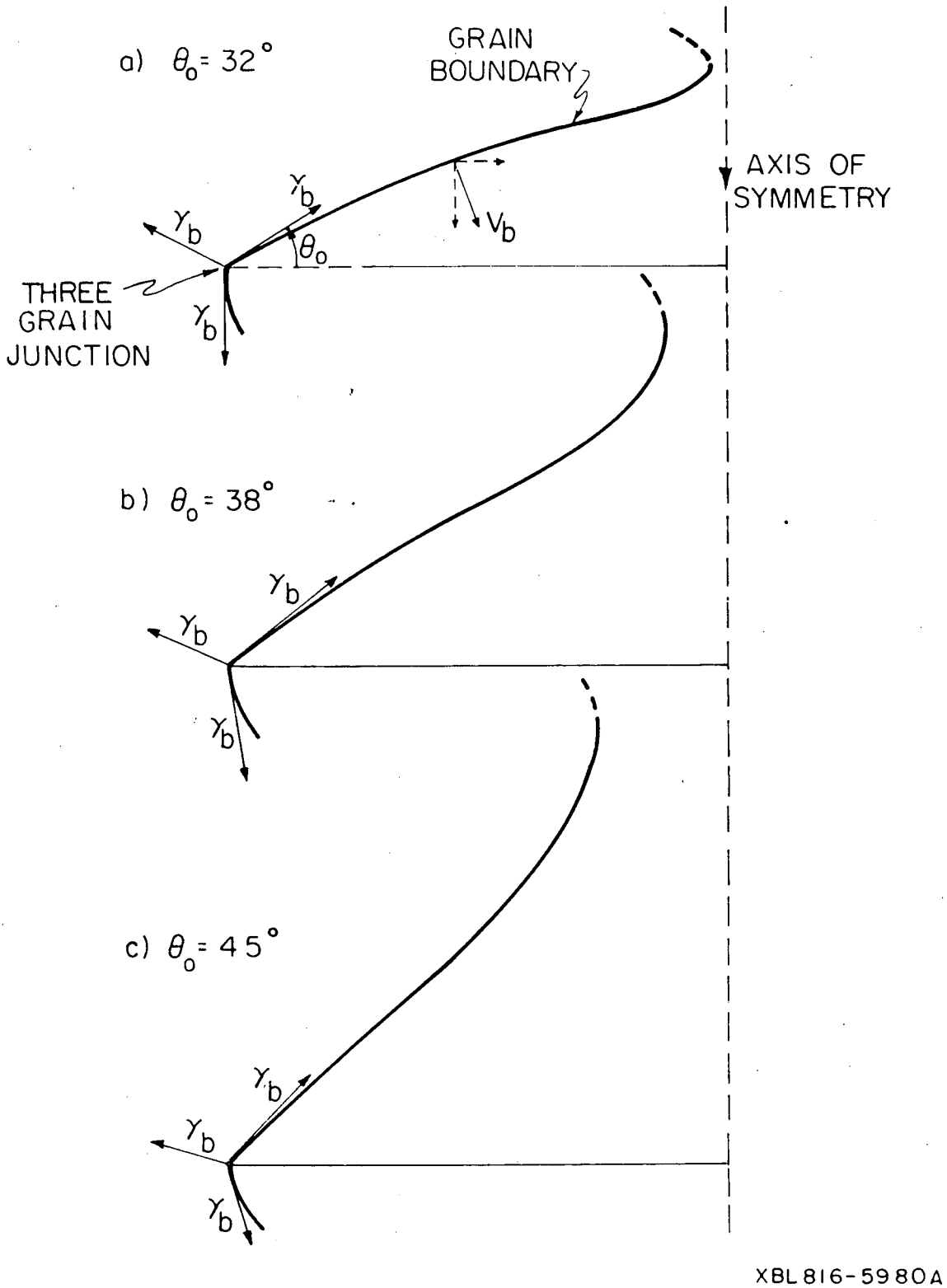
a) $\theta_o = 32°$
GRAIN BOUNDARY
AXIS OF SYMMETRY
γ_b
γ_b
γ_b
V_b
θ_o
THREE GRAIN JUNCTION
γ_b
b) $\theta_o = 38°$
γ_b
γ_b
γ_b
c) $\theta_o = 45°$
γ_b
γ_b
γ_b
XBL816-5980A

Fig. II-12

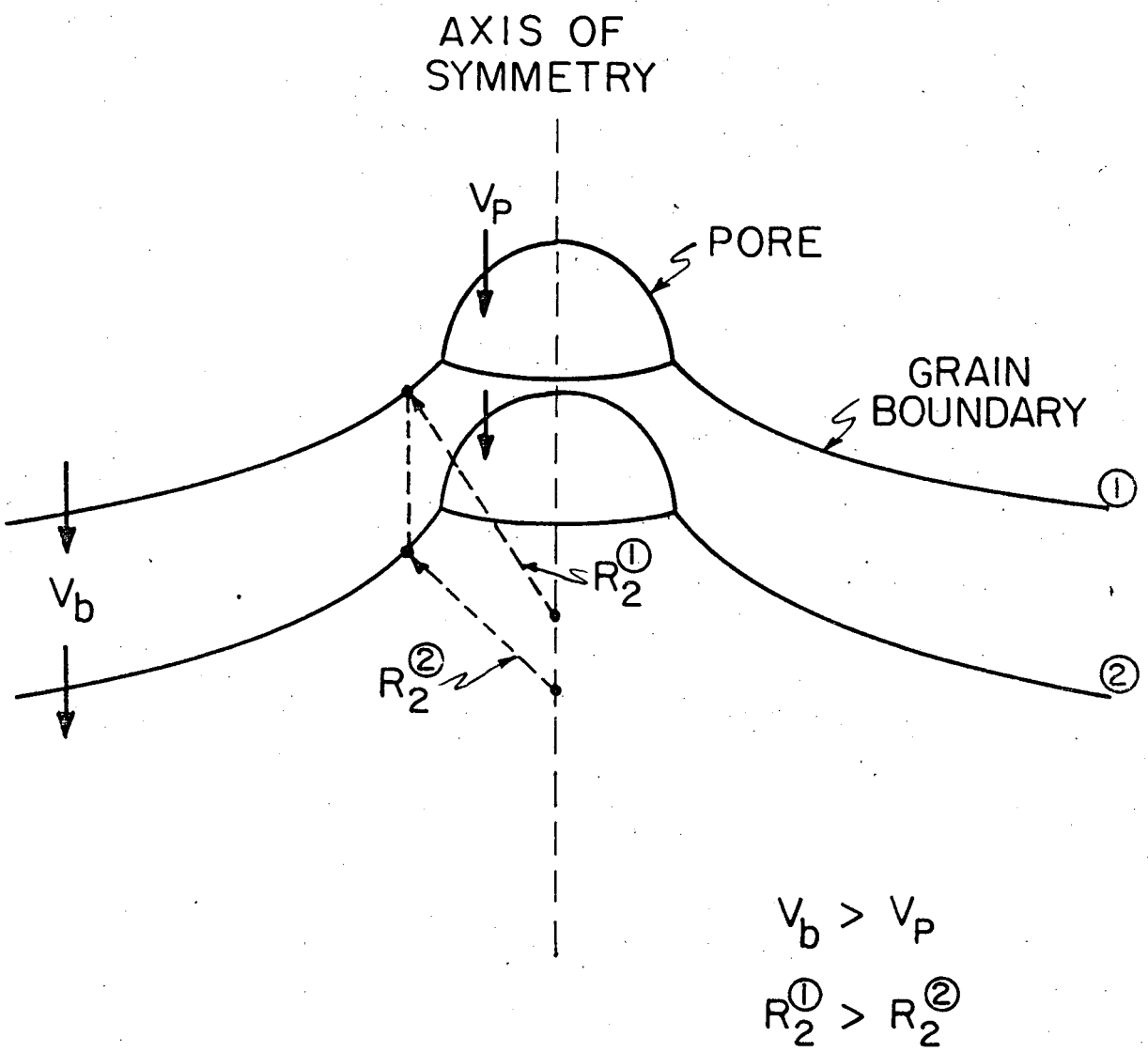
AXIS OF
SYMMETRY
V_P
PORE
GRAIN
BOUNDARY
①
②
V_b
$R_2^{①}$
$R_2^{②}$
$V_b > V_P$
$R_2^{①} > R_2^{②}$
XBL 816-5981

Fig. II-13

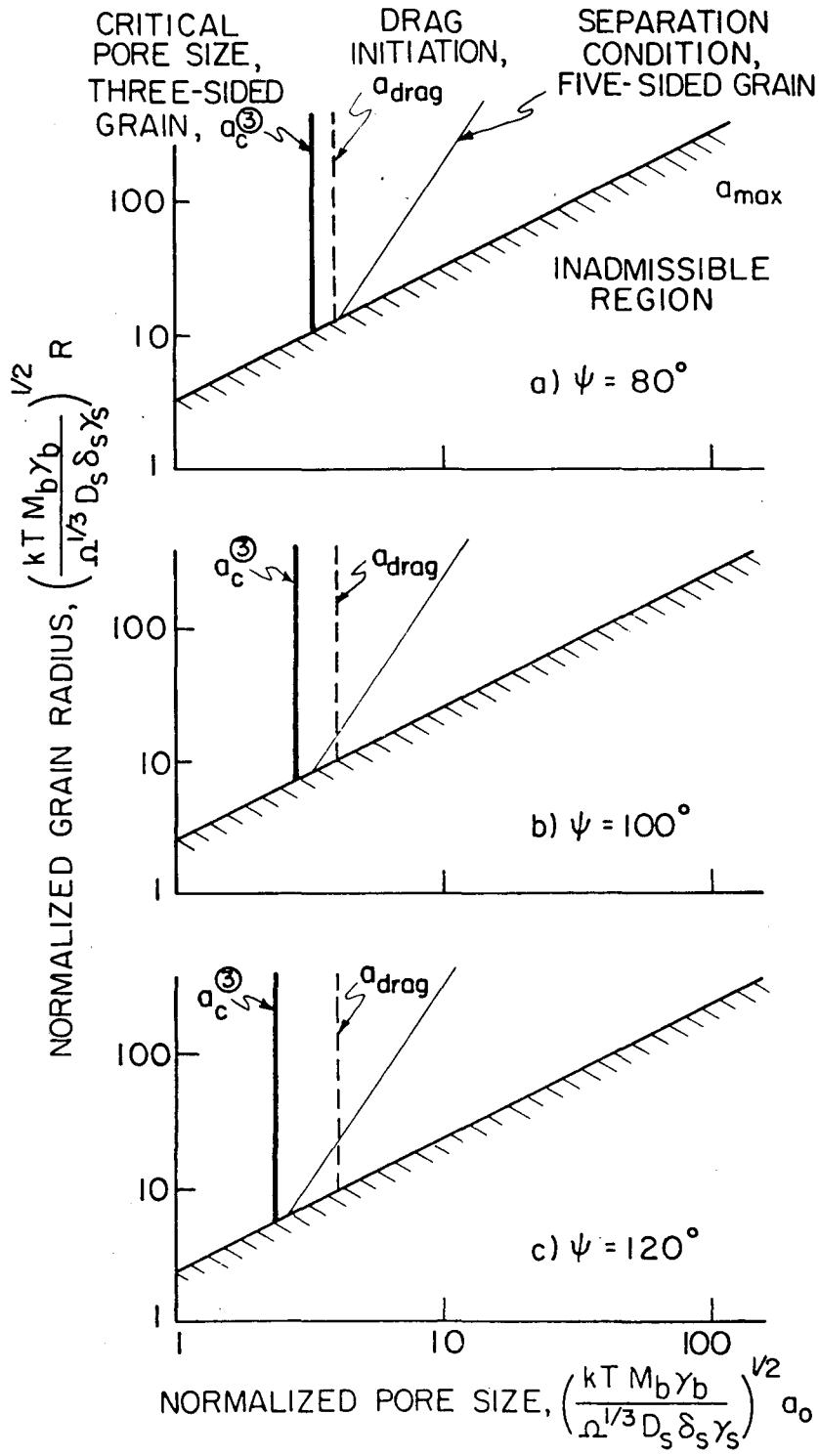
CRITICAL PORE SIZE, THREE-SIDED GRAIN, $a_c^{③}$
DRAG INITIATION, a_{drag}
SEPARATION CONDITION, FIVE-SIDED GRAIN
a_{max}
INADMISSIBLE REGION
a) ψ = 80°
b) ψ = 100°
c) ψ = 120°
100
10
1
NORMALIZED GRAIN RADIUS, $\left(\frac{kT M_b \gamma_b}{\Omega^{1/3} D_s \delta_s \gamma_s}\right)^{1/2} R$
NORMALIZED PORE SIZE, $\left(\frac{kT M_b \gamma_b}{\Omega^{1/3} D_s \delta_s \gamma_s}\right)^{1/2} a_o$
XBL 816-5982

Fig. II-14

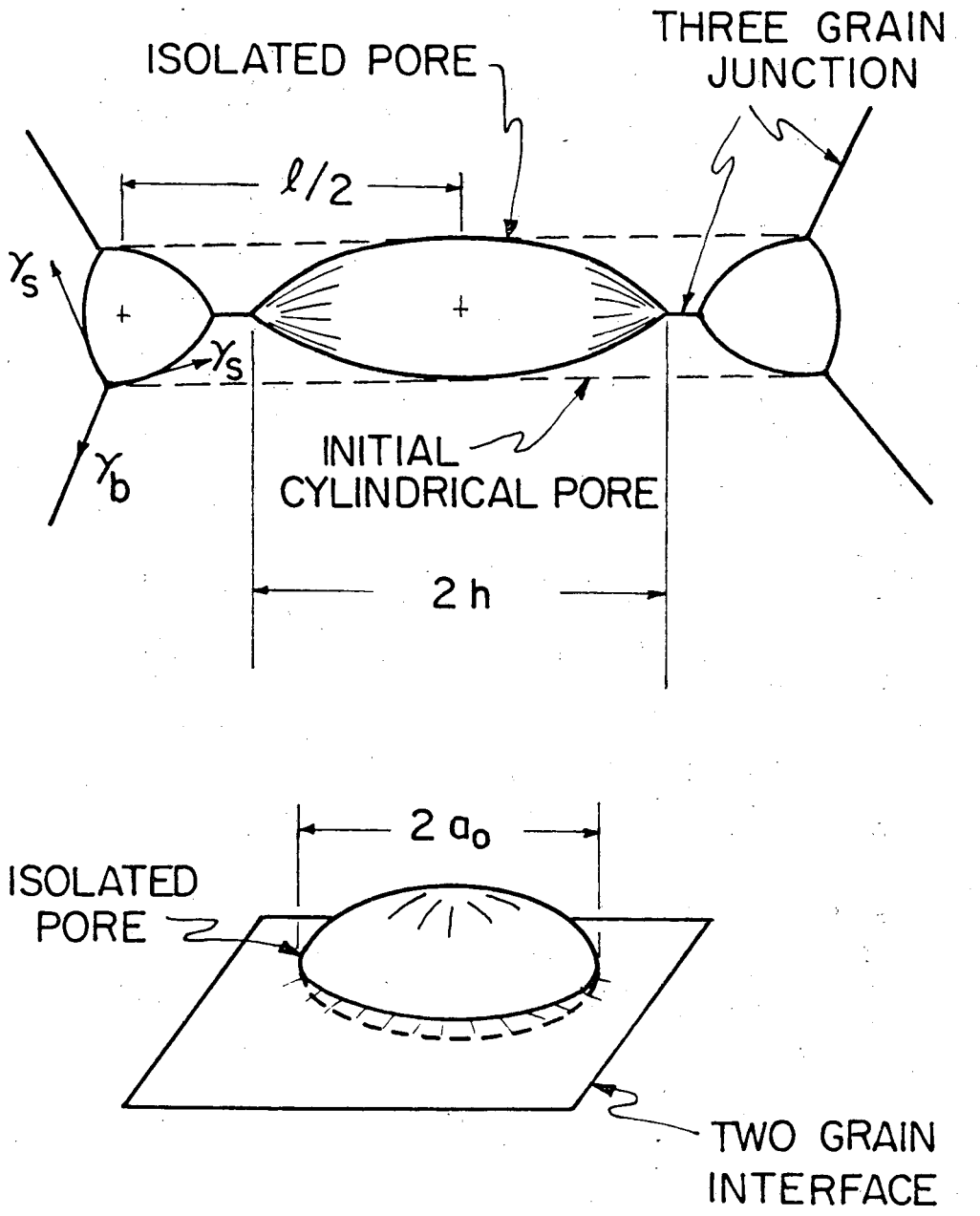
ISOLATED PORE
THREE GRAIN JUNCTION
ℓ/2
γ_s
γ_s
γ_b
INITIAL CYLINDRICAL PORE
2 h
2 a_o
ISOLATED PORE
TWO GRAIN INTERFACE
XBL 816-5983

Fig. II-15

TECHNICAL INFORMATION DEPARTMENT
LAWRENCE BERKELEY LABORATORY
UNIVERSITY OF CALIFORNIA
BERKELEY, CALIFORNIA 94720